Coded Aperture Imaging

novel approaches to high-energy high-resolution laboratory imaging

MATTHEW PETER SELWOOD

Doctor of Philosophy
UNIVERSITY OF YORK
Physics

MAY 2022

Abstract

Rapid advancement is being made in laser driven x-ray and particle sources, pushing the boundaries in temporal duration, spatial and spectral distribution, and maximum energy. These advancements need to be complimented with development of imaging capabilities, in order to fully characterise and utilise the new source potential. Here, coded apertures are used to investigate novel approaches to high-energy high-resolution aperture based imaging.

Firstly, coded aperture theory is applied to high-energy x-ray sources such as those generated using laser wakefield techniques. The coded aperture is compared to a single pinhole aperture, to discuss whether the prior assumption of highly attenuating substrates is required when using coded apertures. The coded aperture with scatter and partial attenuation included, dubbed a 'CASPA', is demonstrated with a 511 keV source simulation, showing that the fully attenuating 18 mm thick tungsten substrate for a single pinhole can be replaced with a 250 μm thick tungsten CASPA. Furthermore, the thin CASPA is not mechanism specific, and the physical processes behind the scatter and partial attenuation is found to be inconsequential as long as the combined result yields adequate hologram contrast for image decoding to occur.

Secondly, an investigation is conducted into imaging with spectral and spatial information for applications such as laser-solid interaction hotspots. Combing coded apertures with Ross pair filters, a banded spectrally-resolving coded aperture is discussed, dubbed a 'BaSCA', using multiple non-redundant array designs on a single aperture and single non-spectrally resolving detector.

Finally, the application of a CASPA for imaging high-resolution high-energy neutron sources from inertial confinement fusion experiments is discussed. Using the National Ignition Facility at Lawrence Livermore National Laboratory as an example, a CASPA is designed for the 14.1 MeV neutrons, and reconstruction techniques discussed. In comparison to the currently implemented 20 cm thick gold grand array, it is suggested here that a 10 mm tungsten CASPA would suffice - potentially reducing manufacturing costs, increasing ease of implementation and field of view.

Table of Contents

List of Figures

List of Tables

List of Codes

DEDICATION

There are many people I would like to thank for their support and input, to help me get to a place where writing this was possible:

I owe immeasurable thanks to my **mother**, without whom I would not have had half the chance at the academic life as I have. Between dyslexia, dyspraxia, and needing glasses, my life could have taken a different path if they were not caught early and I did not receive the specialist help required. I would also like to thank my **father** for his patient ear and advice with all things code, as well as the **entire family** for their acceptance of me geeking out during dinners and events. Though it is probably good that this dedication is at the beginning of the thesis, else they may never see it!

I would like to thank and **all my friends**, for varying levels of patience throughout this process. Whether it was understanding when I had to bow out of social events due to experiments, distracting me from work in various enjoyable ways, or correcting me when I English write no good, I am appreciative of all the support.

I must also thank **Dr. Chris Murphy**, not only for all his supervisory help and advice over the years, but also for taking a chance on me in the first place. I hope I have repaid that gamble with new networks and academic prosperity, and saving that, social amusement. Thanks to **Dr. Chris Underwood** and **Dr. Chris Baird** for accepting me as a non-Chris in the Chris group, and helping me hit the ground running with codes, discussions and teaching. Ditto for all members of the **YPI** for their discussions along the way.

I feel **Spotify** requires an honourable mention too, for sustaining my music addiction through the difficult times. Whether it be to give me energy at 2 am in a dark underground lab, or at 2 pm in the office to drown out noisy neighbours, music was always on. Loud, fast, and heavy.

Finally, I would like to thank **Mr. Peter Bonsall**, my 6^{th} form physics teacher. Without his help to enthuse me in physics, and to show me the fascinating ideas that are out there, I would probably be a chemical engineer somewhere in the middle east about now. A far less fulfilling life, I am sure he would agree.

"I've got a plan so cunning, you could put a tail on it and call it a weasel!"

Edmund Blackadder Esq.

Author's Declaration

I declare that this work was carried out in accordance with the requirements of the University's Regulations and Code of Practice for Research Degree Programmes and that it has not been submitted for any other academic award. Except where indicated by specific reference in the text, the work is the candidate's own work. Work done in collaboration with, or with the assistance of, others, is indicated as such. Any views expressed in the dissertation are those of the author.

SIGNED:  DATE: 04 MAY 2022

Matthew P. Selwood

Acknowledgements

This work was supported by the Engineering and Physical Sciences Research Council [EP/L01663X/1], Scitech Precision, and the Science and Technology Facilities Council. Some of the simulations were undertaken on the Viking Cluster, which is a high performance computer facility provided by the University of York, and thanks are given to the University of York High Performance Computing service, Viking and the Research Computing team.

Thanks are extended to Dr. David Fittinghoff and Dr. Petr Volegov, whose advice and discussion was always appreciated. Although not featured here, thanks are also extended to the staff and users of the Central Laser Facility at the Rutherford Appleton Laboratory, for the experimental knowledge and facilities.

CHAPTER 1

INTRODUCTION

High-energy imaging has a wide range of uses that can be split into two broad categories; diagnosis and application. Various processes, such as nuclear fusion, generate high-energy particles which can be used to diagnose some information about the reaction[1]. Applications can be found in anything from investigating defects in dense materials within engineering[2], to positron-electron tomography (PET) in medical imaging[3] and locating radiation leaks in industrial systems[4]. Current laser plasma research continues to improve the control[5], temporal[6], spatial[7], and spectral[8] characteristics of radiation sources. Parallel advancements in imaging techniques are paramount in order to fully utilise the improved sources.

This work focuses on improving coded aperture techniques in three areas:

1. High-energy photon imaging
2. Imaging with spectral selectivity
3. High-energy high-resolution neutron imaging

where improvement is measured either by ameliorated results or comparable results from a cheaper and easier to implement imaging system. Although the range of applications for high-energy imaging is broad, a specific example will be used per area to discuss how scientific capability could be increased through coded aperture use.

1. Electron-positron annihilations from laser wakefield acceleration.
Research into electron-positron plasmas is important for astrophysics as they naturally occur in extreme regions of the universe[9–12]. Electron bunches striking metal targets can be used to generate positron beams[13], with Sarri *et al.* suggesting that it can also be used to generate neutral electron-positron plasmas[14]. Electron-positron annihilations produce a pair of quantum entangled 511 keV photons in opposing directions[3] and imaging the source size of these photons

could be used to infer the size of the electron-positron plasma. This could then be compared to simulations presented by Sarri *et al.* to verify the plasma properties suggested[14].

2. Plasma temperature from laser-solid interactions.
When a high-intensity laser interacts with solid matter, a thin (often µm size) plasma is formed on the surface and electrons are accelerated through the cold bulk of the material[15]. Measurements of the electron temperature can be used to infer plasma characteristics for applications in electron source generation[16], warm dense matter studies[17], and inertial confinement fusion[18]. Many single-detector techniques utilise two dimensions, one spectral and one either spatial or temporal[19–21], requiring assumptions to be made about the source shape and its symmetry. Being able to image small-scale plasmas in two dimensions with some spectral information will help diagnose asymmetric laser-solid interactions.

3. Primary neutrons from inertial confinement fusion reactions.
Fusion energy is being investigated as a carbon-neutral energy source to reduce the world's dependency on fossil fuels, and potentially help combat global warming[22]. In inertial confinement fusion experiments, a fuel capsule is spherically imploded to form a high-density high-temperature core where fusion reactions will occur and release high-energy neutrons. The neutron yield, which is used for energy production, has dependency on the symmetry of the implosion among other factors. Therefore, imaging neutrons from the implosion is used to help understand the implosion symmetry and improve overall reaction yield.

1.1 Laser Wakefield Acceleration

Radio-frequency linear accelerators (linacs) are conventionally used for electron acceleration. They have a limit to acceleration gradient to the order of 10^2 MV/m, before electron breakdown occurs[23], with electron bunch widths to the order of 100 µm[24]. In order for high energy electron research to be more accessible in a laboratory setting the length of the accelerating medium would need to be of the order of millimetres, rather than kilometres found with linacs. This would require acceleration gradients closer to 10^2 GV/m[23], which have been achieved through use of laser wakefield acceleration (LWFA).

Propagation of an intense laser pulse through a gas will ionise the species to form a plasma[25]. The same laser pulse will exert the ponderomotive force on the plasma, due to the high potential gradient:

$$\vec{F}_p = -\frac{q^2}{4m\omega^2}\nabla\langle E^2\rangle \tag{1.1}$$

where q is the electric charge of the particle, m its mass, ω is the angular frequency of the field, and E is the amplitude of the electric field[26]. The direction of the force acts down the potential gradient.

This creates a cavity behind the propagating laser of low electron density as they have been dispersed due to the ponderomotive force. It is noted that, due to the higher mass, ions are not moved within the same timescales and can be considered to create a stationary quasi-uniform field. Dispelled electrons are then accelerated back towards the cavity by the quasi-static ion background and fall into harmonic oscillation, with the oscillation frequency equal to the plasma frequency:

$$\omega_p^2 = \frac{n_e e^2}{\epsilon_0 m_e} \tag{1.2}$$

where n_e is the number density of electrons, e amd m the electron charge and mass respectively, and ϵ_0 is the vacuum permittivity[27]. This plasma wave will follow the propagating laser pulse, with a comparable phase velocity[28]. Electrons can become trapped within this cavity, by a process known as injection, and accelerated up to relativistic speeds. The electric field along the laser propagation axis can accelerate injected electrons to velocities higher than the group velocity of the laser pulse[29]. The generation of this wake behind a laser is depicted in figure 1.1 and the technique is known as laser wakefield acceleration. It is noted that other forms of plasma accelerators can be used[30–33], but the LWFA is the accelerator of study within the research group.

Published work has demonstrated a breadth of tuned LWFA from temporally short electron beams at 1.4–1.8 fs[34] to high-energy 7.8 GeV bunches[35], with their broad tunability an appealing characteristic for researchers. Divergence of the order of milliradians is common, with field gradients of the order of 10 GV/m, bunch diameters of the order of 10 µm and energies from MeV to low GeV[36].

1.1.1 X-Ray Sources

Research is still being carried out on how best to control the injection mechanism of electrons into the accelerating cavity of a LWFA[37,38]. If the electrons are injected into the cavity off-axis (with respect to the laser propagation direction), there will be a radial electric field which acts to drive the electrons back towards this axis and cause simple harmonic motion, resulting in sinusoidal propagation. The acceleration due to change of direction of the electron will produce synchrotron-like radiation, in a process known within LWFA literature as betatron radiation†. The spectral profile of the x-rays is dependent on where the electrons are injected and how distributed the initial injection sites are from the laser propagation axis. Narrow energy spread electron bunches have been published[39–41] and the x-rays produced are in the 10–100 keV range[42], with source sizes of the order of microns with high spatial coherence[7,43–45].

†It is noted that this is different from the original definition in particle physics, where a betatron is the name of the machine used to accelerate electrons in a circular path to produce this radiation. Here, betatron radiation is used to refer to the photon produced when an electron undergoes betatron motion

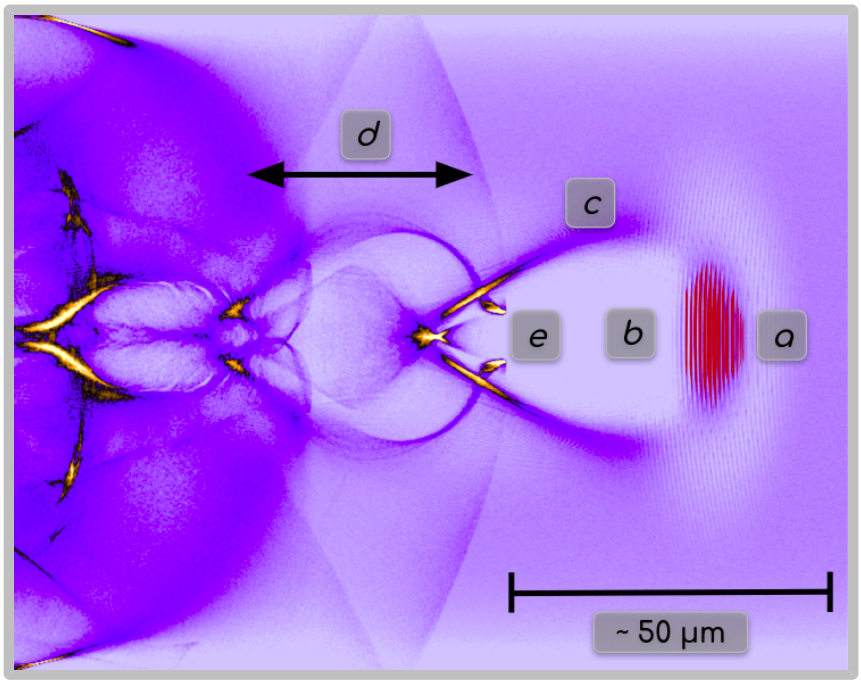

FIGURE 1.1. A simulation of a LWFA courtesy of Chris Underwood, with the colourscale representing electron density and the laser highlighted in red. The laser pulse at (a) propagates from left to right through the plasma. The ponderomotive force leaves a cavity at (b) of low electron density. Electrons are accelerated back towards the cavity at (c), creating harmonic oscillation and plasma waves of wavelength (d). Here, the plasma wave wavelength is 20–30 µm. Electrons within a spectral band become trapped in the cavity, and are accelerated in a bunch behind the laser at (e).

Bremsstrahlung radiation[46] may be generated from LWFA electron beams, and is also produced by a change in electron velocity. When incident on a solid target or foil (referred to as a converter), the electron deceleration experienced due to the electric fields of nuclei within the converter will emit x-rays in a conical and broadband spread out of the convertor rear surface. The maximum photon energy produced is equal to the maximum electron energy and the radiated power will be a function of the convertor's atomic number, ion density, thickness, and the electron beam properties. Source sizes will depend on the electron beam divergence and convertor thickness, but is still usually of the order of 10–100 µm[47,48]. Experimentally, bremsstrahlung is one of the easiest x-ray production methods to implement and control.

In contrast, inverse Compton scattering (ICS) is the most experimentally challenging method, but is highly desirable due to its ability to produce MeV x-ray sources with narrow energy spreads[49,50]. ICS occurs due to the transfer of energy from a relativistic electron to a photon during a collision[51], thus requiring a second laser to counter-propagate with the accelerated electron bunch for maximal energy transfer. The photon energy is a function of the electron energy

pre-collision and incoming laser energy, which are all tunable. It is noted that, if the counter-propagating laser intensity is above a certain threshold the scattering mechanism becomes non-linear and the resultant x-ray spectrum tends towards a synchrotron-like spectrum[52].

The choice of x-ray source is often dictated by experimental feasibility and desired source properties for the application. Some typical source parameters can be seen in table 1.1 from experiments performed on a plethora of lasers. It is noted that betatron radiation will be present in most LWFA sources[47,53], unless specific care is taken to inject electrons on-axis. However, the thickness of converter for bremsstrahlung radiation can attenuate the low energy photons from the betatron.

	Source Size (μm)	Energy Spread	Energy (MeV)	Photons
Betatron	15 – 50	dependent on injection	< 0.035	10^6–10^9
Bremsstrahlung	30 – 300	broadband	< 17	10^8–10^{11}
ICS	3 – 25	quasi-mono-energetic†	< 18	10^7–10^8

Table 1.1: Common properties for LWFA x-ray sources using the three x-ray generation techniques discussed. Data from Albert and Thomas[53], and Lemos *et al.* [47].
†Linear Inverse Compton is narrow band and quasi-mono-energetic, while non-linear will have harmonics generated.

1.1.2 Electron Positron Plasma

Photons emitted via bremsstrahlung continue to interact with the converter after they are produced, and can form an electron-positron pair via multiple mechanisms, depending on the field in which the decay occurs. Photon decay in the field of a nucleus is known as the Bethe-Heitler process[54,55], and in an electromagnetic field (typically a laser) is the Breit-Wheeler process[56]. These are both two-step a processes, requiring the incident electron to be converted to a photon before the pair production. Direct pair production from an electron is possible via the trident process, where the intermediary photon exists only virtually within the electric field of the nucleus[57]. There is a probability that the newly formed electron will decelerate due to another nucleus in the converter, emitting a new photon and in turn a new electron-positron pair. This process is often referred to as a cascade[58].

It is noted that the Breit-Wheeler process requires high laser intensities of 10^{23} W/cm^2, with no facilities currently online that are able to produce this[59], although this threshold may be reached soon with facilities such as ELI-NP[60], ELI-beamlines[61], and CoReLS PW[62].

1.2 Laser-Solid Interactions

High-intensity laser-solid interactions can ionise the solid at the interaction site, creating a plasma film which expands outwards. The plasma can be characterised by a plasma frequency (ω_p), which is the resonant frequency of electrons. Electromagnetic propagation through the

plasma is dependent on the local plasma frequency, where the plasma is opaque to incident waves below the plasma frequency, and transparent to higher frequency incident waves.

The number density of electrons will increase further into the target, and therefore equation 1.2 shows that the plasma frequency will also increase. Therefore a limit will be reached as a function of depth into the plasma plume where the plasma frequency will increase beyond the laser frequency, preventing further laser propagation. Instead, at this boundary the laser may be reflected or coupled into the plasma, usually both[63].

Multiple mechanisms compete in coupling laser energy to the plasma. In order of relevance with increasing laser intensity, these include: inverse bremsstrahlung, resonance absorption, vacuum heating and $\mathbf{J} \times \mathbf{B}$ heating[64]. Spectral imaging of the plasma could increase capability for experimentally understanding the interplay between competing coupling mechanisms.

Electrons are able to gain energy via photon absorption in the electric field of a nucleus through inverse bremsstrahlung[65] - a process named for being the reverse of bremsstrahlung x-ray generation. Resonance absorption occurs when the laser frequency equals the plasma frequency, and the amplitude of the electron oscillations increase due to resonance to a non-linear extent until wave breaking, otherwise known as Landau damping[66], and transferring energy into the plasma[67,68]. In vacuum heating, electrons are pulled from the solid into the vacuum or lower density plasma region due to the high density gradient, and return to the solid having gained kinetic energy due to the movement[69]. $\mathbf{J} \times \mathbf{B}$ heating is forward acceleration of electrons due to the magnetic component of the Lorentz force, which escape along the laser propagation axis into the overdense plasma[70].

As the laser does not propagate through the entire solid, electrons accelerated due to vacuum heating, $\mathbf{J} \times \mathbf{B}$ heating and the ponderomotive force propagate conically through the solid away from the interaction site along the laser axis[15]. The rest of the solid is referred to as the cold bulk, where the laser (and ensuing plasma) has not transferred energy to prior to the electron acceleration. Accelerated electrons can reach relativistic energies across a Maxwellian-esque distribution[64], and individual behaviour of the accelerated electrons in the cold bulk solid depends on the electron energy. The low energy electrons will be trapped inside the solid and deposit all their energy[17]. A higher energy electron will produce K-shell vacancies of atoms they impact, before escaping the rear of the solid[72]. The K-shell vacancies will produce K_α emission, of energy characteristic to the atomic species. By measuring the spectral features of emission from the rear of the target, and comparing the relative intensities between this and other emission lines for a known solid, the plasma temperature can be inferred[73].

To infer plasma temperature at solid density, high spatial resolution is required to resolve features of the interaction site between the focused laser and the solid[74,75]. This can aid research into warm dense matter for astrophysical objects[76], as well as laser-solid energy coupling for nuclear fusion applications[18].

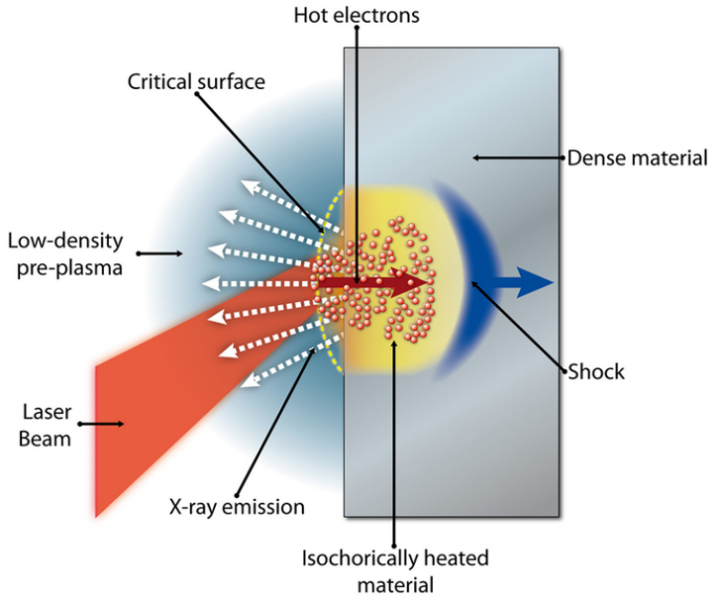

FIGURE 1.2. A diagram of a laser-solid interaction, with the laser (red) creating a plasma film and accelerating electrons conically into the cold bulk of dense material. Figure reproduced from Arber *et al.* [71].

1.3 Nuclear Fusion

The mass of a nucleus is always lower than that of its constituent nucleons (protons and neutrons). This mass deficiency is known as the nuclear binding energy, and can be calculated through Einstein's mass-energy equivalence[77]. The elements with the highest binding energy per nucleon fall a range between iron^{56} and nickel^{62} [78]. When elements of a lower atomic number fuse together, the binding energy per nucleon will increase, and the mass deficit will be released as energy, as well as a neutron often being expelled[79].

Low atomic number nuclei will require less energy input to overcome the electrostatic repulsion, and are attractive candidates for fusion fuel. As with any kinetic system, the probability of a successful collision between fuel particles (cross section) is a function of temperature, and a higher cross section peak is desirable to maximise the number of reactions per unit volume per unit time. The reaction with the highest cross section peak is deuterium and tritium (henceforth referred to as DT), which are both isotopes of hydrogen with 1 and 2 neutrons respectively:

$$ {}^{2}_{1}\mathrm{D} + {}^{3}_{1}\mathrm{T} \rightarrow {}^{4}_{2}\mathrm{He}\ (3.5\ \mathrm{MeV}) + {}^{1}_{0}\mathrm{n}\ (14.1\mathrm{MeV}) \tag{1.3} $$

The DT cross section peak also occurs at the lowest temperature for fusion-viable sources, reducing the energy input requirement before reactions occur. However, tritium is naturally scarce and its radioactivity makes it more difficult to use experimentally. Preliminary fusion studies are often performed using a deuterium fuel for deuterium deuterium reactions (henceforth

referred to as DD). Deuterium is a stable isotope, more abundant than tritium, and the DD reaction is a useful analogue to DT for experimental purposes, but with a lower energy output. The reaction has two potential pathways, each with a 50% probability:

$$\begin{aligned} {}^{2}_{1}\mathrm{D} + {}^{2}_{1}\mathrm{D} &\rightarrow {}^{3}_{1}\mathrm{T}\ (1.0\ \mathrm{MeV}) + {}^{1}_{1}\mathrm{p}\ (3.0\ \mathrm{MeV}) \\ &\rightarrow {}^{3}_{2}\mathrm{He}\ (0.8\ \mathrm{MeV}) + {}^{1}_{0}\mathrm{n}\ (2.5\ \mathrm{MeV}) \end{aligned} \tag{1.4}$$

The Lawson criterion is a useful metric in order to compare the rate of energy production within fusion reactions to the rate of energy lost from the system[80,81], stating the minimum value for a system to have a higher rate of energy production than losses. It is noted that some refer to this as *ignition*, but this is a term with multiple definitions and is currently a hotly contested discussion point within the community. In order to avoid unnecessary controversy, the term will henceforth not be used in any of its forms. The Lawson criterion is often expressed as the triple product between the density, n, the temperature, T, and the confinement time, τ_E, or $nT\tau_E$. For a DT reaction, the Lawson criterion is[82]:

$$nT\tau_E \geq 3 \times 10^{21}\ \mathrm{keV\ s/m^3} \tag{1.5}$$

As the Lawson criterion is a threshold, maximising this triple product is prudent.

The criterion has led to two different approaches to fusion energy, which both require high temperatures to exceed the Lawson criterion threshold. One such approach is to extend confinement time for as long as possible, and keep a continuous plasma fusing for the duration. This approach requires the plasma to be confined for long periods, and is referred to as magnetic confinement fusion (MCF). A second approach is to increase the density, and is referred to as inertial confinement fusion (ICF).

1.3.1 Inertial Confinement Fusion

Having increased density at high temperature reduces the need for long confinement times in order to satisfy the Lawson criterion. By uniformly compressing a sphere, the core will increase in density and temperature until fusion occurs and the criterion is exceeded. However, as fusion occurs and pressure at the core increases, a rarefaction wave causes fuel disassembly. The confinement time is then the duration for which reaction rate is sufficient to burn a significant fraction before the fuel disassembles, which can be approximated through hydrodynamic calculations of the time taken for a rarefaction wave to propagate through the fuel from the vacuum boundary. This will be a function of radius, and the mass average along each radial distance is typically used for the global confinement time[83].

The spatial and spectral distributions of neutrons, as well as their total yield, are a useful metric in analysing ICF implosions. The alpha particles produced need to remain confined within the hotspot to keep the temperature high for subsequent fusion reactions, whereas the energetic

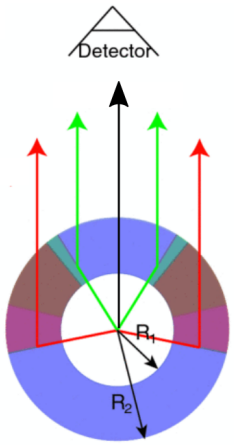

FIGURE 1.3. A depiction of primary (black) and two different energies of secondary (green and red) neutrons from an ICF implosion, and their relative paths to the detector. The fusing hotspot (white) is surrounded by relatively cold dense fuel (blue). Figure reproduced from Gatu Johnson *et al.* [84].

neutrons will escape far more readily. It is these neutrons that will be captured for energy production, and will indicate the efficiency of the implosion. For a known initial number of particles within the fuel, the number of neutrons can be used to infer the rate of fuel loss, and the shape of the neutron source can show to the uniformity of the implosion. A more uniform implosion is likely to create a higher density hotspot and increase fusion reactions resulting in a more efficient fuel capsule. A majority of the neutrons will travel through the fuel unperturbed and escape with all 14.1 MeV of their initial energy, and are referred to as primary neutrons. A smaller fraction of neutrons can be downscattered in energy and escape at different angles, which are referred to as secondary neutrons, as shown in figure 1.3.

The total energy, required to compress the capsule to an adequate size, scales with fuel density and capsule radius. However, with too small a capsule the alpha particles produced would not stay contained within the hotspot and would escape. It is for this reason that ICF capsules tend to have a resting radius of *ca.* 500–750 µm, which can scale down to *ca.* 50–150 µm at peak compression[85,86]. Within this, the hotspot radius of fusing material is often within the range of 25–35 µm[87].

1.3.2 The National Ignition Facility

The National Ignition Facility (NIF) is the largest ICF experiment in the world, housed at the Lawrence Livermore National Laboratory in California, USA[88]. It achieves compression of the fuel via a thin shell which is ablated from the fuel surface, which from Newton's 3rd law creates a compression force. Henceforth this shell is referred to as the "ablator". The ablator material, thickness and properties are still being investigated to improve implosion dynamics[89–92]. NIF

use 192 laser beamlines in order to deliver energy to their capsule, amplifying laser energy while its wavelength is 1053 nm before frequency tripling it down to 351 nm pre-capsule. In total, the lasers hold a nominal 4 MJ energy, and the optics are used very close to their damage thresholds. Between optical damage and cooling times, the repetition rate of NIF shots is on average 2 per working day[93].

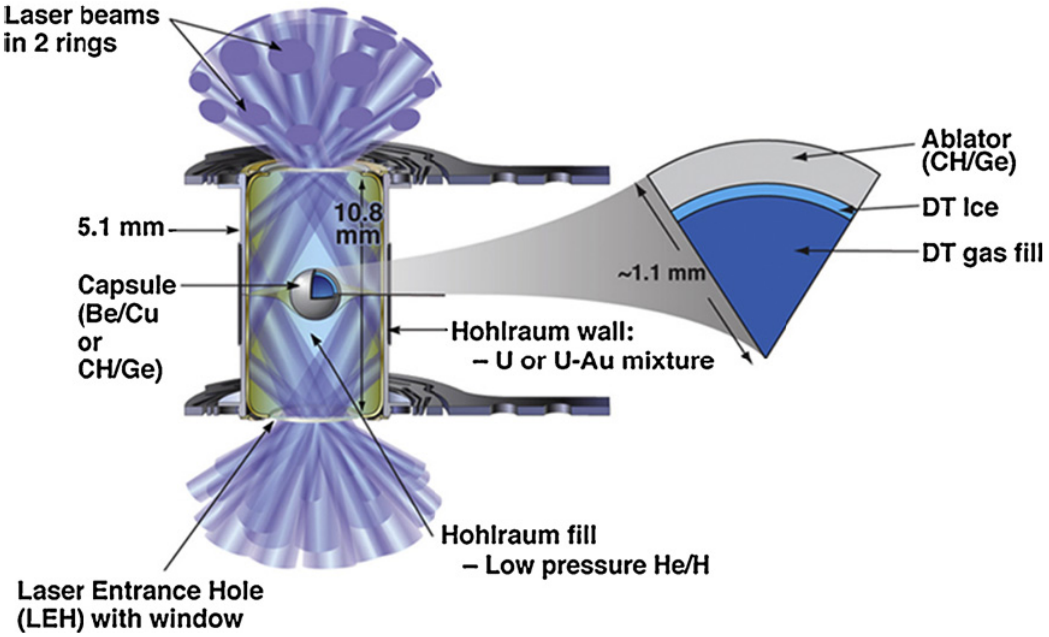

FIGURE 1.4. A diagram of an ICF target for NIF experiments, with (left) the indirect-drive hohlraum and (right) a schematic of the capsule. Figure reproduced from Moses *et al.* [94].

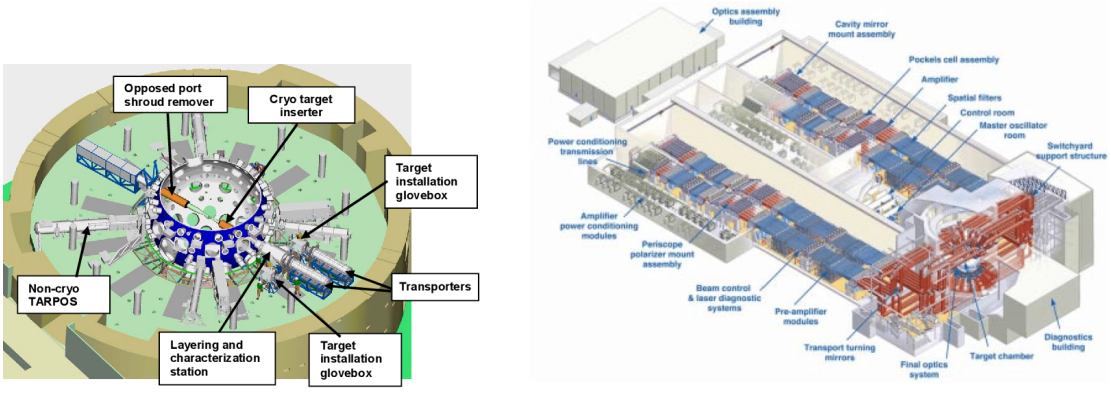

(a) (b)

FIGURE 1.5. A depiction of (a) the target chamber of NIF[95] and (b) its laser system[96]. Figures reproduced from Moses *et al.*.

The vacuum target chamber is 5 m in radius, with the fuel capsule held at its centre. Between the arm to hold the capsule, diagnostic inserters, line-of-sight paths, and the 192 beam paths converging on the capsule, space is at a premium. A diagram of the target chamber and the laser system can be seen in figure 1.5.

Coupling of energy to the ablator is crucial, with uniform energy coupling across the surface aiding symmetric implosions. Many mechanisms exist for coupling energy to the ablation layer[97–100], with the laser energy being coupled directly to the ablator in the original scheme[101], referred to as direct drive. However, the lack of energy coupling uniformity was detrimental to implosion symmetry, and instead a scheme named indirect drive is currently favoured at NIF[18]. This is where laser energy is coupled to a cylindrical *hohlraum* surrounding the capsule to induce x-ray production, and the x-rays are then coupled to the ablator.

With small implosion diameters of *ca.* 50 µm, high-resolution imaging is required to highlight asymmetries which may be reducing fusion efficiency. Currently, the NIF neutron imaging system has a resolution of 10 µm and a substrate thickness of 20 cm solid gold[102]. The next generation of neutron imaging apertures[103] will cost in the region of $800,000 to manufacture and characterise[104].

CHAPTER 2

THEORY

Optical imaging systems often utilise the refractive index and reflectivity of materials to control the path of photons towards the detector. Lenses and mirrors control the focal plane of the system, object magnification, and allow for detectors to be put in convenient locations further from the source being imaged. The refractive index, n, is a measure of change in velocity of light at the boundary between two media:

$$n = \frac{c}{v} \tag{2.1}$$

where c is the speed of light in a vacuum, and v is the phase velocity of light in the medium[105]. This is often expressed in a different form for x-rays, as the phase velocity in a medium can be marginally greater than the speed of light, and therefore n is slightly less than 1:

$$n = 1 - \delta \tag{2.2}$$

where δ is the dispersion term, which scales as the square of the wavelength of the incident photons:

$$\delta = \frac{r_0 \lambda^2 n_e}{2\pi} \tag{2.3}$$

where r_0 is the classical electron radius, λ the wavelength of the light, and n_e the electron density in the medium[106]. For x-rays, where wavelengths are of the order of nm, $\delta \to 0$ and thus $n \to 1$. With a refractive index $\approxeq 1$, the photons pass through the medium unperturbed - preventing the use of lenses for x-ray imaging.

A similar argument can be used for the difficulty of using mirrors for short wavelength imaging. The reflectivity of a surface, ρ, at normal incidence can be calculated from the difference of refractive indices through the Fresnel equations to be:

$$\rho = \left| \frac{n_1 - n_2}{n_1 + n_2} \right|^2 \tag{2.4}$$

When $n_2 \to n_1$, $\rho \to 0$ and no reflection occurs. With the refractive index of air and vacuum ≈ 1[105], short wavelengths are not reflected and mirrors cannot be used. As such, lensless imaging techniques are required for x-rays, or for particles that do not refract reliably.

2.1 Pinhole Imaging

Pinhole imaging is commonly used as a lensless imaging technique. This is comprised of a single perforation machined into a substrate, and under the assumption that the substrate is opaque to incident particles the perforation will project an image of the source onto some detector plane behind as shown in figure 2.1. The nomenclature of imaging a source will be used here, noting that a source need not be an active emitter; backscatter imaging from an object, or backlighter imaging through an object are both included in this definition.

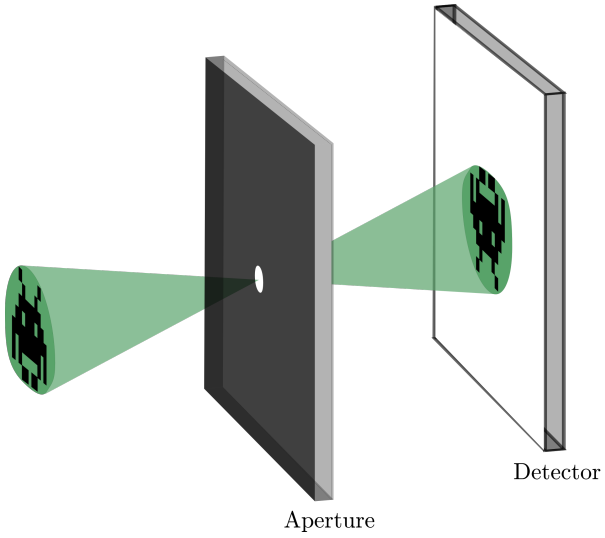

FIGURE 2.1. A schematic for pinhole imaging with a single perforation. Light (green) from the source (space invader) is imaged through the single perforation on the aperture to form an inverted image on the detector.

The ability for a pinhole aperture to image detailed features can be quantified by the resolution capability, R:

$$R = \frac{1}{r_{ab}} \tag{2.5}$$

where r_{ab} is the minimum distance between two point sources a and b such that they can be resolved seperately on the detector. The highest possible image resolution for a circular aperture is diffraction limited, with the optimal pinhole diameter, d_{opt}, given by[107]:

$$d_{\text{opt}} = \sqrt{2.43\ v\lambda} \tag{2.6}$$

where v is the aperture to detector distance, and λ is the wavelength of the incident photon. For x-ray imaging, nm scale wavelengths render production of an optimally sized pinhole impractical. For anything but the brightest of sources, having a pinhole of the order of nm^2 is not likely to have enough throughput of photons to produce an adequate image above background levels.

Instead, the resolution capability of a system can be calculated geometrically, assuming the pinhole diameter is not close to the diffraction limit ($d >> \lambda$), and photons can be modelled as particles with negligible diffraction effects:

$$\frac{1}{R} = d\left(\frac{u+v}{v}\right) \tag{2.7}$$

where u is the distance from the source to the aperture. In optics, the magnification of a system, M, is expressed as v/u, and the resolution capability is often defined as:

$$\frac{1}{R} = d\left(\frac{1}{M}+1\right) \tag{2.8}$$

This shows there is an intrinsic counterbalance between signal strength and resolution capability for a pinhole aperture. Experiments with low intensity sources must reduce resolution capability for adequate signal when using a pinhole aperture.

2.1.1 Source Size Measurements

It is noted that when imaging an object, that the resolution capability is limited by the largest of three factors: perforation size, detector pixel size, or source size. The relationship between perforation size and resolution capability has been discussed above, showing inverse proportionality. The detector pixel size limits the resolution of the system due to the quantisation of the signal, where features resolvable by the perforation may still be detected within the same pixel and become indistinguishable. The impact of detector pixel size on resolution capability can be reduced by using increased system magnification, although for a highly divergent or radially emitting source this will reduce the flux intersecting the detector.

In an idealised system, the source size is infinitesimally small and emitting uniformly and projects an image of the object onto the detector. However, as source size increases, each point in the emitting source will project an image of the object onto the detector in a slightly different position, resulting in a detector image that is the convolution of the source and object. If the source is larger than the desired resolvable feature on the object, it will be blurred out due to this convolution and the total system resolution capability has decreased[108].

However, experimental results suggest that resolutions smaller than the source diameter are achievable due to finite detector areas, if the source is uniformly emitting[38]. It was found that, for divergent sources such as those of a LWFA bremsstrahlung x-ray source, the outermost photons

can posses a divergence great enough to prevent them hitting the detector area. Thus, even as source size increases, the effective source size of photons with a divergence angle subtending onto the detector will reach an upper limit and the effective imaging resolution will not be affected.

2.2 The Grand Array

One way to increase the signal without reducing resolution capability is to use a pinhole array, otherwise known as a grand array. Here, multiple perforations are put onto a single aperture such that they each produce a projection of the source on the detector, as shown in figure 2.2. The perforations are separated enough for their projections to be independent on the detector, with no overlap. In post processing, these images are overlaid to artificially increase the signal strength while still having the same resolution capability.

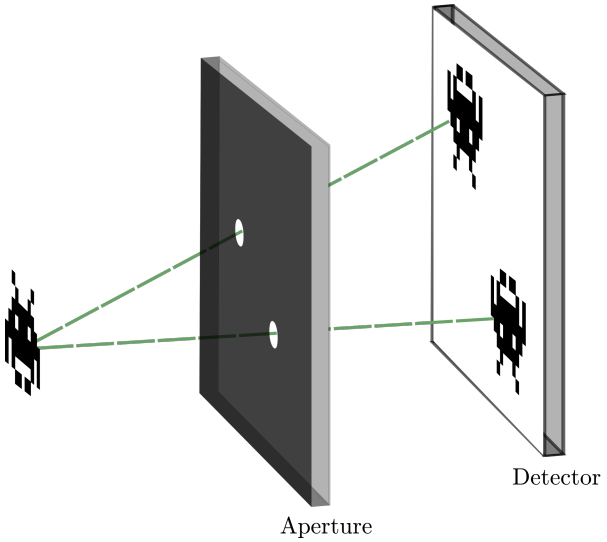

FIGURE 2.2. A schematic for imaging with a grand array of two perforations. Light (green) from the source (space invader) is imaged through the perforations on the aperture to form two inverted projections of the source on the detector. The separation of the perforations is sufficiently large to prevent overlap of the two source projections.

In order to quantify this signal increase, the signal to noise ratio (SNR) is often used in the form[109]:

$$\mathrm{SNR}_j = \frac{\lambda_j}{\sigma_{\bar{j}}} \tag{2.9}$$

where j is the set of detector pixels where the source is expected to create signal, λ is the sum of signal strength across j, and $\sigma_{\bar{j}}$ is the standard deviation of all detector pixels not in j. The set of $\bar{j}$ will be defined as the background for the image.

For a grand array of n perforations, the theoretical SNR increase will be $\sqrt{n}$. However, it is not practical to increase n *ad infinitum*. For a finite detector area, there will be a limit on n scaling with source size and perforation diameter, in order to ensure images are kept separated spatially. This often results in large detectors being used, which puts a monetary cost on the SNR increase.

2.3 Coded Apertures

Coded apertures are a form of pinhole array that do not require the images on the detector to be spatially separated. Instead, the projections on the detector are allowed to overlap, *encoding* information about the source in signal that is not visually representative of the distribution, as shown in figure 2.3. Henceforth, this detector signal will be referred to as a *hologram*. Negating the need to have separated projections allows for a higher density of perforations on the aperture, and therefore a higher signal throughput to the detector. This can occur without having to increase the size of each individual perforation, and therefore total signal is not a function of resolution capability, as it is with the grand array and single pinhole. The encoded hologram will require post-process decoding to form a reconstructed image of the source. It is worth noting that the image produced is a reconstruction, and as such there is a possibility for artefacts from decoding to be produced that are not present in the real source place.

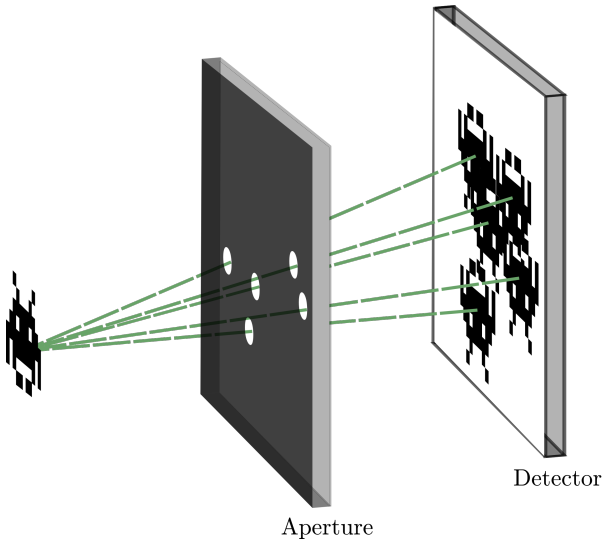

FIGURE 2.3. A schematic for imaging with a coded aperture of five perforations. Light (green) from the source (space invader) is imaged through the perforations on the aperture to form five inverted projections of the source on the detector. The projections are overlapping, resulting in a detector hologram that is not visually representative of the source.

Coded apertures allow for more perforations per unit detector area than the grand array, and

therefore a theoretically a higher SNR per unit detector area. The exact SNR will depend on the coded aperture design chosen, as many exist[4,110–115]. As such, comparison of SNR between coded apertures and grand arrays will be revisited once aperture designs have been discussed.

Originally, coded apertures were designed for indirect x-ray star photography[116] using concentric zone plates as an aperture design that could then be decoded optically. This was later developed by Dicke to square perforations randomly distributed cross the aperture as shown in figure 2.4, that allow for algorithmic decoding instead of optical, increasing resolution capability[110]. Due to their use in astrophyisics for imaging, the original literature often uses the assumption that all incident particles are parallel, from a source that can be considered to be infinitely far from the aperture.

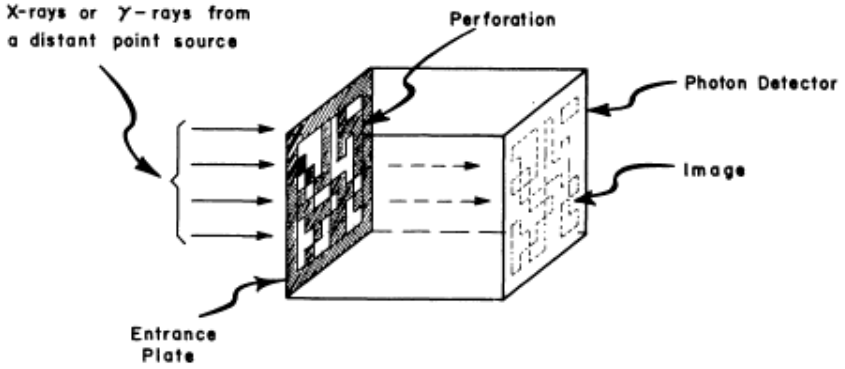

FIGURE 2.4. The first coded aperture with square perforations, designed by Dicke[110]. The array elements are randomly distributed, and the system has no magnification due to the vast distance from source (stars) to aperture.

2.3.1 Hologram Encoding

The generation of the hologram, D, can be seen in figure 2.3 as the overlap between every source projection on the detector. This can be expressed mathematically as a convolution between the source, S, and the aperture function A:

$$D[i,j] = \int_{x=-\infty}^{\infty} \int_{y=-\infty}^{\infty} S[x,y] \cdot A[i-x, j-y]\, dx\, dy \tag{2.10}$$

where A is a binary array, with 1 and 0 denoting a perforation and substrate, respectively. The $[i,j]$ coordinate system is in the detector plane, D, with the $[x,y]$ being coordinates in plane S. Henceforth $\boldsymbol{s} = [x,y]$ and $\boldsymbol{d} = [i,j]$ for ease of notation.

Equation 2.10 assumes an infinite plane for the detector and source, which is unphysical. Digital detectors, such as charged coupled device (CCD) and complimentary metal oxide semiconductor (CMOS) cameras, are all pixelated and cannot be described by a continuous planes.

Analogue particle detectors, such as image plate, will require digitisation through scanning to analyse and decode. The digitisation process will also pixelate the results, and thus the encoding process can be described discretely as:

$$D_{\boldsymbol{d}} = \sum_{\boldsymbol{s}} S_{\boldsymbol{s}} \cdot A_{\boldsymbol{d}-\boldsymbol{s}} \tag{2.11}$$

For laboratory imaging, the assumption cannot be made that incident particles are all parallel. The system will be affected by magnification, as with the single pinhole model. Therefore the hologram is not just a function of S and A, but also system magnification and relative pixel sizes on the aperture and detector (A_{pix} and D_{pix} respectively):

$$n = (M+1)\,\frac{D_{\text{pix}}}{A_{\text{pix}}} \tag{2.12}$$

where a single pixel on A is expanded into $n \times n$ pixels on D. In order for equation 2.11 to have magnification included, a scaled aperture array A' must be used. A' has the same pattern as A, with the length and width increased by a factor of n, and each individual pixel of A expanded into $n \times n$ pixels on A'. The hologram with magnification included can then be expressed as:

$$\begin{aligned} D_{\boldsymbol{d}} &= \sum_{\boldsymbol{s}} S_{\boldsymbol{s}} \cdot A'_{\boldsymbol{d}-\boldsymbol{s}} \\ D &= S * A' \end{aligned} \tag{2.13}$$

with $*$ being the convolution operator.

2.3.2 Undersampled and Oversampled Regimes

Coded apertures can be used in two differing regimes, as depicted in figure 2.5. The undersampled approach assumes that the detector is larger than the projection of the aperture, while the oversampled assumes the detector is the exact size or smaller than of the aperture projection[117]. Both regimes assume that there is no angular offset between the aperture and detector - if the aperture pixels do not project and map cleanly onto the detector pixels, the hologram will not be well represented on the pixel array D. This is an experimental constraint not found for single pinholes or a grand array, as the perforation redundancy is not used to form the source image.

Undersampling is a more versatile approach, as the aperture to detector distance is not required in designing the aperture size. Furthermore, the solid angle for possible incidence from the source on the aperture is larger, yielding a larger field of view for the system. However, this is at the cost of wasted detector area, with parts of the detector not collecting useful signal.

In contrast, oversampling is more efficient for signal on the detector, with the entire detector in use. It requires a *mosaic* of the aperture about itself, to enable imaging of sources not along the central axis. This involves copying the $r \times s$ aperture about itself to model A as a quasi-continuous function, to form an $(2r-1) \times (2s-1)$ full aperture. This has been shown in figure 2.6. The

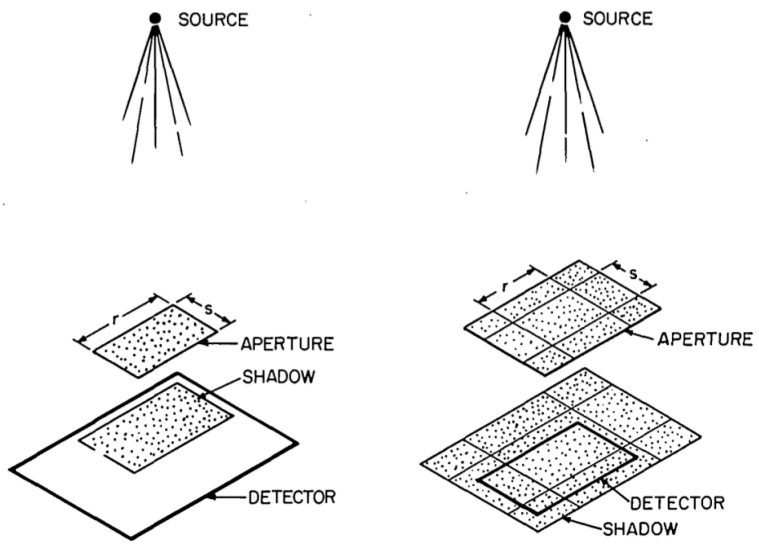

(a) Undersampled System (b) Oversampled System

FIGURE 2.5. A schematic depicting the two experimental geometries; (a) undersampled and (b) oversampled. Dimensions r and s are the dimensions of the aperture design. Figure reproduced from Fenimore and Cannon[117].

aperture and detector size, as well as the distance between them, needs to be carefully regulated such that only a single iteration of A is projected onto the detector at any one time to prevent aliasing. Due to the more efficient use of detector area, the oversampled system will be used in this work, unless stated otherwise.

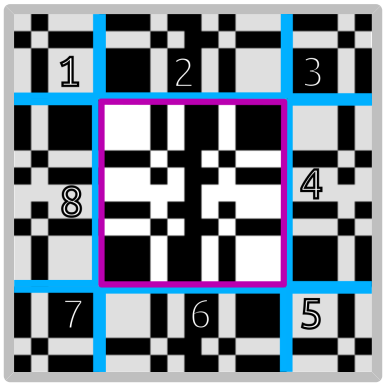

FIGURE 2.6. A depiction of mosaicing using an 11×11 coded aperture. The basic pattern (purple) is mapped onto a 21×21 grid, with the basic pattern in the centre. Copies of the basic pattern (blue, 1 – 8) are placed around the border to extend the aperture quasi-continuously.

2.3.3 Image Decoding

As encoding is a convolution, the decoding from hologram into source reconstruction, $\hat{S}$ will also be a discrete convolution operator. Due to the inversion of the source projection with respect to the original source, decoding is performed with a cross correlation, which is identical to a convolution and reflection:

$$\begin{aligned} \hat{S}_{\boldsymbol{s}} &= \sum A \sum_{\boldsymbol{d}} D_{\boldsymbol{d}} \cdot G_{\boldsymbol{d}-\boldsymbol{s}} \\ \hat{S} &= \kappa(D \star G) \end{aligned} \tag{2.14}$$

where κ is the total number of perforations in the design, G is referred to as the decoding function, and $\star$ is the cross correlation operator. The form of G depends on the aperture design used, which will be discussed in the next section. However, it will always have some dependence on A', and the ability for G to accurately reconstruct the source with low noise is paramount to the efficiency of the imaging system. The normalisation with κ is to ensure the reconstructed image has comparable intensity to the original source.

Conceptually, equation 2.14 is a moving dot product; G is overlaid atop D with some translation, and the dot product calculated. Then G is rastered across D such that every possible overlap is covered. However, due to the computational expense of rastering large dimensional arrays across one another, equation 2.14 is often computed using fast Fourier transform methods, which will be discussed in chapter 3.

2.4 Coded Aperture Design

Substituting equation 2.13 into 2.14:

$$\hat{S} = \kappa \left(S * A'\right) \star G \tag{2.15}$$

Applying convolution associativity[118]:

$$\hat{S} = \kappa S * \left(A' \star G\right) \tag{2.16}$$

Therefore, if A' and G can be created such that their cross correlation is a delta function (a function with a single spike of intensity 1 at its centre, and 0 signal everywhere else), the convolution with S will still be identical to S. Thus, the criterion for optimal coded aperture imaging has been derived:

$$\begin{aligned} &\textbf{if} \quad A' \star G = \delta \\ &\textbf{then} \quad \frac{1}{\kappa}\hat{S} = S \end{aligned} \tag{2.17}$$

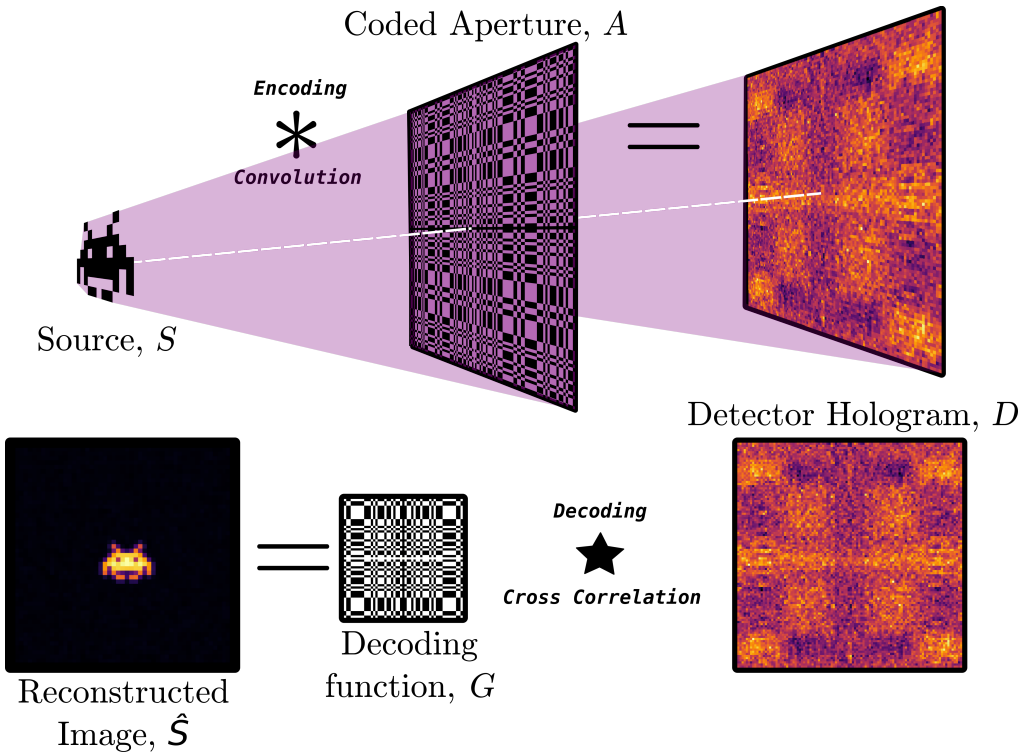

FIGURE 2.7. An example of the coded aperture process. A source, S is projected through each perforation on the aperture, A, and encoded (mathematically expressed as a convolution) onto the detector as the hologram, D. The hologram, D is then decoded (mathematically expressed as a cross correlation) with the decoding function, G, into a reconstruction of the source, $\hat{S}$. Here, a $p53$ MURA has been used as the aperture design and decoding function, which will be explained in section 2.4.5.

As G is usually constructed as a function of A', the aperture design is therefore key in reducing noise levels within $\hat{S}$.

2.4.1 Point Spread Function

The point spread function (PSF) will be used to quantify the ability for an A' and G combination to reconstruct a δ function, and therefore their ability to accurately reconstruct a source. This is the signal of $\hat{S}$, reconstructed from the hologram of a perfectly centred point source infinitely far away. This can be constructed through a cross correlation:

$$\text{PSF} = A \star G \tag{2.18}$$

without the need for simulation or experiment to produce D for the point source. This will generate a reconstructed image reliant purely on the efficiency of the decoding process, which is the purpose of the PSF. The PSF will be a two dimensional image, but coded aperture literature[111,112,117,119]

takes a lineout of the PSF through the origin to highlight the noise more readily, looking at the background structure and fluctuation.

It is worth noting that literature has varying definitions of the PSF for a coded aperture depending on the discussion; these include the detector response to a point source[120], and the decoded point source from D[119]. Here, the latter definition is used. The following discussion on varying aperture designs assumes an A of 40×40 elements[119].

2.4.2 Randomly Distributed Array

Dicke's original coded aperture (originally called a scatter-hole camera) was constructed with perforations along a random distribution[110] with an open aperture fraction (the fraction of aperture area that is perforated) of 0.5, and decoded through an autocorrelation where $G = A$. The cross section can be seen in figure 2.8, with a result far from a δ function. The peak of 800 counts is expected, as it equals the total number of perforations in A, but the decoding noise is high, with a maximum of 400 counts. Two components of noise are present - a high frequency quasi-random fluctuation, atop a low frequency pyramidal drop-off.

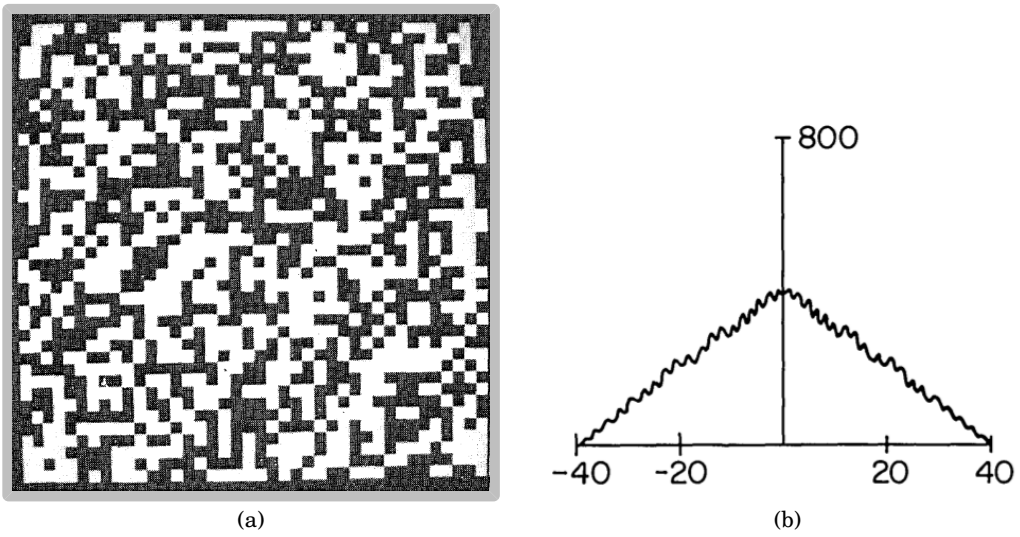

FIGURE 2.8. The (a) aperture and (b) cross section fo the PSF for perforations randomly distributed across a coded aperture of 40×40 elements with exactly 50% perforated, and decoded using $G = A$. The peak signal is the central 800 counts, with the largest magnitude of the noise is equal to 400 counts. Figure reproduced from Fenimore and Cannon[117].

The low frequency noise arises from A and G being binary. Assuming the distribution of perforations across A is quasi-uniform, the expectation value for any sub-section of A will be half its area. Thus, the expectation value of the cross correlation of two randomly distributed apertures will be a quarter of the overlapping area. Using the conceptualisation of a moving

dot product for the decoding of equation 2.14, it can be seen that there will be a variation in overlapping area, and therefore expectation value, as G is rastered across A.

Fenimore and Cannon[117] suggest the use of a unimodular (-1, +1) decoding function instead of the binary (0, 1). G is constructed from the same pattern as A, with all of the 0 values being substituted for -1. The expectation value of this unimodular G is now 0, and will not vary as a function of sub-sectional area, under the assumption that the perforation distribution is quasi-uniform. The effect on the SPF can be seen in figure 2.9, with the low frequency noise being removed. Now, the high frequency noise is centred about 0.

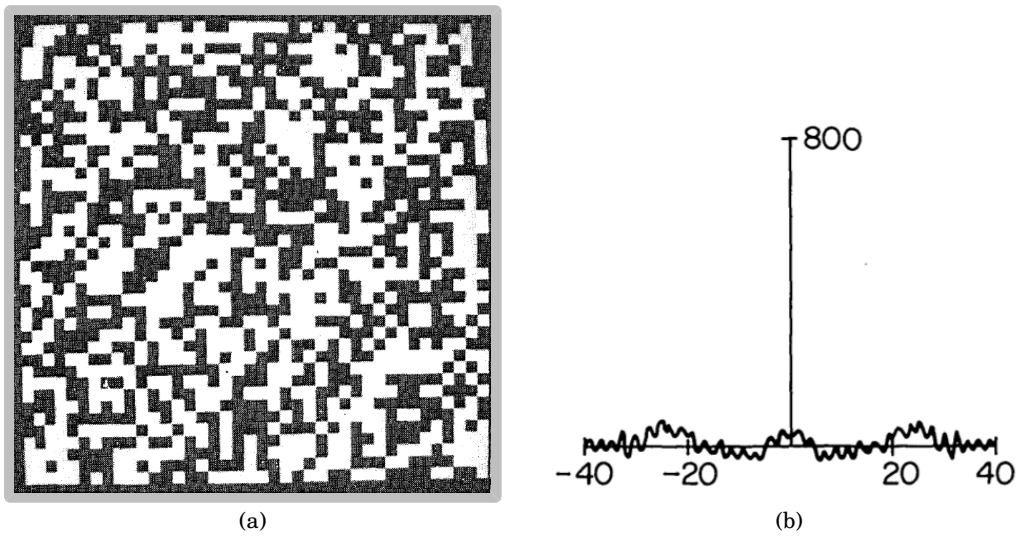

(a) (b)

FIGURE 2.9. The (a) aperture and (b) cross section of the PSF for the same random aperture as figure 2.8, using a unimodular G. The peak signal is the central 800 counts, with the high frequency noise preventing it being a δ function. Figure reproduced from Fenimore and Cannon[117].

It is worth noting that negative values are now possible within $\hat{S}$, showing anti-correlation between D and G. The negative signal strength can be as large the intensity of the source is positive, if the hologram is perfectly anti-correlated with A. Negative values in $\hat{S}$ are unphysical when comparing coded apertures to single pinhole systems, and some literature discusses their removal in post-preprocessing and setting all values below 0 to be 0[121].

It can be seen that the unimodular G has reduced the low frequency decoding noise between figures 2.9 and 2.8. However, the high frequency is still prevalent, and preventing the PSF required for criterion 2.17. There are three interconnected causes for this; perforation separation, patterns, and density.

It can be seen from the moving dot product conception of cross correlation that A cannot hold translational symmetry. Else, as G is rastered across A, each area of translational symmetry will create an artefact within the PSF, and a ghost image of the source in $\hat{S}$. The strength of

the artefact signal in the PSF will scale as the area of the repeated pattern in A, with the simplest case of translational symmetry being regularly spaced perforations. Figure 2.10 depicts this source of decoding error for regularly spaced perforations. The translational pattern of the perforations in (a) creates identical holograms for both the black and grey source, and in decoding will show correlation with both positions. It is only by using an irregularly spaced perforation distribution in (b) that unique holograms will be formed for the two sources.

While regular perforation distributions are detrimental to decoding accuracy, uniform perforation density will prevent signal bias from sections of the source plane. If there is a gradient in perforation density, it can no longer be assumed that the expectation value for a subset of $G = 0$. If the expectation value of the subset fluctuates, then so too will the cross correlation with A, and high frequency fluctuations will appear in the PSF.

However, when using a randomly constructed aperture, it is statistically unlikely that it will hold no translational symmetry, irregular perforation distribution, and uniform perforation density. Instead, a repeatable construction method is required that can satisfy these three conditions.

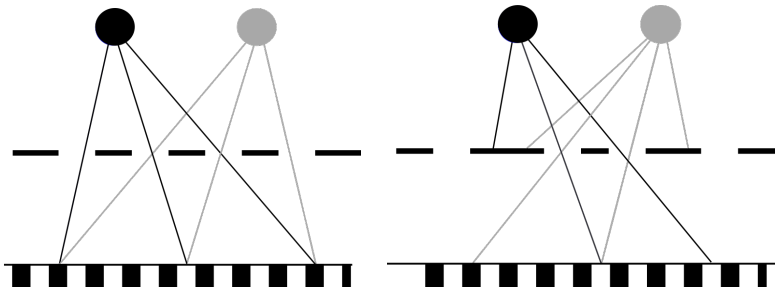

(a) Regular Perforation Distribution (b) Irregular Perforation Distribution

FIGURE 2.10. A simplified depiction comparing possible sources of decoding error from perforation distribution within a coded aperture. Particles from two possible source positions (black and grey) are traced through an aperture of (a) uniform and (b) irregular perforation distribution onto a pixelated detector. Without prior knowledge, the detector positions in (a) are unable to differentiate the two possible sources.

2.4.3 Non-Redundant Array

The first such solution is the non-redundant array (NRA)[117]. This is an array where the vector separation between any two perforation locations (the redundancy) is unique. This prevents the regular perforation separation, and the resultant aliasing. This is at the expense of open aperture fraction, as 0.5 is unattainable with the constraint of non-redundancy. The construction of an NRA is ill-defined in literature, but can be constructed for any prime number (or square of a prime) basis, p [122], and mapped onto an $r \times s$ dimensional array with $p - 1$ perforations. Not all

p values are suitable imaging purposes, as s can be as low as 2 and generate long thin aperture designs.

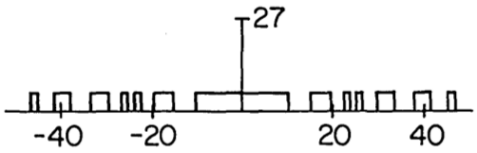

FIGURE 2.11. A cross section of the PSF for a non-redundant coded aperture of 40×40 elements. This was then decoded as a function of the aperture design, A. The peak signal is the central 27 counts, and the noise is uniform and of known magnitude. Figure reproduced from Fenimore and Cannon[117].

The PSF of an NRA can be seen in figure 2.11, with the peak of 27 counts being the number of perforations in the aperture. Although not a δ function the background is flat and of known magnitude, 1 for the PSF, and is a function of A, without randomness. NRAs are used among some medical imaging groups[123], and for sources with large gradients in emission properties[124], although their use is not ubiquitous[125]. The open fraction of 0.017 for figure 2.11 prevents the same signal increase of the 0.5 open fraction NRA.

2.4.4 Uniformly Redundant Array

1D arrays with uniform and known autocorrelations have been utilised within communication and signal processing since the 1950's, designed for military anti-jamming of tactical communications[126]. A pseudo-noise (PN) sequence has a periodic autocorrelation, with a period equal to the length of the array, L. The binary array of the PN sequence holds one more logic values of 1 than 0[127], and hence an expectation value of approximately 0.5 for large L. In the special case where L is a prime number, and can be expressed as:

$$L = 2^n - 1 \tag{2.19}$$

where n is any positive integer, and the autocorrelation becomes uniform:

$$\text{PN autocorrelation}[i] = \begin{cases} 0 \text{ when } i = 0 \\ -1/p \text{ otherwise} \end{cases} \tag{2.20}$$

PN sequences with a prime p possess a *window property*, where any non-zero 4 digit tuple will occur only once. Such sequences can also be created in 2D with the same properties[128], for an array of size $s \times r$ where:

$$L = sr = 2^n - 1 \tag{2.21}$$

and r and s are co-prime, meaning they share no common denominators besides 1. L is the 1D PN sequence which is then translated into 2D. As L is not prime, the 1D form does not produce the window property, yet r and s being co-prime forms the window property in 2D, with no non-zero 2×2 tuple being repeated. The expectation value of the 2D PN sequence is still approximately 0.5.

Fenimore and Cannon found that, by taking the PN sequence where $r - s = 2$ and applying a cyclic permutation, the redundancy is uniform[117]. That is, the vector separation between any two perforations occurs α times across the array, where α is constant across all included vector separations. The cyclic permutation assumes the PN sequence is periodic, and translates [0,0] into the centre of the $r \times s$ array. This family of designs are known as uniformly redundant arrays (URA). Due to the number of logic values of 1 and 0, the expectation value of G becomes 1, not 0 as with the random aperture.

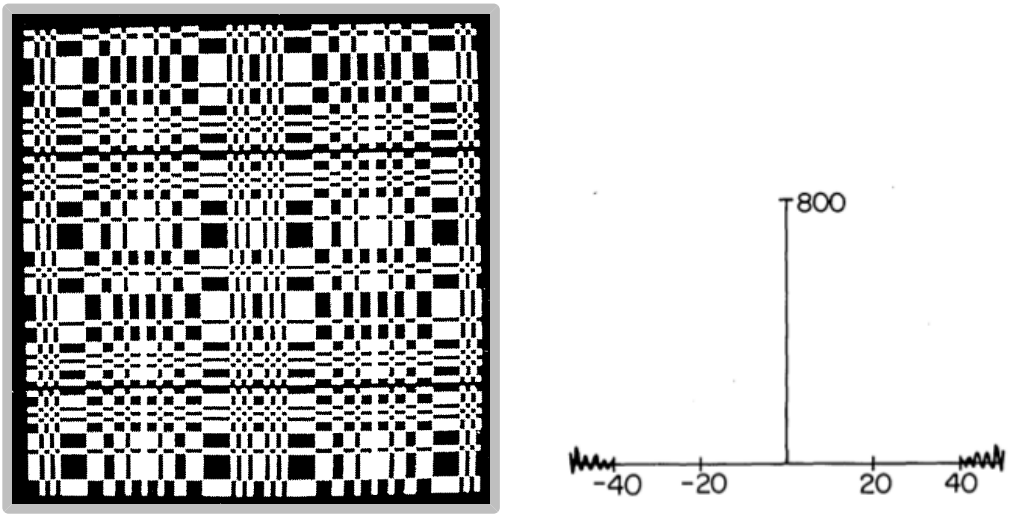

(a) (b)

Figure 2.12: The (a) aperture and (b) cross section of the PSF for a URA coded aperture, of 43×41 elements. The URA has been mosaiced into a $2r \times 2s$ aperture. This was then decoded as a function of a unimodular G. The noise only occurs ± 41; beyond the edges of the aperture, and thus the 800 count signal is a δ function for the aperture area. Figure reproduced from Fenimore and Cannon[117].

The PSF for a URA can be seen in figure 2.12, with a δ spike with no noise within the bound of ± 41. This is the first array to satisfy criterion 2.17, and theoretically produce reconstructions of a source without the presence of decoding artefacts. The requirement for $r - s = 2$ always produces a quasi-square URA, which is beneficial for 2D imaging.

Both grand arrays and coded apertures are used within similar fields, with the former favoured for ICF neutron imaging[129], and the latter for radiation leaks from nuclear reactors[4]. The benefits of coded apertures discussed above all rely on an aperture being manufactured without imperfection. The URA in figure 2.12(a) highlights the challenge of doing so, with a

complex pattern where sections of substrate are often not connected to one another. When imaging particles that require metal substrates, mounting such a URA can be an experimental difficulty. When moving to high-energy high-resolution imaging, the high substrate thickness and small perforation diameter required makes coded apertures difficult to manufacture without imperfection that could compromise the PSF of the design.

Comparisons between grand arrays and URAs have been discussed by Wagner, showing a URA does not have the same SNR increase per perforation as a grand array[129]. Therefore for an infinite detector plane, a grand array will outperform the SNR of a URA. However, when using a finite detector area, the higher perforation density of the coded aperture will allow for a higher SNR increase per unit detector area than a grand array.

The family of URA designs available is sparsely populated because of s and r needing to be relatively prime and $r - s = 2$. For large values of r, the likelihood of $r - 2$ being relatively prime to r decreases. However, for the oversampled imaging regime matching between aperture design and detector dimensions is important. As most detectors are off-the-shelf, without input from the experimentalist on active detector area, it is more useful to have a larger family of coded aperture designs available when designing an imaging system. For $r, s < 100$, only 8 possible URA designs exist[112].

2.4.5 Modified Uniformly Redundant Arrays

Instead of the near-square URA, a modification can be made such that $r - s = 0$ to make a perfectly square array. In order for r and s to still be relatively prime, $r = s =$ a prime number, p. Gotesmann and Fennimore created as new family of coded apertures with this modified URA (MURA), where a design can be created for any prime number, p, on a $p \times p$ array[112]. This expands the size of the family, with 24 possible MURA designs for $p < 100$. The element-wise construction can be written as:

$$A_{ij} = \begin{cases} 0 & \text{if } i = 0, \\ 1 & \text{if } j = 0,\ i \neq 0, \\ 1 & \text{if } C_i C_j = +1, \\ 0 & \text{otherwise} \end{cases} \tag{2.22}$$

before the cyclic permutation is performed. C_α is defined as:

$$C_\alpha = \begin{cases} +1 & \text{if } \alpha \text{ is the quadratic residue modulo of } p, \\ -1 & \text{otherwise} \end{cases} \tag{2.23}$$

where the quadratic residue modulo is tested for i and j independently. This is performed by iterating through each positive integer, $\beta < p$, and evaluating whether the square of the integer divided by p is equal to the index:

$$\alpha = \left.\frac{\beta^2}{p}\right|_{\beta \in \mathbb{Z} < p} \tag{2.24}$$

A' is not required to manufacture A, and instead A_{pix} can be increased by a factor of n from equation 2.12. For computational ease, G can be constructed from A, and then converted to G' through the same single pixel expansion into $n \times n$ pixels. Before this magnification adjustment, G is constructed from A pre-cyclic permutation:

$$G_{ij} = \begin{cases} +1 & \text{if } i+j=0, \\ +1 & \text{if } A_{ij}=1,\ i+j\neq 0, \\ -1 & \text{if } A_{ij}=0,\ i+j\neq 0, \end{cases} \tag{2.25}$$

and then the cyclic permutation is applied to both A and G, before the latter is expanded to G'. For an oversampled system, A is then mosaiced onto a $(2p-1)\times(2p-1)$ aperture design, with an example aperture and corresponding decoding function ae shown in figure 2.13. The construction equations are discussed in depth within the literature, such as Gottesman and Fenimore[112].

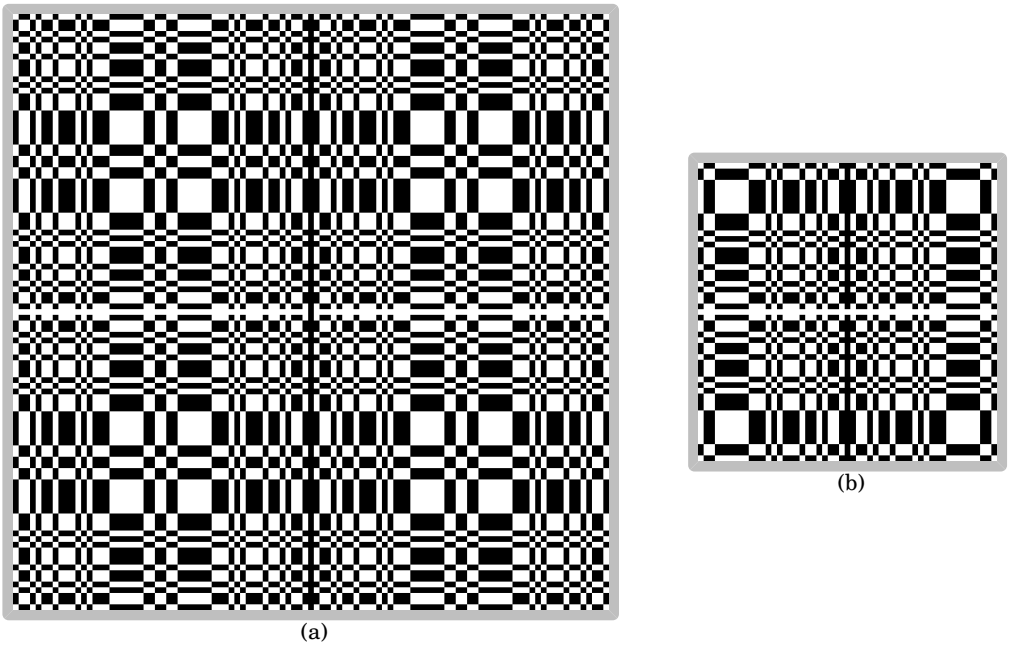

(a) (b)

Figure 2.13: A $p53$ (a) mosaiced A and (b) unimodular G using the construction of equations 2.22 and 2.25.

One useful feature of the cyclic permutation of the MURA is the central row of the aperture is all perforation, and the central column is all substrate. This will be referred to as the aperture *cross-hair*. Assuming the perforations are optically transparent, the cross-hair from a projected point source can be used as calibration for the system to remove angular offsets between aperture and detector.

The MURA has a quantifiable SNR, defined by:

$$SNR_j = \frac{\kappa \lambda_j}{\sqrt{\kappa \lambda_j + \sum_{\boldsymbol{d}} D_{\boldsymbol{d}}}} \tag{2.26}$$

where j is the set of pixels in $\hat{S}$ where the source is expected to create signal, λ is the sum of signal strength across j, and κ is a normalisation term of the total perforation count, as per Dicke[110].

2.5 Particle–Matter Interactions

When considering classical aperture imaging techniques for low-energy particles, the assumption is made that the substrate will highly attenuate incident particles that interact with it. However, with high-energy particles this assumption is not always correct. Using the example of the NIF neutron imaging aperture, the 20 cm gold substrate is not designed to attenuate incident neutrons. Instead, it is thick enough that the total length is multiple mean free path lengths for 14.1 MeV neutrons, and any neutrons interacting with the substrate should scatter at least once. After the 30 m flight distance from aperture to detector, the vector of any neutrons scattered by the substrate will not intersect with the detector. This effectively removes neutrons incident on the substrate from the imaging system, without the necessity for low probability neutron absorption reactions.

Multiple mechanisms of scatter and attenuation can occur as a function of substrate density, ρ, substrate atomic number, Z, incident particle type and incident particle energy. In this work, imaging of high-energy photons and neutrons is discussed, and as such their particle–matter interactions are advantageous to understand.

2.5.1 Photons

In order of ascending incident photon energy, the four main interaction mechanisms for the keV to MeV photons with matter are Rayleigh scattering, photoelectric effect, Compton scattering, and pair production.

Rayleigh scattering is an elastic process in which the photon interacts with the charge distribution about an atom, with insufficient energy to displace any one electron. Thus, this occurs for low photon energies below roughly 20 keV, as above this an electron would be freed during the collision. The photon scatters without causing atomic excitation or ionisation[130] and predominantly in the forward direction, but backscatter can occur if the collision with the atom has an incident angle of 0°. The cross section of interaction scales linearly with Z[131].

The photoelectric effect is an absorption mechanism which is important for photon energies less than 100 keV. When colliding with a bound electron, the photon energy is greater than the binding energy and the electron is displaced, absorbing the photon in the process. A higher shell

electron will relax down to fill the shell vacancy, and emit a photon of characteristic wavelength from the discrete energy differential between the shells. The direction of this photon emission is independent of the incident photon, and the energy is often in the low keV range which will be reabsorbed within the material. The cross section of interaction scales with ρ and Z^3 [131].

Compton scatter is a similar process to the photoelectric effect, where the incident photon collides with a bound electron, and imparts more energy in collision than the binding energy - thereby displacing the electron. However, the incident photon energy is sufficiently large (30 keV to 5 MeV) that the photon scatters during the collision, instead of being absorbed. As the photon energy is in excess of the binding energy, Compton scattering cross section is independent of Z, but does scale with the electron density of the material [131].

The mechanisms of pair production have been discussed previously in section 1.1.2, where an incident photon generates an electron positron pair, the latter of which will annihilate with an electron to produce an entangled pair of 511 keV photons. This only occurs with incident photons over 1.022 MeV, and the scaling with ρ and Z is dependent on the mechanism [54–57].

2.5.2 Fast Neutrons

Fast neutron interactions with matter are predominantly via scatter mechanisms with nuclei, both elastic and inelastic. Both mechanisms are interactions with nuclei, and as such the cross sections scale with ρ as per unit are a denser material has either more nuclei, larger nuclei, or both. Thus there is a greater potential for interaction to occur between the neutron and a nucleus.

Elastic neutron scattering conserves kinetic energy before and after the collision, and is dominant for incident neutrons below 10 MeV. Lighter (low Z) nuclei are often used as neutron moderators because of the elastic scatter properties, as the neutron can impart more kinetic energy to the nuclei, and as such the recoiled neutron has lost energy in the collision [132,133]. Over multiple mean free paths, it is possible for the neutron to be absorbed in the bulk material, or to be moderated to a degree where a time gated detector can remove them from data acquisition.

Inelastic neutron scatter does not conserve kinetic energy, and the incident neutron interacts with the nucleus. The nucleus enters an excited state and emits gamma rays in order to relax back down to ground state, and a neutron of lower energy leaves the collision. It is possible for multiple neutrons to be emitted in this process, usually with higher incident neutron energies. The energy required to reach the first excited state of a nuclei decreases as Z increases, and thus species with a higher Z are more likely to scatter inelastically [132,133].

CHAPTER 3

METHODOLOGY

Various codes and techniques have been used to perform this research, with a majority of the presented work originating from Geant4 Monte Carlo simulations, C++ ray tracing simulations and analysis, or Python analysis scripts. Here, the techniques used will be discussed, and the linking employed between these programs.

3.1 Decoding Efficiency

The cross correlation of equation 2.14 used for image decoding is computationally inefficient. To code it as written would require 4 nested loops in i, j, x and y. The number of iterations scales roughly as p^4, which for the $p53$ example aperture of figure 2.13(a) would be *ca.* 10^7 iterations. Most computational codes use a fast Fourier transform (FFT) to speed up processing time[134].

Fourier transforms are able to compute a correlation due to convolution theorem, stating that a convolution is equivalent to a multiplication in the frequency domain:

$$\mathscr{F}[D \star G] = \mathscr{F}[D]\mathscr{F}[G] \tag{3.1}$$

where $\mathscr{F}$ denotes a Fourier transform[135]. For the two dimensional case of array ᛟ, the Fourier and inverse Fourier transforms are described as:

$$\begin{aligned} \mathscr{F}\left[\text{ᛟ}_{x,y}\right]_{u,v} &= \sum_x \sum_y \text{ᛟ}_{x,y} e^{-i2\pi(ux+vy)} \\ \text{ᛟ}_{x,y} &= \sum_u \sum_v \mathscr{F}\left[\text{ᛟ}_{x,y}\right]_{u,v} e^{i2\pi(ux+vy)} \end{aligned} \tag{3.2}$$

where $[x,y]$ and $[u,v]$ are the coordinates in real space and frequency space, respectively.

Therefore, the cross correlation can be computed in Fourier space, and then the inverse Fourier transform applied to return to real space. Performing the 3 Fourier transforms required to compute equation 3.1 would not increase the speed of calculation without using a FFT method, where the signal can be split into smaller sub-signals, and the Fourier transform of these computed separately in parallel. Then, the resulting sub-signals can be recombined to form the transformed signal[136].

It is noted that a similar approach could be used for the i, j loop of the direct cross correlation. However, this will always be more memory inefficient than the FFT method, as it will require a copy both full sized signals to exist in every parallel process. The convolutions and cross correlations used here are all computed using the FFT method, either through Python library SCIPY[134] or C++ library OpenCV[137].

3.2 Geant4

Geant4 is a Monte-Carlo simulation toolkit for the interactions of particles and matter, written in C++[138]. It can be programmed for custom "world" setups, particle geometries, momenta, and active detectors in an attempt to simulate experiments as accurately as possible.

Here, Geant4 version 10.5.0 has been used on an Unbuntu 16.04 linux machine with the following flags (which are predominantly for visualisation):

- DG4INTY_USE_XT
- DG4VIS_USE_OPENGL
- DG4UI_USE_TCSH
- DG4INTY_USE_QT
- DG4UI_USE_QT
- DG4VIS_USE_OPENGLQT
- DG4VIS_USE_RAYTRACERX
- DG4VIS_USE_OPENGLX
- DG4MULTITHREADED
- std=c++11

with the simulations use the EM standard model package, using the following model packages for particle interactions:

- G4LivermorePhotoelectricModel
- G4RayleighScattering
- G4UrbanMscModel for electron and positron scattering
- G4WentzelModel and G4eCoulombScatteringModel, but only used here for protons that may be generated within the simulation

The physics package for incident neutrons is QGSP_BERT. This uses a Bertini cascade for primary neutrons, with results between 1 MeV and 10 GeV agreeing closer with experimental data than other models within Geant4. It is noted that QGSP_BERT_HP could be used in the future, for even more accurate calculations for the 1 to 20 MeV neutron range, at a cost of run time and code performance. The decector package used is G4SensitiveDetector, and stored in 1D and 2D histograms before comma separated value (CSV) output.

3.2.1 Code Flow

Geant4 works by creating "runs" of multiple particles, and simulating their path through matter. Each time a particle interacts with matter, or the boundary between matter, an "event" occurs. Multiple runs can occur in one simulation, and the initial number of events (particles) varied. The general flow for a Geant4 simulation can be split up into the following sections:

Initialisation - Starting the way in which the simulation will be run. Defining variables such as which physics package to use, whether to run a visualiser during simulation, seeding random number generators and multithreading. Although Geant4 does not utilise command line `argv` and `argc` input, this is where it is passed into the simulation. This occurs once per simulation.

World Construction - Defining the constraints, materials, shapes and properties of everything the particles could interact with. The "world volume" is the total volume over which the simulation will be run, and within which is every object or cavity resides. Properties of many known materials are included, and composites can be constructed from their atomic constituents. Here, active materials can be defined to be used as detectors - referred to as "sensitive". This occurs once per simulation.

Particle Initialisation - Defining the particles to be simulated, such as their origin, momenta and type. This can be changed via a Geant4 input deck, but defaults can be coded in when no information is provided in the input deck. This occurs once per run.

Run Action - A single run begins. This tracks all the events occurring within the run, and moves between them. Sensitive detectors only read for individual runs, and at the end of the run the detector histogram is exported. Therefore, multiple runs will give multiple detector signals.

Event Action - Any interaction between particles and matter, or particles and other particles through mechanisms like pair production. The number of total events will be dependent on the amount of boundary changes and materials in the world volume, and the trajectory of the particles.

Hit Action - An event between a particle and a sensitive material. A class can be written to define how this event is logged, and thus defining the detector properties. Hit actions, or a custom variant, are the primary way of exporting data from Geant4. If the information is not collected in the hit action, it cannot be retrieved later.

3.2.2 File Passing

The Geant4 simulations written for this work are capable of taking file inputs for source shape, spectrum, and aperture design - with the latter being generated by the C++ program. These are all raw text files in three column format; x, y, and likelihood. All the x, y coordinates are in pixels, and then converted into physical sizes and locations inside Geant4 using a `pixel size` variable. It is noted that the Gaussian sources were generated within Geant4, and are not discretised into pixels like the other sources. Aperture files have a binary likelihood, with the substrate denoted 0 and a perforation 1.

Output into other programs is defined by Geant4 and its CSV class. The file format is 5 column:

1. Number of Entries
2. Sum of the Weighted entries
3. Sum of entires, Weighted^2
4. Sum of X (bin number) by Weight
5. Sum of X squared by Weight

where the row index is representative of the detector pixel, filling from [$x = 0$, $y = 0$] in the positive x direction. It is noted that an extra pixel is added to the start and end of every row and column for "overflow" - events that hit the volume but not within the bounds of the scored histogram. Here, a separate python script is used to unwrap the 1D list into a 2D array using known dimensions for the detector from the Geant4 build. This 2D array is then saved as a CSV to be imported into decoding and analysis scripts.

3.2.3 Aperture Construction

The aperture is constructed from a text input file, passed from either a C++ or Python script. A block of volume is defined for a single pixel of the aperture, with the correct substrate material, length and width A_{pix}, and the thickness of the aperture. This is then placed inside an aperture volume at every coordinate where the input file likelihood is 0 - denoting substrate. A 0.5% tolerance is added to the length and width to ensure no gaps were present between adjoining substrate pixels, and tested using a uniform parallel beam onto a high resolution detector.

A $0.1p$ pixel boarder is added to prevent particles circumventing the aperture and still hitting the detector. Once the aperture volume has been constructed, it can then be placed and rotated within the world volume as usual.

3.2.4 Maximum Particle Number

The variable used by Geant4 for the number of events to initialise is poorly documented. Examples describe the '`run/beamOn n`' command as the way to increase the number of particles initialised

in the simulation, with n being the number of particles. However, the documentation does not describe the variable type used to define n. Here, it was found that n is stored as a signed 32 bit integer, which has a maximum of 2^{31}, or *ca.* 2.1×10^{9}.

This is not always enough to simulate high flux environments, and documentation is lacking to explain how to simulate more particles. For others facing this issue, two possible solutions are suggested here. Firstly, multiple runs can be defined with the same particle type and energy. This will increase the number of particles present by the number of runs called. Secondly, multiple particles can be defined per initialised event. Using an unsigned integer for the number of particles per event, this can increase the maximum particle count by 2^{32}, to a new maximum per run of 2^{63}.

It is recommended that Geant4 developers should convert their n to an unsigned integer, as a negative particle number is unphysical and unnecessary to store. This would double the maximum n, and increase the absolute maximum number of particles per run by a factor of 2 to 2^{64}. Using a 64 bit unsigned integer would also be useful, as would having appropriate documentation so more people are aware that this is even a possible issue.

3.2.5 Command Line Input

Geant4 is designed to have variables hard-coded in, which can cause difficulty when searching thousands of lines of code and multiple files to change the correct variable. It is common to have a separate header file for variables, in order to collate frequently changed parameters in a convenient location. However, this requires the simulation to be re-compiled every time a variable is changed, which is inefficient for performing large parameter scans.

One possible solution is to have a raw text file in the source code directory with all the relevant variables. This text file is then read by the code to change parameters, and sweeps are performed from a bash script that increments the text file to change the desired variables, before running the simulation once more. However, this limits the code to being run linearly, with only 1 instance of the code being run at any time. If the code were run twice on two different processors, altering the text file for run 2 would alter the parameters for run 1 also, and change the results.

It is noted that one possible solution is to have multiple copies of the code across different directories, or having multiple text files with 1 file per simulation run. Multiple input files increases the risk of error within the coding process, accidentally calling the input file for the wrong parameters and assuming the results are for the intended parameters. Having multiple instances of the code across many directories is memory intensive and difficult to manage, with the potential for different directories to have older versions of the code and therefore not be a direct comparison between other points in the parameter scan.

The solution used here is a custom class to read, sort, and check variables from command line inputs, before assigning them to variables in the class which are called by the rest of the simulation. Input parameters are taken from argv and filtered to look for the input tag '--'

before the input name. Using switches, the first letter of the input name is evaluated, then the first letter of the option, and the following input value is evaluated to ensure it is reasonable. While the value check is not a robust user interface, it prevents negative thicknesses, decimal threads, or strings for expected numbers. Within the class, it is best practice to store the variables privately, with separate functions to return the variables when desired. This prevents values being changed by any means beyond the command line input class.

The limitation of the technique described is the necessity that the first letter of each input name or option is unique, giving a theoretical maximum number of variables to be 676. However, this is more than enough variables for the applications here, and the same process could be used with string matching instead of first letter evaluation ot expand the number of variables available.

```
Format in the format of: --<input name> <input vlaue>
Unchanged variables have default values stored.
To read these default variables, run command --varDefault

--- Input Names ---
List of input names and their inputs:
--Aperture:
Changes the Aerture parameters
option => type   -> coded, pinhole, none, or solid
option => pValue -> MURA length / configuration
option => unit   -> the unit distance of the aperture
option => sizePix -> the x,y size of 1 pixel (no unit)
option => z      -> the aperture thickness (no unit)
option = density -> Increase W density by this factor

--Detector:
change the Detector parameters
options => x, y, z -> Detector size (from the centre, no unit)
option => unit   -> the unit distance of the detector
options => i, j, k -> Total # bins per Dimension
option => spec   -> total # bins in Energy
option => E      -> Max. Energy (MeV) to detect

--Geometry:
change the geometry of the G4 simulation
option => phi    -> Rotation about the y axis (degrees)
option => theta  -> Rotation about the x axis (degrees)
option => unit   -> the unit distance of the entire world
option => S-A    -> distance Source to Aperture (no units)
option => A-D    -> distance Aperture to Detector (no units)

--Object:
change the properties of the Scattering Object
option => image -> pattern of the Scattering Object:
```

```
> subOption => pointSource
> subOption => blob (Gaussian)
> subOption => Arrow
> subOption => spaceInvader
> subOption => ghost
option => unit  -> the unit distance (mm, um, etc)
option => z     -> Thickness of the Object (no unit)
option => density -> Increase W density by this factor
option => scale -> Scale to increase the object by
option => phi   -> Rotation about the y axis (degrees)
option => theta -> Rotation about the x axis (degrees)

--Source:
change the source information
option => unit    -> the unit size
options => x, y, z -> minor change in source position (unit = aperture unit)
options => i, j, k -> source size (from the centre, unit = aperture unit)
option => energy  -> photon energy, in MeV
option => flux    -> number of particles
option => particle -> xray, positron or neutron
option => shaping -> true: shaped beam onto a foil, (object shape)
                  -> false: square beam onto shaped object

--multiThread:
changes parameters around parallelisation
option => threads -> the number of threads. Must be an int

--runName:
adds a prefix to all filenames created
prevents override of previous run data

--Printing :
change the printing functions, when verbose is being used
option => silence -> only print progress tracker  True/False
option => runAct  -> print on RunAction actions   True/False
option => eventAct -> print on EventAction actions True/False
option => stepAct -> print on SteppingAction actions True/False

--varDefault: display the default variables

--- Unit List ---
-> pc :parsec
-> km :kilometer
-> m  : meter
-> mm :millimeter
-> um :micron
-> nm :nanometer
```

```
82
83  --- Example ---
84  $ ./CASPA CASPA.in --aperture pValue 53 unit mm --object image blob
85    --multiThread threads 40 --printing silence true --runName exampleRun
86
87  M. P. Selwood. UoY YPI. 2020
```

Code 3.1: Example of Geant4 command line input options and syntax via custom class

Another limitation of using a class based system is multi-threading. When multiple threads are used to speed up the run-time of a code, the `argv` and `argc` variables are only passed into the master thread. Therefore the changed variables will only be changed in the master thread, and the submissive threads will run with the wrong variables when their interface classes are initialised.

To prevent this, a Myers singleton can be employed[139]. This is a technique for only allowing one instance of a class to exist per simulation, which is then accessed by each individual thread. Geant4 already implements Myers singletons for its classes to make them thread-safe. This is a mechanism by which each thread checks to see if an instance of the class already exists. If no class exists, one is created and initialised using the `argv` and `argc` variables from the command line input. If a class does exist, the thread is pointed towards that instance within the memory, and can access the relevant variables without creating a new instance. An example of the class header file code can be seen in listing 3.2.

```
1  class MPS_Interface{
2    public:
3        // Myers Singleton: threadsafe implimentation
4      static MPS_Interface& getInstance(){
5        return instance();
6      }
7
8      static void initialization(int argc, char** argv){
9        instance(&argc, &argv);
10     }
11
12   private:
13     // Myers singleton adapted for initial input
14     static MPS_Interface& instance(int* argc=nullptr, char*** argv=nullptr){
15       static MPS_Interface instance{argc, argv};
16       return instance;
17     }
18
19     // constructor //
20     MPS_Interface(int *argc, char ***argv); //constructor
21 }
22
23 // Call variables in other files //
```

```
24 MPS_Interface runVariables = MPS_Interface::getInstance();
```

Code 3.2: Example of Myers singleton implimentation, to make the MPS_Interface class thread-safe.

The thread-safe Myers singleton approach allows for multi-threaded simulations to be run both locally and on clusters such as Viking. The requirement for shared memory between all the threads does preclude the use of multi-node architecture. However, the speed increase is sufficient that with 40 cores on the Viking cluster a simulation of 10^9 neutrons can be performed in roughly 20 minutes, which is adequate for the purposes here. Furthermore, multiple runs can be initialised in parallel from a single job on a cluster, further decreasing parameter sweep run-time.

3.2.6 CAD Input

In order for apertures to be manufactured via laser machining, a computer aided design (CAD) drawing is required. It is prudent to simulate as close to the manufactured product as possible, and therefore using the same model for manufacture and simulation is a useful tool. Although Geant4 has GDML file inputs, the documentation is lacking. The relevant code to import CAD GDML files can be seen in listing 3.3, with an example of a CAD imported object in figure 3.1.

```
1 #include "G4GDMLParser.hh"
2
3 G4GDMLParser parser;
4 parser.Read("<FILE>.gdml");
5 G4LogicalVolume* spaceInvader = parser.GetVolume("CAD_volume");
6 // ALWAYS has to be CAD_volume //
7 G4PhysicalVolumeStore::DeRegister(parser.GetWorldVolume());
```

Code 3.3: CAD GDML file input to Geant4 world volume

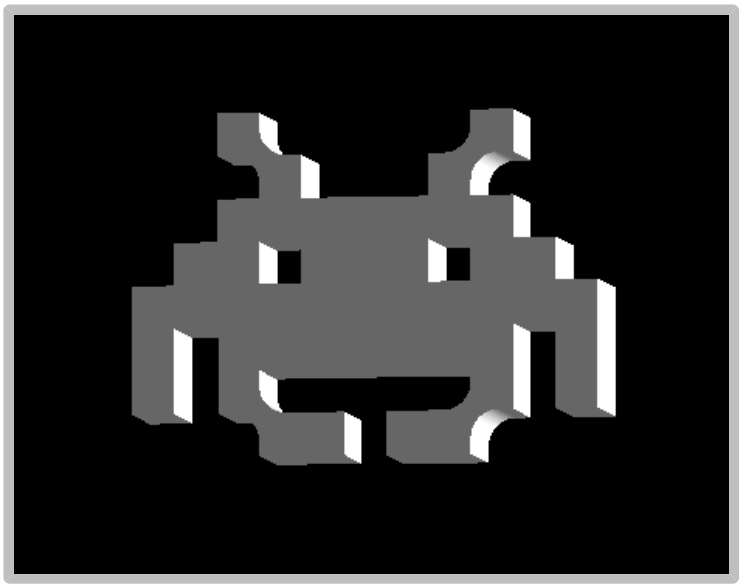

FIGURE 3.1. Imported GDML model of a complex object into Geant4.

3.3 CAD API Plug-In

Although CAD programs allow for manual drawing of parts, the sheer number of perforations in the coded apertures used here make this infeasible. For the $p53$ example aperture of figure 2.13(a) of roughly 5,500 perforations which would need to be drawn. Furthermore, in order to make the aperture free standing, the corners would need to be rounded, adding extra steps to the CAD modelling of a single perforation.

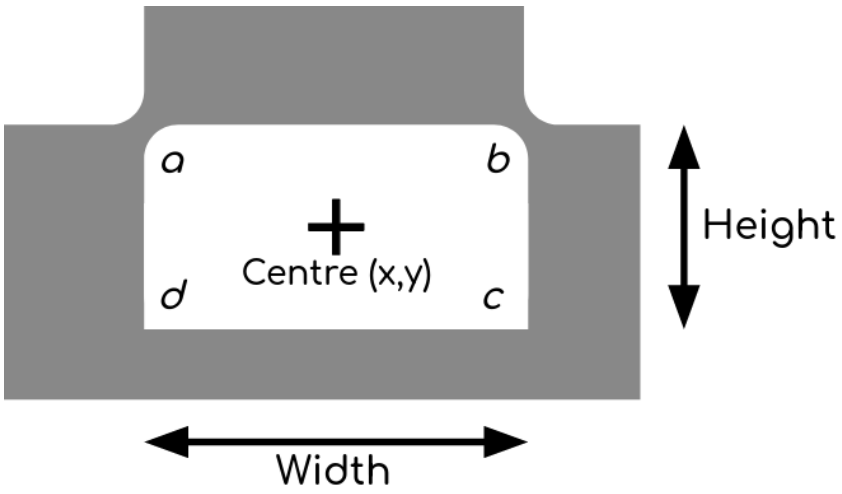

Figure 3.2: The categorisation of a perforation in the CAD API plug-in, where corners a, b, c and d are binary, with a value of 1 for a rounded corner and 0 otherwise.

Thus it can be seen that a programmatic approach is desirable to generate the CAD drawings. For ease of implementation, all perforations are defined as rectangles with a centre point (in x, y Cartesian coordinates) with a width and height. The list of perforations are then tested against one another, to test if corner rounding is required to keep the substrate as one solid self-supporting piece. This is assigned a rounding value to denote which corner(s) require rounding:

$$\text{rounding value} = 1 + 2^0 a + 2^1 b + 2^2 c + 2^3 d \tag{3.3}$$

giving every perforation a value between 1 and 32, and substrate a value of 0, with the assignment shown in figure 3.3. The CAD software used was Fusion360, and the plug-in written is in the appendix. Using this, and input values for any p, substrate thickness, aperture pixel size, and corner roundedness any MURA can be constructed. It is worth noting that the process is memory intensive, and for large p values more RAM may be required, or the use of a different (probably non-free) CAD software. Using a custom-build gaming PC with 16 GB of RAM, a dedicated 1050Ti graphics card and AMD AM4 processor, the Fusion360 software would slow to a crawl for $p > 61$, and for a $p97$ would succeed roughly 40% of the time, with the other 60% requiring a forced restart of the machine.

CHAPTER 4

CODED APERTURES WITH SCATTER AND PARTIAL ATTENUATION

Sub-millimetre radiation sources are ubiquitous in laser-plasma physics, from the small x-ray sources produced for imaging[140], to understanding fusion targets[141–143] or astrophysical analogues[144] including those which aim to study pure electron-positron plasmas[14]. Some such sources will also produce other forms of high-energy radiation - for instance the 14.1 MeV neutrons from DT fusion reactions. In addition, laser-based sources have the potential to impact medical or industrial imaging by increasing the photon energy accessible while potentially reducing the source size. This research into novel sources increases the urgency to find a method for imaging highly penetrating (> 100 keV), small (*ca.* 10 µm) sources to aid development and optimisation.

LWFA has demonstrated the ability to produce micron-sized, MeV-to-GeV electron beams over millimetre scales[29,39–41]. In addition, laser-plasma interactions have recently demonstrated the ability to produce intense beams of positrons[13,14,145]. In order to optimise x-ray sources from LWFA, or measure the spatial extent and charge of a positron population, improvements in the imaging of ~511 keV radiation sources would be advantageous.

4.1 Aperture Imaging

Simple to implement, pinhole cameras provide one such solution, but are limited when in low signal or high energy applications, due to the small pinhole size and attenuation requirement respectively. Since the resolution of the imaging system is dependent on the size of the pinhole, there is an inherent trade-off between imaging resolution and signal strength. In order to optimise a novel laser-based x-ray source (which may fluctuate from shot-to-shot), high resolution in a single shot is desirable. In addition, since the pinhole comprises only a small fraction of the substrate plane, the material used to form the pinhole must provide almost complete attenuation,

requiring a thick substrate. Current micro-machining methods are limited to a hole aspect ratio of *ca.* 50[146] so again the resolution must be compromised for signal to noise ratio (SNR).

In response to these limitations, multi-pinhole systems have been employed, either in the form of a grand array[147,148], or a coded aperture[149]. These are systems with differing methodologies; the former generates multiple images which can be added to compensate for low signal levels or can provide spectral information through differential filtering[129], whereas the latter superimposes the image from each pinhole, which is then decoded in a post-processing step. The specifics of coded apertures are discussed more in section 4.2, but they have have been implemented in a variety of ways, including time modulated apertures[150], spherical apertures for 3D reconstruction[115] and for imaging scattered x-rays in a medical context[151].

Both pinhole arrays and conventional coded apertures still require that the pinhole substrate be highly attenuating to achieve an acceptable SNR. Coded apertures are typically favoured for low-signal environments due to the larger number of perforations possible whilst using standard detectors. However, this is at the detriment of SNR, which is not present a grand array.

Where a static, passive aperture is used, coded apertures have been demonstrated to work for 0.06–1.3 MeV x-rays, requiring aperture perforation diameters of 1.3–2.2 mm[152]. Here, we demonstrate that the resolution limit may be extended by orders of magnitude, since the decoding process is able to discard the background arising from imperfect attenuation. This is quantified through ray tracing calculations which consider the aperture to be either scattering or only partially attenuating, allowing the impact of each effect on imaging capability to be studied independently. We then illustrate the effectiveness of a more realistic aperture - which will exhibit both effects - through Geant4 simulations of a point source. The theoretical imaging improvement expected using a coded aperture with scatter and partial attenuation (CASPA) is compared to a pinhole of equivalent resolution and substrate thickness.

4.2 Coded Apertures & CASPAs

A coded aperture is an array of κ pinholes - henceforth called perforations - in a specific arrangement, with each casting an image of the source onto the detector. The resultant signal from the overlaid images is dubbed the hologram[116]. This hologram can then be decoded through a cross correlation against the decoding function (created from the known aperture design) to form a likeness of the original source[112,119,153].

In contrast to single pinholes, coded apertures do not have any inherent compromise between resolution and signal intensity. The signal may be increased by having a larger number of small perforations, since the resolution is still dictated by the perforation size, where as the signal strength is improved by a factor of κ. Usefully, another advantage of coded apertures is that the decoding process is uniform-background subtracting. The decoding functions are designed such that their cross correlation with an array of uniform magnitude is zero[154]. Thus, particles

incident on the coded aperture need not be fully attenuated, as conventionally assumed, but merely scattered uniformly across the detector surface.

CASPAs utilize this property to propose apertures with better resolution than previously attainable when imaging high-energy x-rays (> 100 keV). When the transmitted photons from the substrate (green in figure 4.1) creates a quasi-uniform background, and their intensity is lower than that of the signal (white), the source can still be reconstructed without the need for full attenuation. This increases the potential scope of use for CASPAs beyond that of pinhole arrays, as the latter does not contain a decoding method and thus is unable to compensate for partially attenuating substrates in a manner similar to the single pinhole case discussed in section 4.5.

Many coded aperture designs exist[4], each sharing similar properties: reduction of inherent noise achieved through uniform perforation distribution without translational symmetry, and maximization of the number of pinholes on the design[119]. For the purposes of this study, the modified uniformly redundant array (MURA) of Gottesman and Fenimore[112] is chosen as the CASPA. These are a family of coded apertures, where each design is designated by its individual prime number basis, p. MURA the properties and construction have been discussed in section 2.4.5.

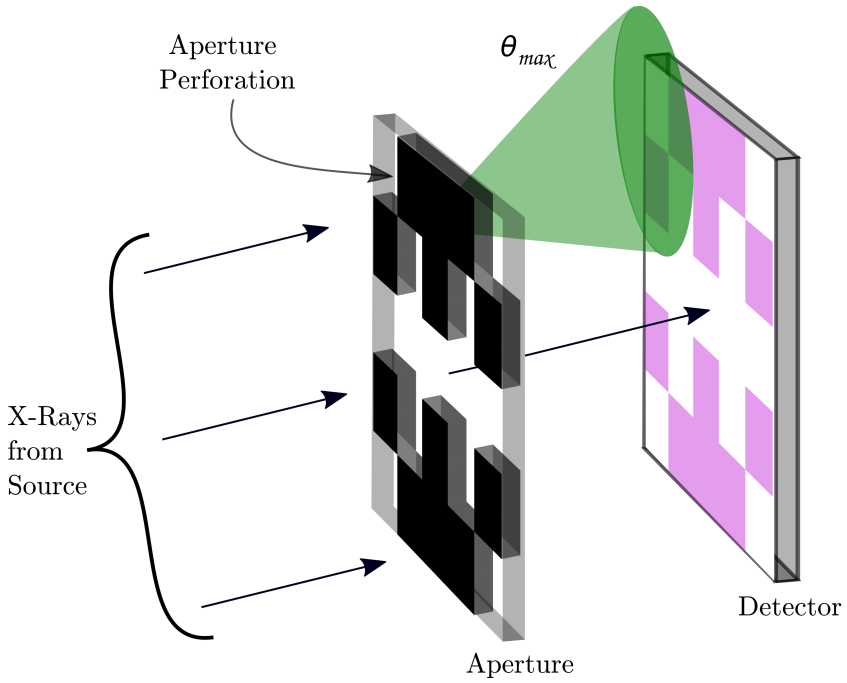

FIGURE 4.1. CASPA system, using a $p5$ MURA. X-rays either: pass through perforations and hit the detector unperturbed; strike the substrate (black) and are absorbed; or strike the substrate and scatter between some angle between 0 and $\theta_{\max}$ (green). The CASPA is designed such that the hologram background (pink) is quasi-uniform, and there is adequate contrast for decoding between said background and the expected signal (white).

4.2.1 Hologram Background

As discussed in chapter 2, the decoding of a hologram is a cross correlation with some decoding function, G - which in turn is a function of the aperture design, A. G is designed such that the expectation value of the array is 1, and the cross correlation of G with a flat background will stay as a flat array.

This cross correlation can be seen as a rastered *likeness* search across the hologram, searching for encoded information by the aperture design. Using this analogy, if the hologram is only flat background then the likeness search will find no correlation with A, and the result will also be flat. Thus, if the CASPA attenuates and scatters to form a uniform background, it will not affect the ability for G to reconstruct the source.

It is noted that having a flat background is not the only solution to background removal, merely the optimal. If a different structured background exists - either through the CASPA, or from other sources within the experiment - it will contribute minimally to the reconstruction under the assumption that is has no correlation with A, and therefore holds no encoded information. Non-uniform backgrounds are likely to add high frequency noise to the reconstruction, akin to the PSF of figure 2.9. However, the hologram requires adequate contrast between signal and background from all sources (CASPA, other scattering sources, and other emitters) in order to reconstruct the source of interest. Therefore, if there is higher background from non-CASPA origins, the CASPA will have to be thicker in order to compensate the other backgrounds through more attenuation and scatter.

4.3 Ray-Tracing Model

A ray tracing model (RTM) has been used to generate synthetic holograms as follows: A ray, represented by unit-vector $\vec{r}$, is generated in a random direction from the source to the aperture. The distance between the between source and aperture in the direction of $\vec{r}$ is given by τ:

$$\tau = \frac{(\vec{P}_a - \vec{P}_s) \cdot \vec{n}}{\vec{r} \cdot \vec{n}} \tag{4.1}$$

where $\vec{P}_a$ is the position of the centre of the aperture, $\vec{P}_s$ is the position of the source, and $\vec{n}$ is the vector normal to the plane of the aperture. The impact point of $\vec{r}$ on the aperture, $\vec{P}_i$ is:

$$\vec{P}_i = \vec{P}_s + \tau\ \vec{r} \tag{4.2}$$

If $\vec{P}_i$ is within the given aperture dimensions, it is compared against the aperture to test if the impact is at a perforation site, of size A_{pix}. Then, the rays are:

1. absorbed and removed from the simulation;
2. scattered by angle θ;
3. incident on a perforation and unaffected.

The likelihood of absorption and the maximum scattering angle, $\theta_{\max}$, may be varied in the simulation. The variables from equations 4.1 and 4.2 are depicted in figure 4.2.

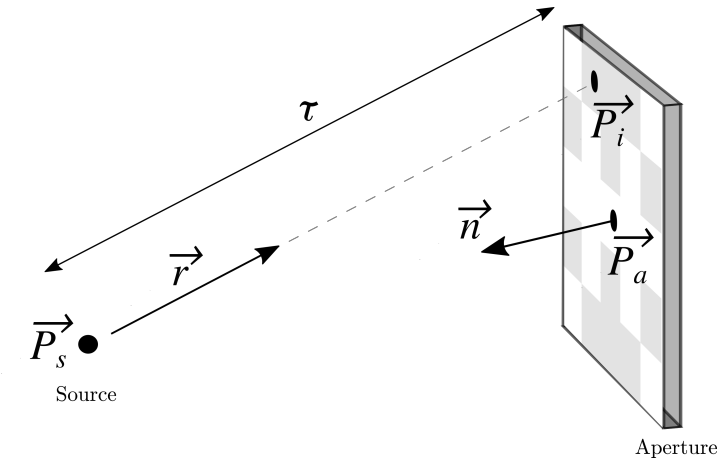

FIGURE 4.2. The depiction of equations 4.1 and 4.2, showing the ray tracing method for ascertaining where on the aperture a ray from the source will be incident. The aperture design has been greyed out to highlight the incident points.

4.3.1 Perturbing Vector

The scattering vector $\delta\vec{r}$ along axis $\langle 0,0,1\rangle$ is given by:

$$\begin{aligned}\delta\vec{r}_x &= \cos\ \phi\sqrt{1-\delta\vec{r}_z^2}\\ \delta\vec{r}_y &= \sin\ \phi\sqrt{1-\delta\vec{r}_z^2}\\ \delta\vec{r}_z &= R(1-\cos\ \theta_{\max})+\cos\ \theta_{\max}\end{aligned} \tag{4.3}$$

where R,ϕ and θ are uniformly distributed random numbers within the ranges: $0 \le R \le 1$ and $0 \le \phi < 2\pi$. For the unique case of $\vec{r} = (0,0,1)$, the perturbed unit vector, $\vec{r}_{\text{pert}}$ equals the normalised scatter vector, $\delta\hat{\vec{r}}$.

For all other vectors, $\delta\hat{\vec{r}}$ must be rotated such that its axis lies along $\vec{r}$, instead of $\langle 0,0,1\rangle$. This is achieved through a rotational matrix, $\aleph$, about rotational axis, $\vec{s}$, subtended through angle α[155]:

$$\vec{s} = \langle 0,0,1\rangle \times \vec{r} \tag{4.4}$$

$$\alpha = \arccos(\ \langle 0,0,1\rangle \cdot \vec{r}\ ) \tag{4.5}$$

$$\mathbb{M} = \begin{bmatrix} \cos\alpha + \vec{s}_x^2(1-\cos\alpha) & \vec{s}_x\vec{s}_y(1-\cos\alpha) - \vec{s}_z\sin\alpha & \vec{s}_x\vec{s}_z(1-\cos\alpha) + \vec{s}_y\sin\alpha \\ \vec{s}_x\vec{s}_y(1-\cos\alpha) + \vec{s}_z\sin\alpha & \cos(\alpha) + \vec{s}_y^2(1-\cos\alpha) & \vec{s}_y\vec{s}_z(1-\cos\alpha) - \vec{s}_x\sin\alpha \\ \vec{s}_x\vec{s}_z(1-\cos\alpha) - \vec{s}_y\sin\alpha & \vec{s}_y\vec{s}_z(1-\cos\alpha) + \vec{s}_x\sin\alpha & \cos(\alpha) + \vec{s}_z^2(1-\cos\alpha) \end{bmatrix} \tag{4.6}$$

In the general case, the perturbed vector is defined as:

$$\vec{r}_{\text{pert}} = \mathbb{M} \cdot \delta\vec{r} \tag{4.7}$$

Equations 4.1 and 4.2 are re-applied to all the scatter and perforation site rays, using the position of the detector, $\vec{P}_d$ instead of $\vec{P}_a$, to find the new $\vec{P}_i$ in the detector plane. A hologram is then constructed from a histogram of the detector plane.

Once decoded, the image is evaluated by calculating the SNR from the known position of the sources in the source plane:

$$\text{SNR}_j = \frac{\lambda_j - \mu_{\bar{j}}}{\sigma_{\bar{j}}} \tag{4.8}$$

where j is the set of expected positions, λ_j is the sum of signal strength over all j and $\mu_{\bar{j}}$ and $\sigma_{\bar{j}}$ are the mean and standard deviation of all pixels not in set j, respectively. All pixels not in set j are henceforth called the background.

4.3.2 Random Number Generation

The RTM is a pseudo-Monte Carlo simulation, using a large volume of rays to statistically create a hologram. As such, there is a necessity for random numbers to build up this statistical profile. However, computationally generating truly random is not trivial. Mathematically based generators are capable of getting stuck repeating short sequences or continually perpetuation of a zero value[156]. Furthermore, attempting to generate a random number by selecting a random mathematical process from a list of functions lead to unpredictable cyclic periods[156]. For the purposes of a Monte-Carlo simulation, the random number generator (RNG) need not be truly random, or even cryptographically random[†] , but a pseudo-random number generator (PRNG) will suffice. That is, a RNG that is statistically random, but each value is sequential based on its predecessors.

[†]a random number generator where past and future values can be predicted from analysing a small sub-set of values

Per ray traced, the PRNG will be called between 3 and 6 times:

- 2, for $\vec{r}_x$ and $\vec{r}_y$;
- 1, for determining if the particular ray is attenuated;
- If it is not attenuated, then 1 for determining if it is scattered;
- If it is scattered, then 2 for ϕ and $\delta\vec{r}_z$ of equation 4.3.

As such, the number of calls to the PRNG function is linearly dependant on simulation flux. With fluxes of the order of 10^8 and above being simulated, it is desirable for a thread-safe generator to allow for multi-threading to be utilised. Furthermore, with so many function calls, the period of the PRNG must not be significantly less than the flux.

C & C++ have their own in-build PRNGs, but neither have been used for the RTM due to their unknown properties. The classic C function `rand()` uses global variables, making it problematic for use with multi-threading. Both `rand()` and C++'s updated equivalent, `<random>`, have a period equal to the arbitrary integer `RAND_MAX`. This variable is defined by the compiler and computing hardware used, and can be as low as $2^{15}-1$ (*ca.* 3×10^4). Furthermore, the nature of intrinsic functions to coding languages is that, although they are open source, the source code is rarely easily accessible or scrutinised by people besides the developers.

For the reasons stated above, a hard-coded PRNG has been implemented called an exclusive-or shift (XORshf), that utilised bitwise operations instead of mathematical[157]. The XORshf is statistically random, as shown by the Diehard Battery of Tests[158]. The PRNG's maximum value is `uint64_t`, which is a constant value across all compilers.

An exclusive-or logical operator, $\wedge$, is a bitwise comparison between two bit strings, which will be conceptualised as string $\Bbbk$ and $\dagger$. It compares each bit of the same index, `[i]`, in both strings; if only 1 of $\Bbbk$`[i]` and $\dagger$`[i]` is a 1, then the result is a 1. For every other possibility, a 0 is returned[159]. For an example case where $\Bbbk$ is $[1,0,0,1]$ and $\dagger$ is $[1,1,0,0]$:

$$\begin{array}{rr} & 1\,0\,0\,1 \\ \wedge & 1\,1\,0\,0 \\ \hline & 0\,1\,0\,1 \end{array}$$

Bit shifting simply moves all of the bits along the string in the speficied direction and number of bits. Any bits shifted outside the length of the string, and any newly introduced bits are given a value of 0. This can be either to the left, <<, or right, >>, with sequential moves in either direction used to ensure both ends of the bit string are all 0 values. XORshf utilises both of these techniques, and the specific order depends on the generator used. Here, the XORshf128 is implemented, which has a period of $2^{128}-1$ (*ca.* 3×10^{38})[157].

The implemented XORshf128 works thus[157]:

$$\begin{aligned} \text{X}' &= \text{X} << 11 \\ \text{X}'' &= \text{X}' >> 8 \\ \text{Y}' &= \text{Y} >> 19 \\ \text{RAND} &= (\text{X}'' \wedge \text{Y}) \wedge \text{Y}' \end{aligned} \tag{4.9}$$

where B is initialised as the previous RAND value, and X is initialised as the previous Y value.

The XORshf128 needs to be seeded, as with all PRNG's. For testing purposes, this can be set to a constant. For simulation, the seed is a function of the date, time, and thread ID, to help keep the code thread-safe without repeating rays.

4.4 Experimental Considerations

In this design study, a $p53$ MURA is used, which has 5512 perforations. 6×10^7 photons are randomly fired at the aperture from the point source and collected on a detector of idealised dimensions, as depicted in figure 4.3. The system has a magnification of 1[154,160], and no addition of external noise or background. The idealised detector size, D_{det} is given by:

$$D_{\text{det}} = \frac{Mp}{R} \tag{4.10}$$

where M is the magnification of the system and R is the desired number of resolvable features per unit length, henceforth called resolution capability. The pixel size of the idealised detector is given by:

$$D_{\text{pix}} = \frac{M}{nR} \tag{4.11}$$

where n is any positive integer, and the aperture pixel size is given by:

$$A_{\text{pix}} = \frac{1}{R(M^{-1}+1)} \tag{4.12}$$

For this study the detector is 106×106 pixels, $R = 0.5$ pixel^{-1}, $M = 1$ and $n = 2$, resulting in aperture and detector pixels being the same size. The imaging system field-of-view will be proportional to the size of the aperture p value and the desired resolution capability. As such, for any other given experiment a detector can be chosen to fit the spatial and spectral requirements.

While this work does not aim to resolve the challenges in selecting an appropriate detector, it is clear that MeV-photon or neutron detection with sub-100 µm resolution is not possible with high efficiency. Mikerov *et al.*[161] suggest that neutron detector resolution could be better than 100 µm. With modest magnification built in to system, the increased throughput of a CASPA could be beneficial for imaging the symmetry of DT-fusion reactions in inertial confinement fusion

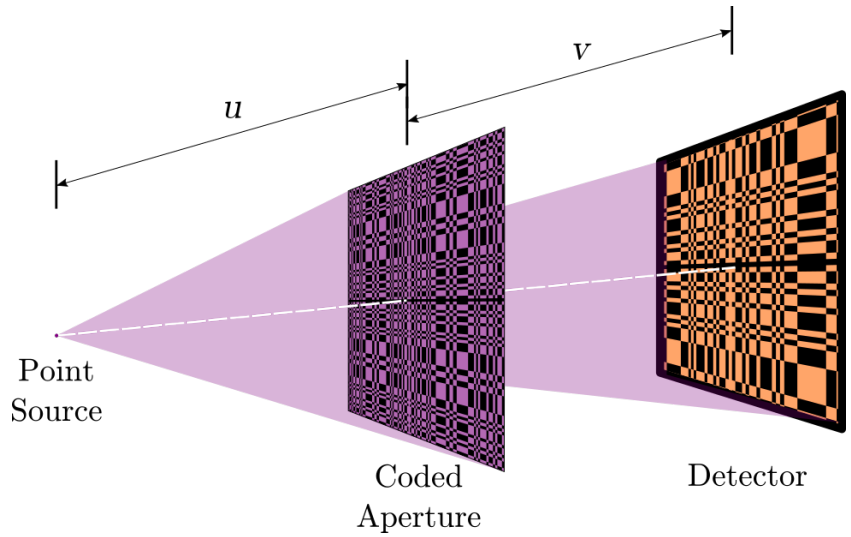

FIGURE 4.3. A diagram of the CASPA imaging system used in this study, using a RTM generated hologram on the detector. The aperture is a $p53$ MURA, and $u = v = 1060A_{\text{pix}}$.

experiments, as discussed in chapter 6. For a resolution of 0.1 μm^{-1} as indicated in this work we would require a detection area in excess of 0.5×0.5 mm, and a pixel size of ≤10 µm. At photon energies < 30 keV, this can be readily achieved with commercially available sCMOS detectors, whilst the 30–100 keV range can be achieved with CdTe detectors[162] or Medipix and Timepix detectors[163]. Detectors in the 200+ keV range are under development, such as a CsI array[164], and the progress of other such high-energy, high-resolution detectors will be concurrent with development in compact laser-plasma x-ray sources and fusion neutron detectors. CASPAs are not reliant on such development, and can be used with current detectors and system magnification to achieve the desired resolution capability.

4.5 CASPA - Pinhole Comparison

We now compare a CASPA to a standard pinhole, as a function of the substrate properties using SNR (equation 4.8) as the figure of merit. SNR values are not absolute, and will scale with number of particles (either photon or neutron) within the simulation. Convergence testing could be applied to find the maximum SNR and negate the dependency on number of particles. However, this would only elongate simulation run-time, as the relative trends between attenuation, scatter, and SNR is the subject of interest. Absolute values would not be consistent for all systems, and further work would be required to design a CASPA for a given source and experiment. For the initial comparison, it is assumed that aperture attenuation and maximum scattering angle can be varied independently. While these properties will be correlated and dependent on the physical attributes of the aperture, it is useful to consider their effects on image quality independently.

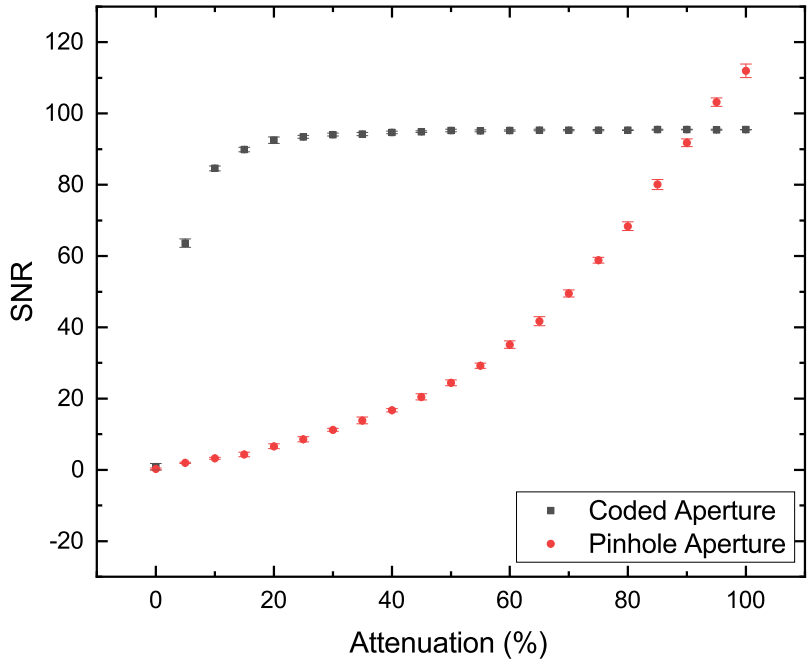

FIGURE 4.4. Variation in SNR for coded and pinhole apertures as a function of aperture attenuation only. Errors from the standard deviation of 6 simulations.

The detrimental effect of incomplete attenuation on a pinhole aperture can be seen in figure 4.4. It follows the expected trend, due to the lack of inherent background-subtraction. In contrast, the SNR of the coded aperture remains within 5% of its maximum at only 15% attenuation. It should be noted that, since the decoding is conducted in Fourier space with finite planes, the coded aperture always exhibits noise even at 100% attenuation and so underperforms the pinhole in this case.

From figure 4.5, it is clear that scattering through the aperture is of limited value to imaging with a pinhole. The increase in SNR here is, in small part, due to scattered particles missing the detector. The more significant effect is that the scattered rays are being distributed over a larger area. In the case of the coded aperture, this quasi-uniform background will be removed during decoding, resulting in a near-zero $\mu_{\bar{j}}$. However, in the case of the pinhole the quasi-uniform background remains, increasing $\mu_{\bar{j}}$ and thus reducing the SNR of the pinhole. This effect has reduced the SNR maximum of the pinhole by 83%, compared with the maximum seen in figure 4.4.

Individually, figures 4.4 and 4.5 show that SNR of a CASPA has not degraded by more than 5% when the substrate has a minimum attenuation of 15% or a minimum θ_{max} of 20^o . The two mechanisms can be combined to produce a CASPA with lower values of each, whilst still keeping sufficient SNR to allow imaging. The results of a two dimensional study (figure 4.6) demonstrate this additive effect.

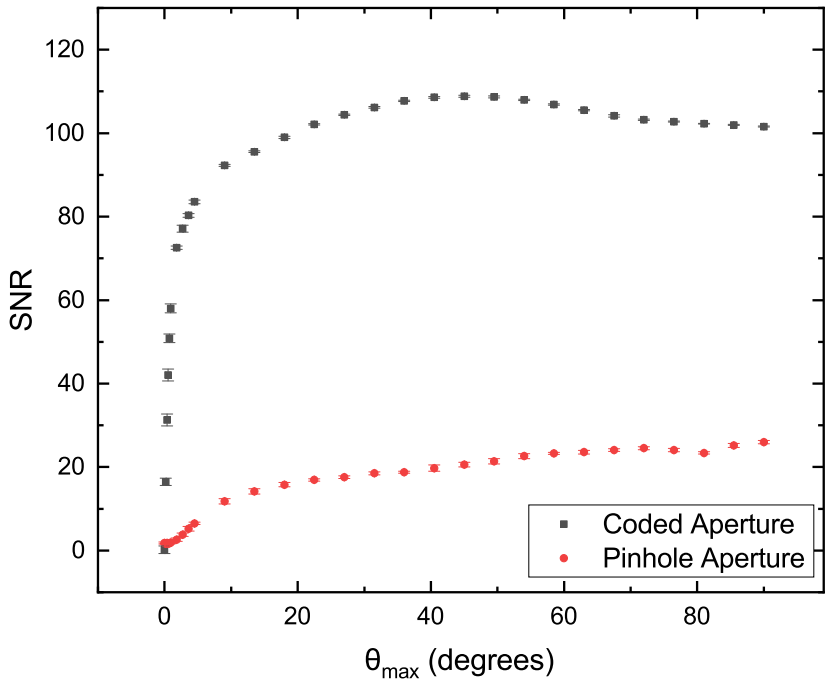

FIGURE 4.5. Variation in SNR for coded and pinhole apertures as a function of $\theta_{\max}$. Zero attenuation is assumed. Errors from the standard deviation of 6 simulations.

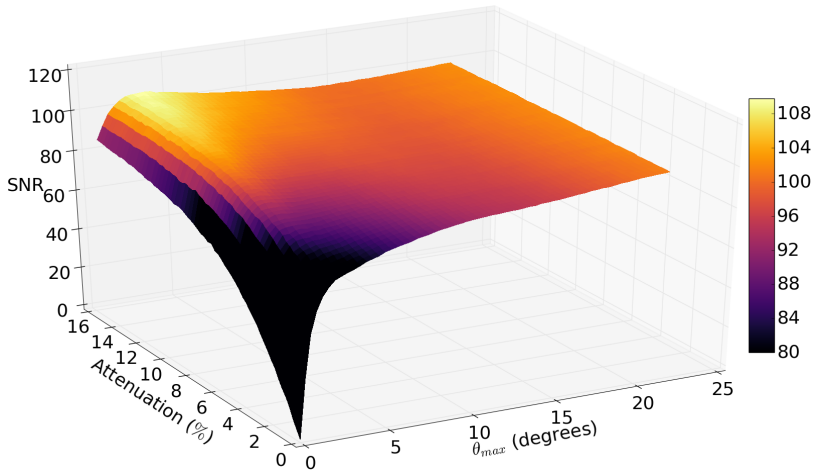

FIGURE 4.6. Surface plot of SNR as a function of both attenuation and $\theta_{\max}$.

4.6 Benchmarking RTM with Geant4

Although the RTM is useful in demonstrating the independent effects of scattering and attenuation on imaging efficacy, it does not reflect the reality that both will increase as the aperture thickness is increased. For this, a Monte Carlo simulation package is required. 511 keV photons are used, to coincide with gamma rays used in PET imaging[165] and the CASPA and source are

modelled using Geant4[138].

To benchmark the RTM, the same design and geometry is modelled in Geant4. A 250 µm thick tungsten substrate was used, calculated to be the equivalent to 6.30% attenuation at 511 keV from mass coefficients[166], with an A_{pix} of 50 µm, and thus an aspect ratio of 5.

It was found that, above an aspect ratio of 5-10, the effective field of view for many of the non-central CASPA perforations did not include the point source being imaged. This in an inherent issue with using MURAs, as they were originally designed for far-field imaging, instead of the near-field application being demonstrated here. To generate a 4π scattering source, a positron beam of 2^{32-1} particles was directed onto a 200 µm tungsten target, resulting in 1.34×10^{6} photon events on the detector.

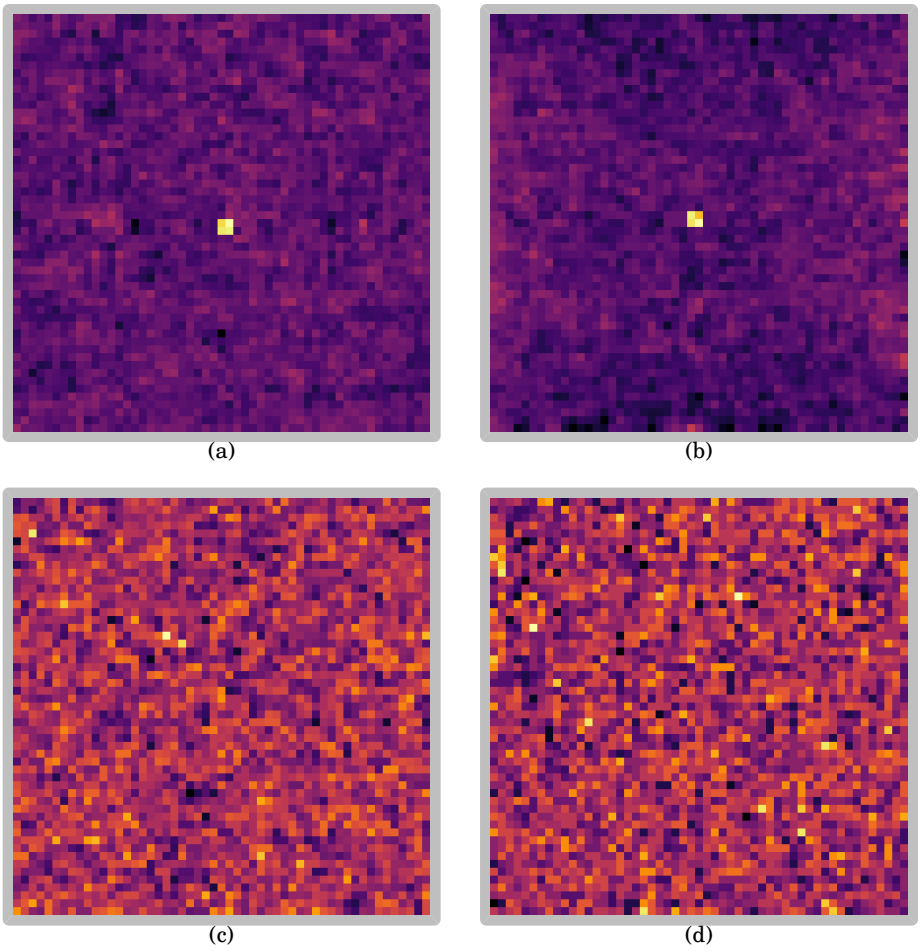

FIGURE 4.7. A comparison between the RTM, (a) & (c), and Geant4, (b) & (d), methods for holgram simulation. (a) & (b) use a CASPA, whilst (c) & (d) are pinholes. (a) – (d) all have the same substrate thickness and A_{pix}. The scales are independent of one another, ranging from the local minima to maxima, with the CASPAs being the expected *ca.* 2 orders of magnitude greater than the pinholes

A separate Geant4 simulation was used to determine $\theta_{\max}$, in order to create a comparable environment for the RTM. $1{\times}10^8$ 511 keV photons were fired into a 250 µm tungsten plate, and the FWHM of their impact upon the detector calculated. This resulted in a $\theta_{\max}$ of $1.3{\pm}0.2$ degrees. It was also quantified that only 0.8% of the non-attenuated ray were scattered by the substrate, which was then incorporated into the RTM. $5.33{\times}10^6$ photons were used, in resulting in a comparable $(1.33 \pm 0.01){\times}10^6$ detector events.

The decoded images of the RTM and Geant4 can be seen in figure 4.7, with SNR values of 47 ± 3 and 43, respectively. The variation is likely due to the discrepancy in source size; the RTM source is an infinitesimally small point in space, whilst Geant4 source size is $¼A_{\text{pix}}$, due to the intrinsic requirement for finite dimensions. The reduced SNR is due to the diminished number of photons impacting the detector with respect to section 4.5. However, the added complexity of the Geant4 toolkit makes higher Geant4 fluxes impractical due to the simulation run-time.

Despite the slight variation in SNR, figure 4.7 is able to show that the two hologram generation techniques are comparable. The RTM run-time is orders of magnitude smaller than its Geant4 counterpart, being of the order of 10 seconds versus 10 hours, and as such the RTM is preferred for simulating higher flux systems.

4.7 Extended Source

Generating a hologram for an extended source requires an increase in number of particles used, to prevent a significant drop in intensity per unit area in the source plane, or *source plane* now an extended shape is being imaged. As RTM holograms were shown to be comparable to Geant4, RTM is used for the extended source, due to its greater speed.

Continuing with the example of a tungsten aperture to image 511 keV photons, a substrate thickness of 18 mm would be required for 99% attenuation. For an aspect ratio of 5, the perforation size of a fully attenuating system would be 3.6 mm, and the maximum resolution would be 7 mm. - although it is noted there would be field of view challenges with such a thick aperture that have not been considered here. This is in contrast to the 250 µm CASPA, which for the same aspect ratio of 5 would have feature sizes of 50 µm and a resolution limit of 100 µm. This equates to a ×70 increase in resolution capability in this demonstration. Moreover, the CASPA (figure 4.8(a)) is able to reconstruct an image in the high-energy low-signal environment that an equivalent pinhole (figure 4.8(b)) could not.

We propose that extending the aperture-detector distance could further decrease the aperture thickness required for effective imaging. Scatter within a CASPA enables a high SNR by distributing the photons upon a large detector area, creating a quasi-uniform background. By conserving the detector area over which photons are scattered, it can be shown geometrically that $\theta_{\max}$ and the aperture-detector distance are inversely proportional. As propagation distance has not been investigated here, its effects can instead be qualitatively discussed through an increase

in θ_{max}. An increase in θ_{max} has been shown by figure 4.6 to require less aperture attenuation, and therefore can produce a better imaging resolution; this is before considering the conventional resolution improvement from system magnification.

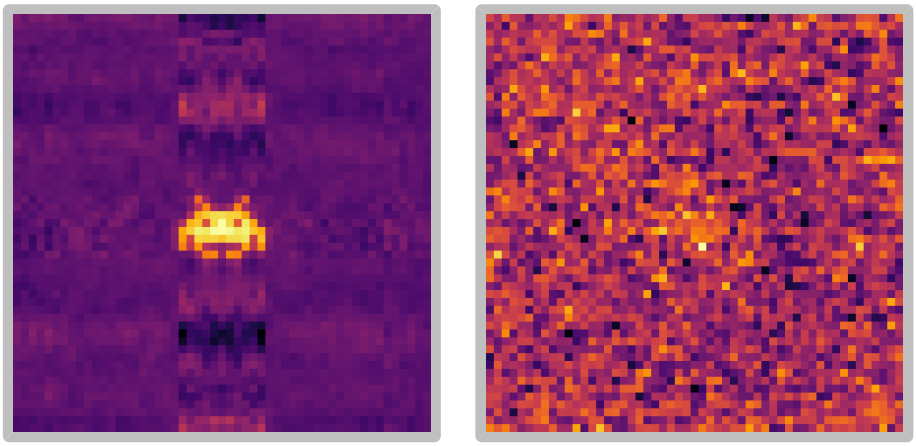

(a) (b)

FIGURE 4.8. RTM generated results for a CASPA (a), and an equivalent pinhole (b) for an extended source. 1×10^8 photons per source unit area, resulting in a total flux of 4.6×10^9 511 keV photons.

4.8 Improved Decoding

Figure 4.8 demonstrates that the CASPA is able to reconstruct a source that an equivalent pinhole cannot, despite being of identical substrate material, thickness, and aperture size. However, some aliasing can be seen, with source-like iterations most notable in the positive and negative i direction. This is not solely an artefact of the CASPA, and is present in coded aperture decodes with 100% attenuation and $\theta_{max} = 0$, as shown in figure 4.9. It can therefore be surmised that the aliasing seen is a bi-product of the decoding method of equation 2.14.

The effects of aliasing on the decoding accuracy can be seen within the PSF graphs shown in figure 4.10. Although the graphs are for different p value arrays, and different flux simulations, it can be seen that the delta spike shown in Fenimore[119] has not been obtained within the SPSF for this work. Instead, the aliasing appears as noise across the background, quasi-symmetrical about the central spike.

As previously stated, when oversampling (see figure 2.5) the ideal detector size is designed to project the central aperture pattern onto the entirety of the detector. Moreover, G is scaled up to incorporate magnification into the decoding process, as the original apertures were only used for systems assuming the incident photons were collimated, typically from far-off star systems[112,119]. This scaling leaves the array size of G and the idealised size of D to be the same.

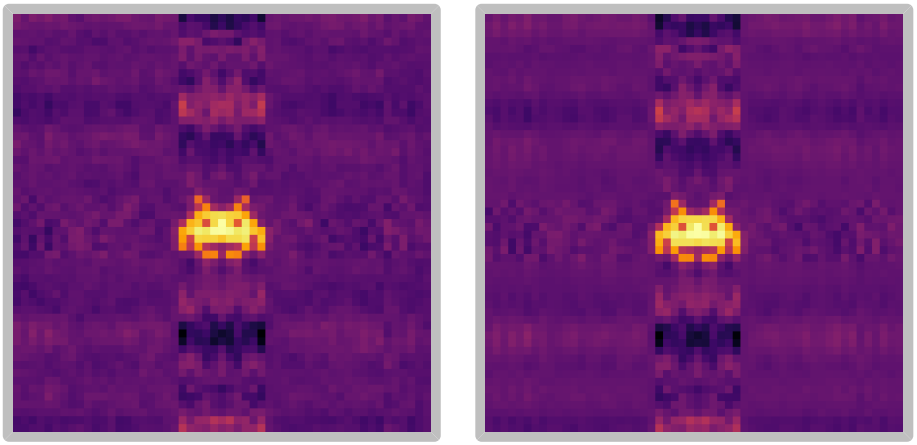

(a) (b)

FIGURE 4.9. A comparison of (a) the CASPA image from figure 4.8(a) against (b) a coded aperture image with 100% attenuation and no scatter in the substrate.

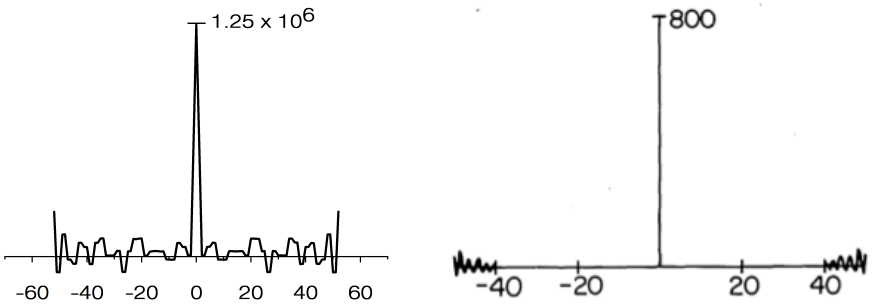

(a) (b)

FIGURE 4.10. The PSF of a fully attenuating coded aperture image of a point source, taken from a line-out in the x direction. (a) is a $p53$ MURA hologram created with the RTM, and (b) is a δ function from a $p40$ URA by Fenimore[119], as shown in figure 2.12.

In signal processing, the Nyquist criterion states that to prevent aliasing, the sample rate, f_s, must be at least twice that of the bandwidth, B[167]:

$$f_s > 2B \tag{4.13}$$

for the recreation of an analogue signal using a Fourier transform method. For a simplified signal of only 1 frequency component, equation 4.13 states the signal length analysed must be at least twice that of an individual cycle. Conceptualising D as a single, complex signal to be reconstructed into $\hat{S}$, the decoding method does not satisfy the Nyquist criterion as the signal length analysed is only the length of one individual cycle. This explains the aliasing seen in figure 4.9 and the impact it has on the SFSF of figure 4.10.

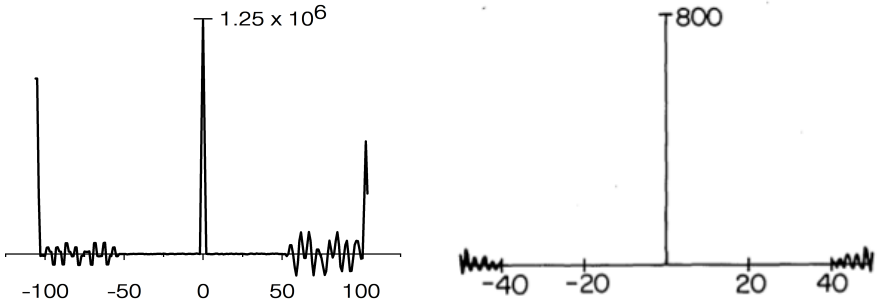

(a) (b)

FIGURE 4.11. A side-by-side comparison of the δ function PSF from the periodic decoding method against that of Fenimore shown previously (figure 2.12[119]). (a) is the same $p53$ aperture and simulated detector as figure 4.10(a).

The Nyquist criterion can be satisfied pre-decoding post-processing, by modelling the detector plane as part of a periodic function. The same mosaic technique can be applied to D as it is in the creation of A, increasing the size of D to $(2D_{\text{det}}-1)\times(2D_{\text{det}}-1)$. This creates a $\hat{S}$ twice as large as required, which is then cropped back to size. Figure 4.11 shows that this has not removed the aliasing from $\hat{S}$, but instead moved it sufficiently far towards the edge of the array that it is removed when cropped. This brings the SPSF results of the periodic method into agreement with Fenimore[119]. It is worth noting that the magnitude of the peak has not changed between figures 4.10(a) & 4.11(a), suggesting there is no information lost between the two decoding methods.

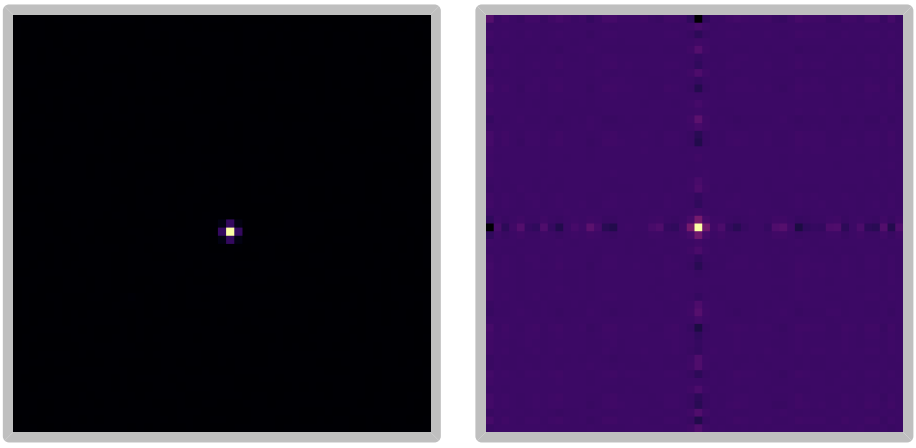

(a) (b)

FIGURE 4.12. A comparison of (a) the periodic decoding method against (b) the previous decoding method for a point source, under identical experimental conditions, and a total flux of 1×10^7. SNR of (a) is 152.2 ± 0.4, (b) is 81.0 ± 0.1, with the peak intensity being $(7.03\pm0.01)\times10^5$ and $(7.033\pm0.007)\times10^5$ respectively.

The decoding improvement can be visualised not only by the PSF, but also by the reconstruction of a point source, as shown in figure 4.12. The Fourier aliasing seen in the cross-hair like configuration has been successfully removed with the periodic decoding method. It is worth noting that there is still some background fluctuation in both images, with figure 4.11(a) not being a true delta function. Thus, for a theoretically perfect system, it cannot achieve the infinite SNR of its pinhole counterpart. However, in the finite simulation of figure 4.4, the periodic decoding methods increased SNR of 152.4 ± 0.4 elevates its performance above that of the pinhole aperture.

The aliasing observed is known to be a function the number of sources present in S[112]. This was never an issue in the original MURA design, as its purpose was imaging < 10 point sources, but for a small-scale laboratory imaging system of an extended source, the accumulative effect of each pixel in S is detrimental to the imaging quality attainable. Previously, these aliasing effects have begun to dominate $\hat{S}$ when S has > 100 pixels of source, which would have reduces the scope of use for coded apertures and CASPA's. Figure 4.13 shows that larger extended sources are possible with the improved decoding. While the threefold SNR increase is desirable, the visual comparison between figures 4.13(a) & 4.13(b) shows the difference in clarity between the two $\hat{S}$, which best demonstrates the necessity of the improved decoding method.

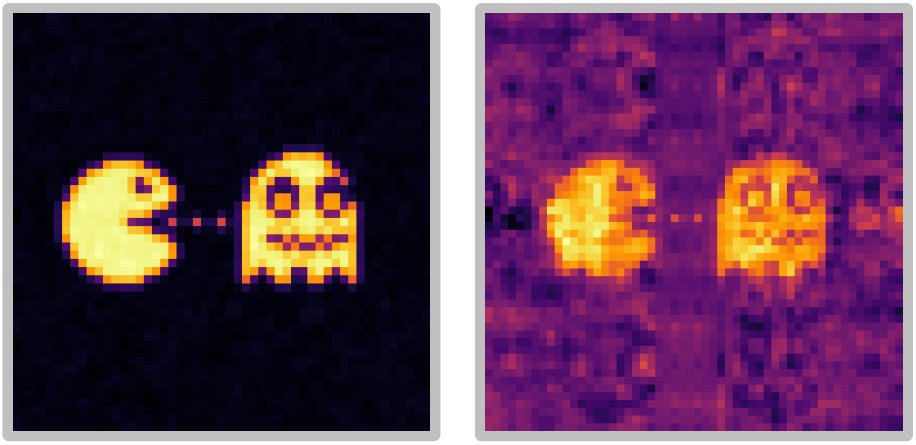

(a) (b)

FIGURE 4.13. A comparison of (a) the periodic decoding method against (b) the previous decoding method for a larger extended source which was previously noise heavy, under identical experimental conditions, and a total flux of 3.11×10^9. SNR of (a) is 6100 ± 30, (b) is 2042 ± 5, with λ_j being $(3.540 \pm 0.003) \times 10^8$ and $(3.340 \pm 0.003) \times 10^8$ respectively.

It is also worth noting that the improved decoding method is not only applicable to 100% attenuating coded apertures. Figure 4.14 shows a comparison between the two decoding methods for the CASPA hologram of figure 4.8 through a 250 µm W aperture. Once again there is nearly a threefold increase in SNR, and the visual comparison shows the aliasing has been removed. There is a low level, random background present, but it is no longer proportional to any aperture

or source properties, and nor is it constant across multiple simulations. This is due to the finite particle number and the randomness of a Monte Carlo system, and is likely to also be observed in laboratory results.

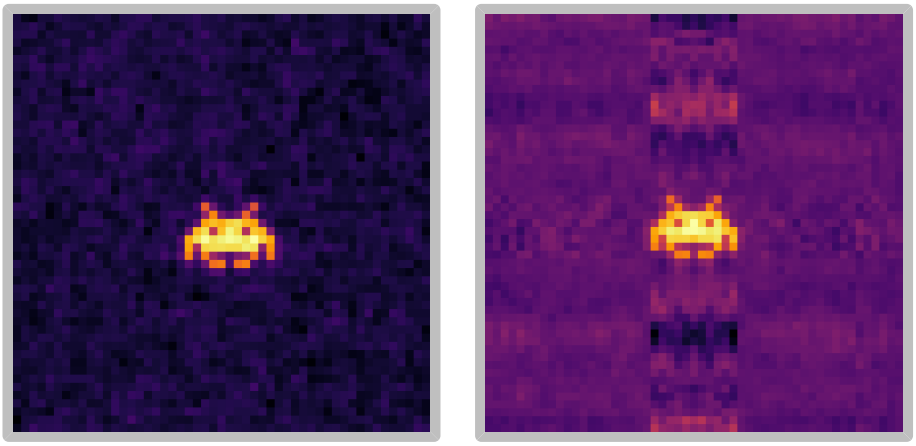

(a) (b)

FIGURE 4.14. A comparison of the improvement in CASPA image quality between (a) the periodic decoding method and (b) the previous decoding method for an extended source, under identical experimental conditions, and a total flux of 4.6×10^9. SNR of (a) is 1426 ± 3, (b) is 598 ± 1, with the λ_j being $(4.716 \pm 0.003) \times 10^7$ and $(4.701 \pm 0.007) \times 10^7$ respectively.

4.9 Conclusion

In summary, we propose that complete attenuation is not required for coded apertures to generate high SNR images. We demonstrate that this benefit is due to the way in which the image from a coded aperture is reconstructed, allowing a flat background to be removed. This means that full-attenuation of the substrate is not required and that scattering the photons or neutrons through the aperture relaxes this requirement further. We also show through benchmarking with Geant4 that, with knowledge of the scattering angle and attenuation of the substrate, coded aperture holograms may be generated quickly from a ray tracing model.

We show a practical example of this by simulating an extended source imaged with 511 keV photons using a 250 µm thick tungsten CASPA. Through this, we demonstrate that high-energy low-flux aperture imaging is feasible, corresponding to a significant improvement in either resolution or flux compared to a fully attenuating pinhole aperture. Given experimental access, or more detailed information about the simulated parameters, this can be applied to electron-positron plasma experiments, such as those by Sarri *et al.* to validate the results suggested therein, and their agreement with the simulations performed[13,14].

CHAPTER 5

BANDED SPECTRAL CODED APERTURES

Spectral information can be useful to infer the plasma temperature during an experiment, when invasive probes will melt and affect plasma conditions. Spectrometers can be used to calculate a temperature via prior assumptions of the source - such as it being a black body emitter. However, many spectrometers will not hold spatial or temporal information, which can be useful in diagnosing plasma characteristics. Some single-detector techniques utilise a two dimensional camera, with one dimension for spectral information and the other for spatial or temporal[19–21]. For the spectral-spatial techniques, assumptions about source symmetry need to be made.

Cameras do exist that are capable of recording 2D spatial and spectral information of a source[168–171]. These operate with each pixel able to read out the deposited energy within them over a given short read-out time. In order to ensure the energy deposited is from a single particle, the camera needs to be filtered such that only one particle hits any one pixel per read-out, otherwise known as single hit detection.

Single hit detection does have its limitations. The amount of filtering required necessitates integration over time to build up a spectral profile, which is not possible on single shot experiments. Due to the hardware required to have energy readouts the pixel sizes are often large, which will reduce the resolution capability of the system. The quauntum efficiency of these cameras can limit their use to low keV ranges[170] up to 100 keV[168]. Finally, the intricacy of such cameras means the cost of purchase is high, pricing some small laboratories out of their use.

Often the complete spectrum is not required to fit the temperature. Instead, it can be inferred from two to three data points - which can be achieved with three distinct spectral bands. Spectrally banded imaging is also useful for high background imaging of different energies, the be able to selectively filter out the desired spectra.

5.1 Ross Pairs

Named after their original author, Perley Ross, Ross pair filters are one such technique for isolating specific energy bands from a broad spectrum[172]. Measurements of the source are taken with two different filters, a and b, and the difference $b - a$ plotted. The materials and thicknesses of a and b are chosen such that their transmission overlaps everywhere besides their K-absorption edges, as shown in figure 5.1.

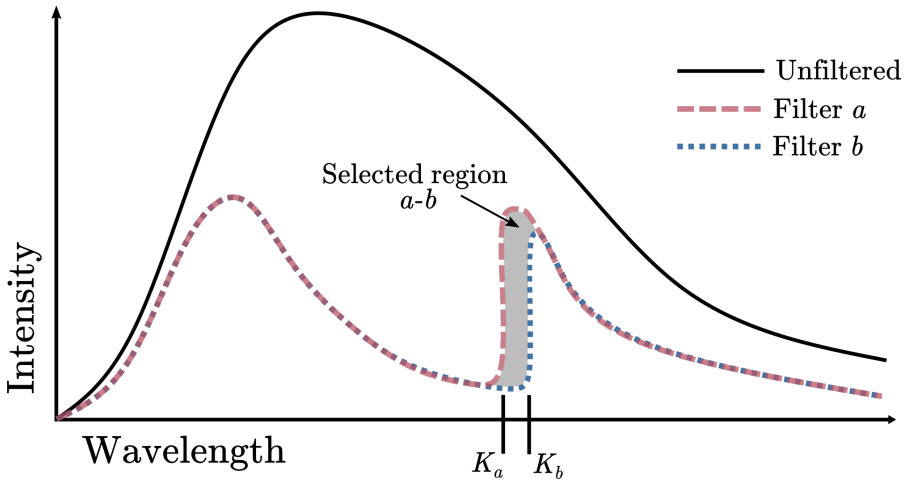

FIGURE 5.1. A sketch showing the transmission spectrum of a broadband source (unfiltered) through filters a and b, where the filter materials and thicknesses have been chosen to create a Ross pair. The grey region is the spectral range being bandpass filtered, between K_a and K_b.

In order to have a narrow energy band, as well as increasing the chance of a and b having transmission overlap everywhere but the K-edge, materials of adjacent atomic number are used[173]. Therefore one limitation of the Ross pair technique is their tunability. The spectral bands produced can only ever be between discrete K-edges, and cannot be adapted to the desired experimental range. Although it is possible to shift the K-edge of a material through doping, shifts of 1–3 eV have been published[174], which are unlikely to make a noticeable difference with metal K-edges all roughly within the keV range (the originally published example of Ag and Cd being 25.5 and 26.7 keV respectively[172]).

Other limitations to Ross pair filters are the maximum energy cap, and the number of pairs available. The K-edge of uranium is 115 keV[175], effectively limiting the range of source energies Ross pairs can be used with to less than *ca.* 100 keV. Furthermore, not all elements are safe, practical, or cost effective to use as a filter, further reducing the list of possible Ross pair filters.

The scope of Ross pair use can be expanded by relaxing the requirement for transmission to overlap everywhere that is not the K-edge. Instead, the residual sensitivity outside the desired band must be significantly lower than within the band (10% tolerance). This allows Ross pairs to

be designed with non-adjacent atomic numbers, for doped or stacked filters instead of elements, and for wideband filters spanning 10–20 keV each[176].

Ross pair filters can be combined with a pinhole to produce selectively spectrally banded imaging - where the substrate is fully attenuating, and the pinhole is made of the filter material. This projects a image of the source onto the detector, with the counts varying as a function of source energy and filter a transmission. A second image is projected through a pinhole of filter b, and the images subtracted from one another to produce an image of the source only within the energy band $K_b \leq E \leq K_a$.

As discussed in chapter 2, single pinhole imaging has limitations for high-resolution, low signal or large sources. Separate images need to be formed for each filtered pinhole, which requires either a large detector or multiple detectors to capture.

5.2 Non-Redundant Arrays

Coded apertures can be utilised to decode overlapping images from a known aperture design, and thus can theoretically be used in conjunction with ross pair filters to create a more spatially efficient spectrally banded imaging system with the benefits of a coded aperture. Multiple aperture designs with different filtering levels - akin to Ross pairs - can be put onto a single substrate. This will create a combined hologram of the multiple filters, which can then be decoded separately, and subtracted, to form spectrally banded images. This will henceforth be called a banded spectral coded aperture (BaSCA).

In order to have multiple designs on a single substrate, the open fraction of any one design cannot exceed $1/2n$, where n is the number of aperture designs. For this reason, a MURA or URA are unsuitable as their $n \approx 0.5$. A random aperture could be used, but the high frequency decoding noise discussed in chapter 2 is why they are not considered here.

5.2.1 Construction

The construction of NRAs is ill-defined in the literature[119,122,177,178], for anyone but theoretical mathematicians. Here, a description of the construction process will be given with enough detail to create an NRA design for any given prime number or square of a prime, p, without delving into the set theory used to create them.

Like uniformly redundant arrays, the basis for an NRA is a 1D difference set, C, and is categorised by (v,k,λ). C is a subset of larger group, E, which consists of v elements - E is typically an ascending group of integers from $0 \rightarrow v-1$. Subset C consists of k elements, where the difference between any two values in C occurs exactly λ times[177]. For NRA generation, $\lambda = 1$. Singer sets are a specific case of difference sets that are used in NRA generation, with the following properties[179]:

$$\begin{aligned} v &= p^2 + p + 1 \\ k &= p + 1 \end{aligned} \tag{5.1}$$

The 1D Singer set needs to be converted into a 2D array, where:

$$\begin{aligned} v &= L_x L_y \\ L_x &\perp L_y \end{aligned} \tag{5.2}$$

to form a 2D grid of dimensions L_x and L_y, where L_x and L_y are co-prime, meaning they share no common denominator and can be assumed prime relative to one another. The Singer set is mapped onto the $L_x \times L_y$ array by the modulo of value C_i and the length of the corresponding side L[122]:

$$\text{NRA}\,[x,y] = \sum_{i=0}^{k} \left[\quad \text{mod}\,(\,C_i \mid L_x\,), \quad \text{mod}\,(\,C_i \mid L_y\,) \,\right] \tag{5.3}$$

where $[x,y]$ are the array indices of the NRA. The modulo is the remainder from the division of two values, and is often programatically written as "`a % b`" in C-based languages.

The PSF for the $p49$ NRA of figure 5.2 can be seen in figure 5.3 with its featured sidelobes of uniform signal. The array is normalised by a factor of k, which produces the sidelobe intensity of 0.02 and the peak signal of 1.

Although NRAs exist for all prime numbers, or squares of primes, not all are useful for 2D imaging apertures. The co-prime criteria can yield designs where $L_y << L_x$, which are not suitable for sources which are not similarly long and thin, or detectors which are square or quasi-square. For instance, the $k14$ NRA only has 2 co-primes available for L_x ans L_y: 3 and 61. This means there are fewer NRA designs available for use than MURA ones.

If an NRA was mosaiced akin to an MURA, λ would increase by a factor of 4–8, and the useful PSF properties would no longer be valid. Thus, NRAs are typically run in the undersampled regime to prevent further decoding noise and variation (as described in figure 2.5). Therefore detector dimension matching is less important to NRA imaging, and the reduced number of available designs is less detrimental to their ubiquitous use. The preferred design can be chosen based on the signal increase from k, or the co-primes available from v.

Singer sets are not trivial to construct, with new techniques continuing to be published[180]. This put a theoretical limit on the amount of NRA designs available and their sizes. However, the sets have been found for all "mathematically small" numbers, with online resources listing sets up to $(995007, 998, 1)$†. It is unlikely to require an NRA with dimensions larger than 2883×823, and thus the finite number of Singer set is not deemed here to be a limiting factor on NRA use.

†https://www.dmgordon.org/diffset/

(241, 50, 1) Singer Set

$p = 49 \qquad L_x = 57,\ L_y = 43$

{0, 1, 22, 26, 36, 42, 110, 342, 435, 484, 518, 535, 562, 639, 685, 740, 752, 842, 923, 988, 1003, 1012, 1042, 1231, 1289, 1307, 1380, 1418, 1513, 1544, 1676, 1709, 1762, 1770, 1867, 1878, 1907, 1930, 2055, 2092, 2137, 2140, 2142, 2199, 2206, 2278, 2321, 2334, 2353, 2381}

Set Value	x	y	Set Value	x	y	Set Value	x	y
0	0	0	842	44	25	1867	43	18
1	1	1	923	11	20	1878	54	29
22	22	22	988	19	42	1907	26	15
26	26	26	1003	34	14	1930	49	38
36	36	36	1012	43	23	2055	3	34
42	42	42	1042	16	10	2092	40	28
110	53	24	1231	34	27	2137	28	30
342	0	41	1289	35	42	2140	31	33
435	36	5	1307	53	17	2142	33	35
484	28	11	1380	12	4	2199	33	6
518	5	2	1418	50	42	2206	40	13
535	22	19	1513	31	8	2278	55	42
562	49	3	1544	5	39	2321	41	42
639	12	37	1676	23	42	2334	54	12
685	1	40	1709	56	32	2353	16	31
740	56	9	1762	52	42	2381	44	16
752	11	21	1770	3	7			

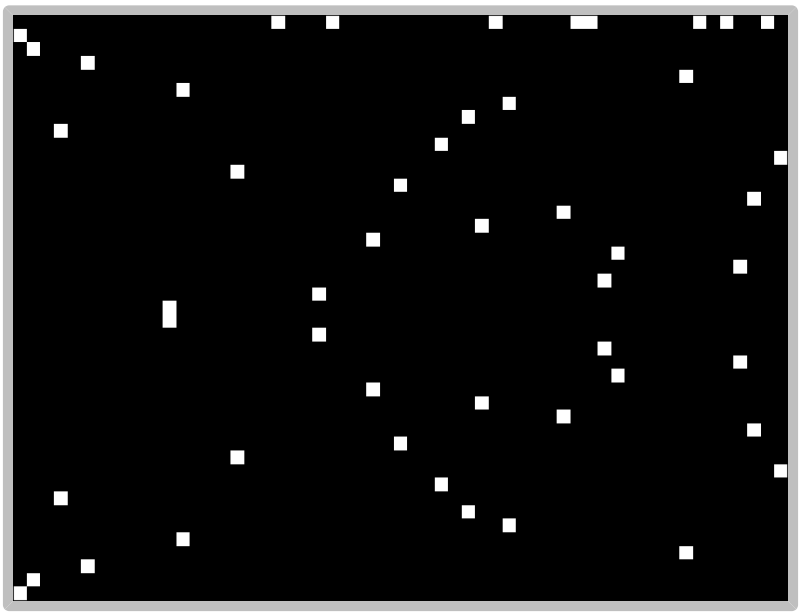

Figure 5.2: The NRA generation method, starting from an exemplar p value of 49. The k value, and corresponding Singer set can then be calculated, and co-primes for L_x and L_y found. The set is then mapped onto the array via equation 5.3 to generate the NRA depicted.

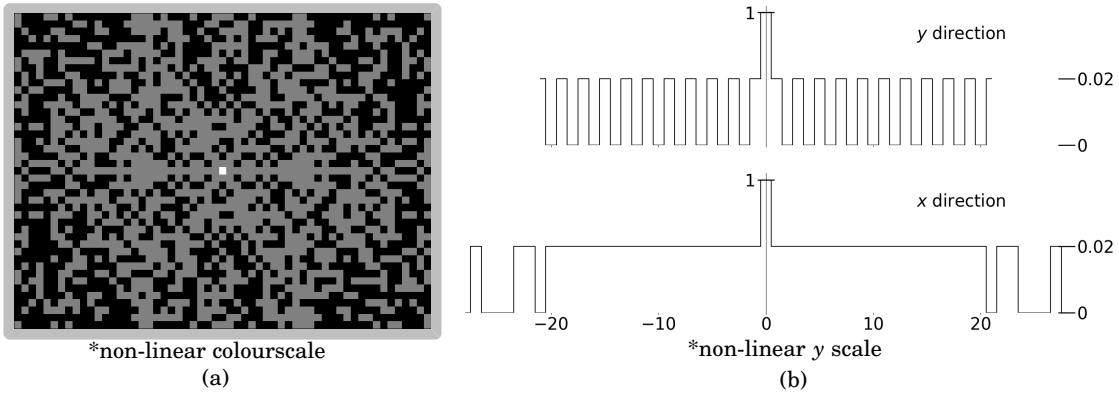

FIGURE 5.3. The normalised PSF for a $p49$ NRA in (a) 2D and (b) lineouts through the centre along the x and y axes. The colourscale of (a) and the y scale of (b) have been made non-linear to highlight the structure within the background.

5.2.2 Point Spread Function

As discussed in chapter 2, the point spread function (PSF) for an NRA is not a δ function, instead having a central spike with featured sidelobes of known magnitude as shown in figure 5.3. The sidelobes will henceforth be referred to as B, and the PSF can be described as:

$$A \star G = \delta + B \tag{5.4}$$

with the reconstruction becoming:

$$\hat{S} = S + S * B \tag{5.5}$$

showing a background component dependent on the source. Ideally, a decoding function would be created such that $A \star G = \delta$. However, an inverse cross correlation is not a well defined mathematical construct. Instead, an approximation for B is required to compensate for the background. Without S being known, $S * B$ must be intuited via an approximation. This can be done through a virtual hologram, D_v, being the hologram that would have been produced if $\hat{S}$ was the original source:

$$D_v = \hat{S} * A \tag{5.6}$$

The comparison of D with D_v can then speak to the form of B. If $\hat{S} = S$, then $D_v = D$ and there was no background added by the decoding process. If $\hat{S} = S + S * B$, and there is intrinsic background in the decoding, D_v becomes:

$$\begin{aligned} D_v &= \hat{S} * A \\ &= (S + S * B) * A \\ &= S * A + S * B * A \\ &= D + S * B * A \end{aligned} \tag{5.7}$$

and the comparison between D_v and D becomes:

$$D_v - D = S * B * A \tag{5.8}$$

The effect of this comparison on the reconstructed image will be $(D_v - D) \star A$:

$$\begin{aligned} (D_v - D) \star G &= S * B * A \star G \\ &= S * B * (\delta + B) \\ &= S * B + S * B * B \end{aligned} \tag{5.9}$$

As a first approximation, the background signal in equation 5.5 can be:

$$(S * B) \approx (D_v - D) \star G \tag{5.10}$$

Substituting this back into equation 5.5, the reconstruction with background compensation becomes:

$$\begin{aligned} \hat{S} &\approx D \star G - (D_v - D) \star G \\ &\approx (2D - D_v) \star G \\ &\approx (2D - D \star G * A) \star G \end{aligned} \tag{5.11}$$

The PSF of the background compensated NRA can be seen in figure 5.4, with an additional assumption that $0 \leq \hat{S}$ (to keep the reconstruction physically possible). The background due to decoding noise has been removed, without altering the peak value.

5.2.3 Source Imaging

Now that a decoding compensation has been found for the PSF, it can be compared against the non-compensated PSF using point sources, large single intensity sources, and more complex variable sources. For the following results, the $p49$ NRA from figure 5.2 has been used in an undersampled system where the detector dimensions are 4 times larger than the NRA. In order to analyse the decoding method and assumptions, the hologram will be made via mathematical convolution of the source and aperture, instead of via ray tracing or Monte-Carlo codes. The system magnification is 1, and all noise is present from decoding error only. $\hat{S}$ has been reduced

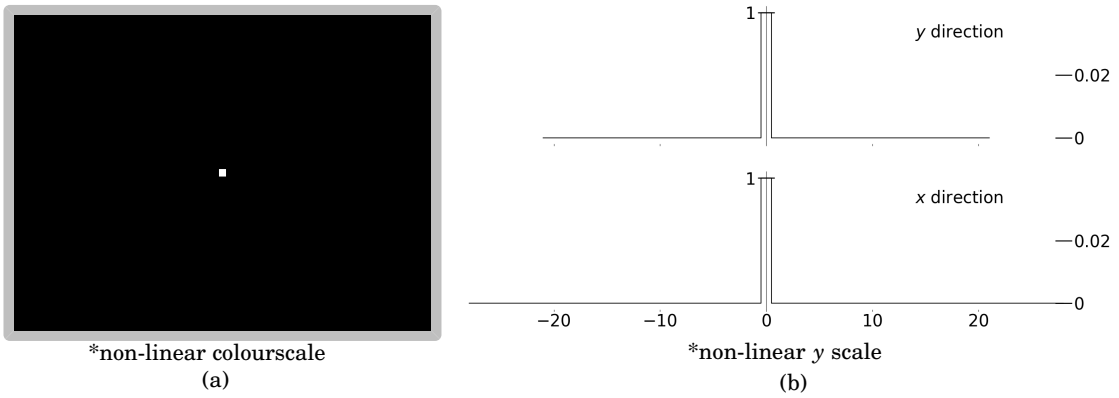

FIGURE 5.4. The normalised PSF for a $p49$ NRA after background compensation from equation 5.11 in (a) 2D and (b) lineouts through the centre along the x and y axes.

in size after post-processing to match that of the A, as this is the maximum field of view for the system.

The reconstructions of 3 point sources with and without the compensation of equation 5.11 can be seen in figure 5.5(a). The compensation has been over zealous and removed all signal, as well as the background. This is likely due to the peak signal in the uncompensated image being higher than the expected value of 1. Instead, decoding noise from the other two point sources overlaps with the signal, forming the peak seen at 1.04. This is confirmed by the background being in three discrete values - 0.02, the error from the PSF of a single point source, 0.04 and 0.06.

Equation 5.11 is formed such that the peaks of $D - D_v = 0$, and therefore the peaks of $2D - D_v = D$. However, if the peaks of $D \neq S$, decoding noise has been introduced in the process, which will be increased during D_v, and the peaks of $D_v \neq D$. This results in D_v peak values larger than D, and if the peaks of $D_v > 2D$ then a blank compensated image is produced, as seen in figure 5.5(a).

Instead, a different factor is required to balance D and D_v to reduce peak inflation.

$$\hat{S} \approx (nD - D_v) \star G \tag{5.12}$$

where n is the ratio of:

$$n = \frac{\overline{D}_v}{\overline{D}} \tag{5.13}$$

where the bar denotes the mean peak values of D_v and D. The peaks of D can be defined as the indecencies where $D > 0.9$, as detectors operate with integer counts and therefore anything non-integer in unphysical. The peaks locations of D_v will be the same as of D.

The effect of the new compensation can be seen in figure 5.6, with the three peaks now visible with no background. However, the magnitude of the peaks is not consistent, with variation from

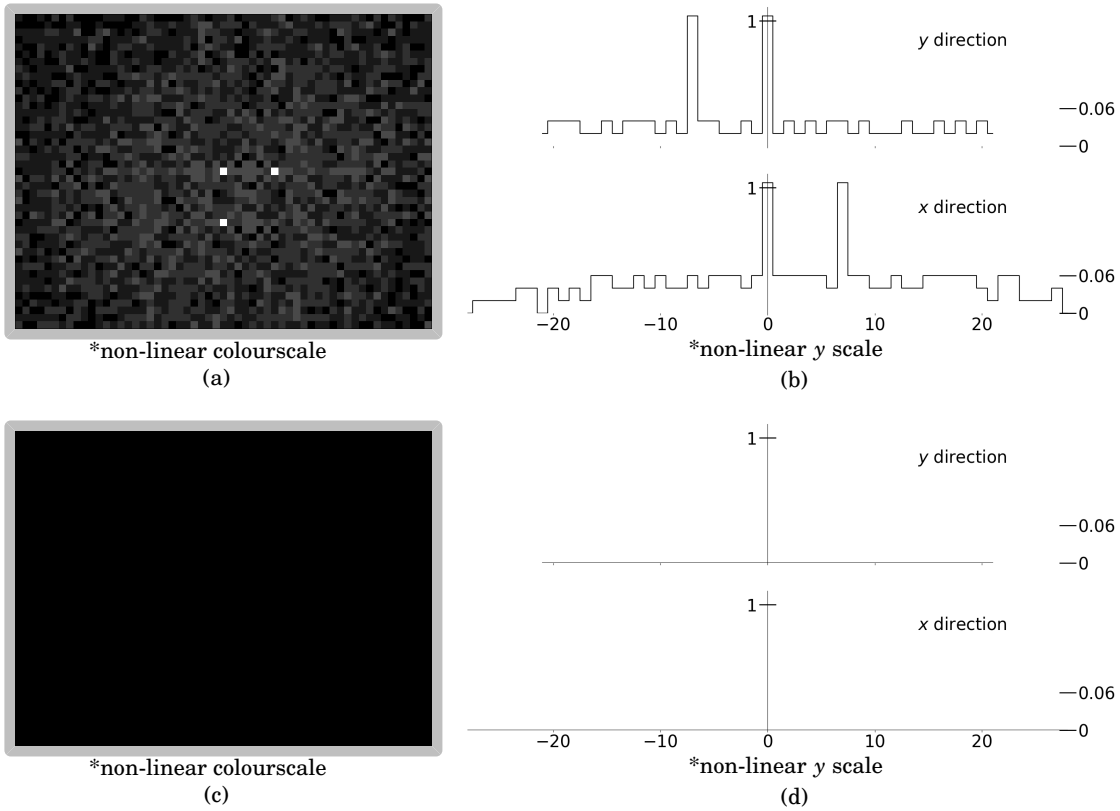

FIGURE 5.5. (left) Decoded images and (right) lineouts for a source constructed from three distinct points using (top) no compensation and (bottom) the background compensation of equation 5.11. The background on the images has been increased by a factor of 5 to highlight the features. The peak of (b) is 1.04.

0.96 to 1.20 seen in the lineout from uniform source intensities. This raises limitations on the use of this compensation technique for experiments where absolute or relative source measurements are required.

Another possible compensation method is via background subtraction in post-processing. With the background intensity of the PSF known, it is possible to approximate the background levels and perform a flat subtraction to $\hat{S}$. The background level varies as a function of source intensity and size, both of which are unknown. Instead, an approximation for maximum background levels can be calculated from $\hat{S}$ - the sum of the standard deviation and mean of all non-zero points.

This post-subtraction processing is demonstrated in figure 5.7. Although the background has been reduced with respect to figure 5.5, the background is still built of three discrete values and is non-zero. One major assumption of this method is that the area of the total image is significantly larger than that of the source and thus the standard deviation and mean are approximately that of the background. This assumption is likely to be less effective the larger the object becomes.

With a larger object, the difference between the three methods (no alteration, compensation,

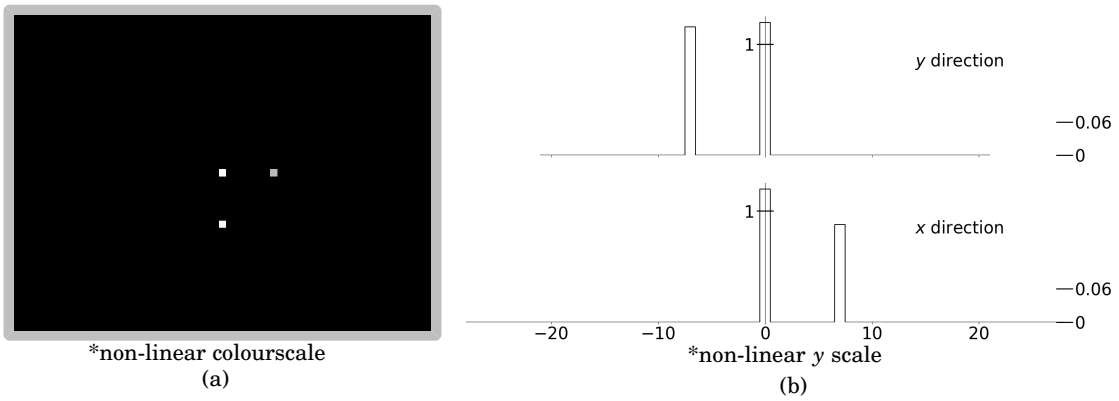

FIGURE 5.6. The (a) decoded image and (b) lineout for 3 point sources imaged through a p49 NRA using the compensation of equation 5.12, with $n = 5.25$ calculated.

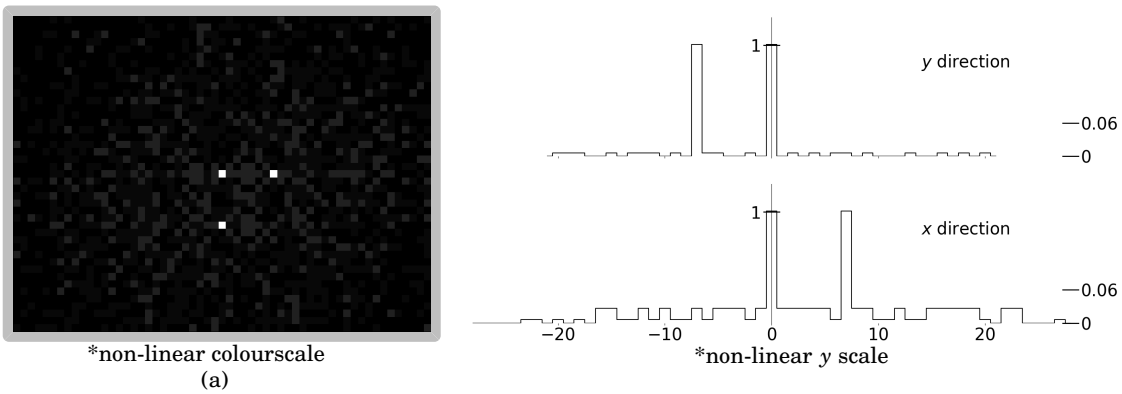

FIGURE 5.7. The (a) decoded image and (b) lineout for 3 point sources imaged through a p49 NRA using the post-subtraction compensation method. Subtraction value of 0.055 was calculated.

and background subtraction) is more readily seen. Firstly, the background levels of the un-altered image in figure 5.8 are still discrete, but with 46 possibilities (the number of pixels in the source) it is looking more like the random high frequency noise discussed in chapter 2.

Although the peaks of the post-subtraction have been reduced, they are still not equal to the input intensity of 1. The decoding noise also becomes apparent in variation of the peak intensities, as the input source is uniform. As the subtraction is uniform, it will not alter the deviation in peak intensity. Although there are more 0 values present than the unchanged image, the lineouts show a majority of pixels have a non-zero value. This suggests that the standard deviation and mean of the image are low, with higher concentrated areas of decoding noise. The background appears to be higher closer to the source, with a drop-off towards the edge of the image.

The compensation of equation 5.12 has removed the entirety of the background from the space invader. However, it has also exacerbated the variation in the peak intensities, with the relative

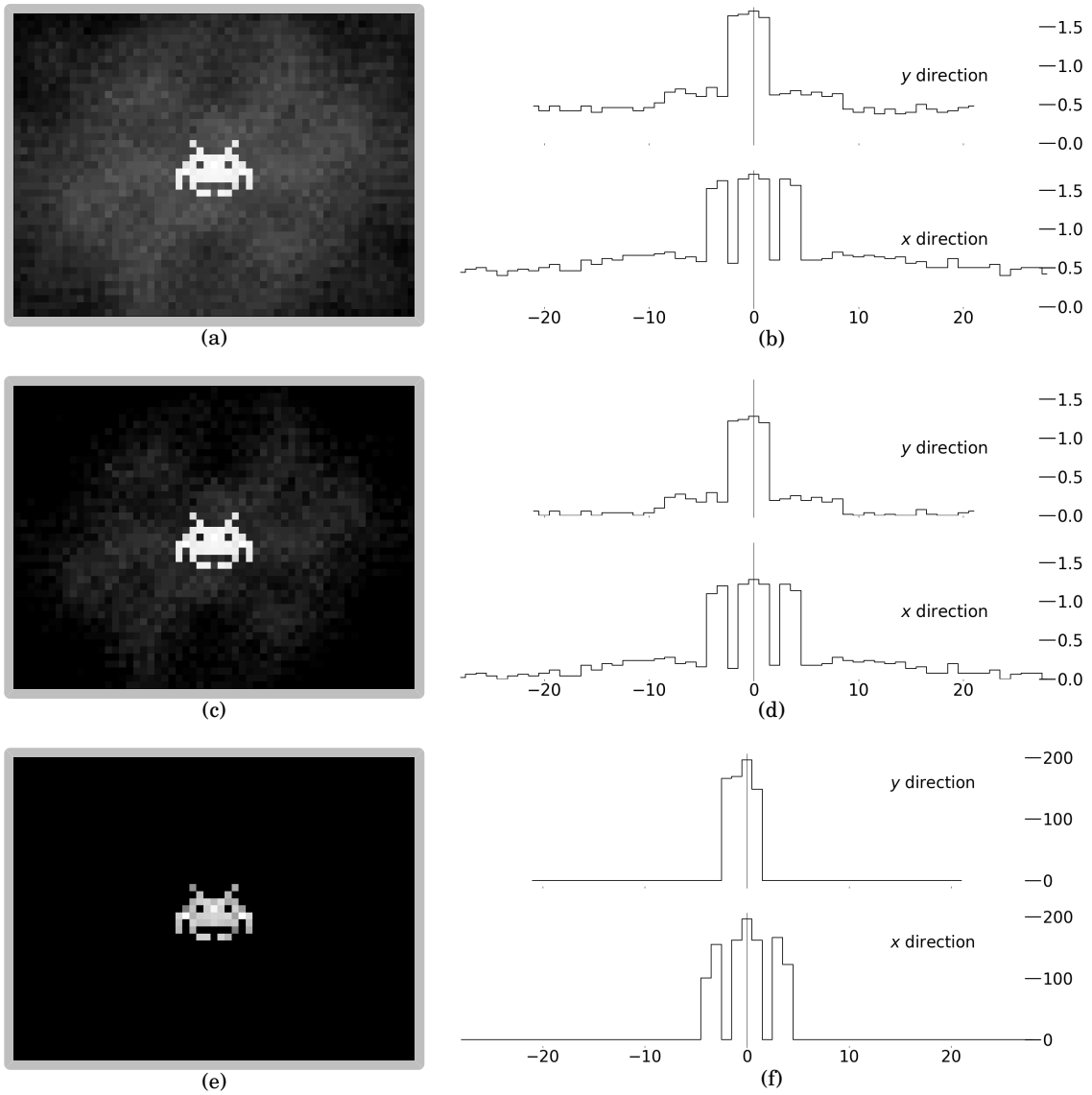

FIGURE 5.8. (left) Decoded images and (right) lineouts for a Space Invader source of uniform intensity 1. The (top) unaltered decoded image has undergone (middle) post-substraction processing with a value of 0.423 calculated and (bottom) the compensation of equation 5.12 with $n = 14.1$.

shifts the same between peaks, although the amplitude change is magnified. Furthermore, the peak intensity is *ca.* 200 times that of the input source, further suggesting the compensation will be unsuitable for imaging where intensities and relative peaks are required to infer source properties. Although the source shape is still imaged, allowing NRAs to be used for purposes such as laser spot imaging.

Figure 5.9 compares the three systems for a large, varying intensity source. The uncompensated and post-subtraction images have negligible change between them. While the Gaussians

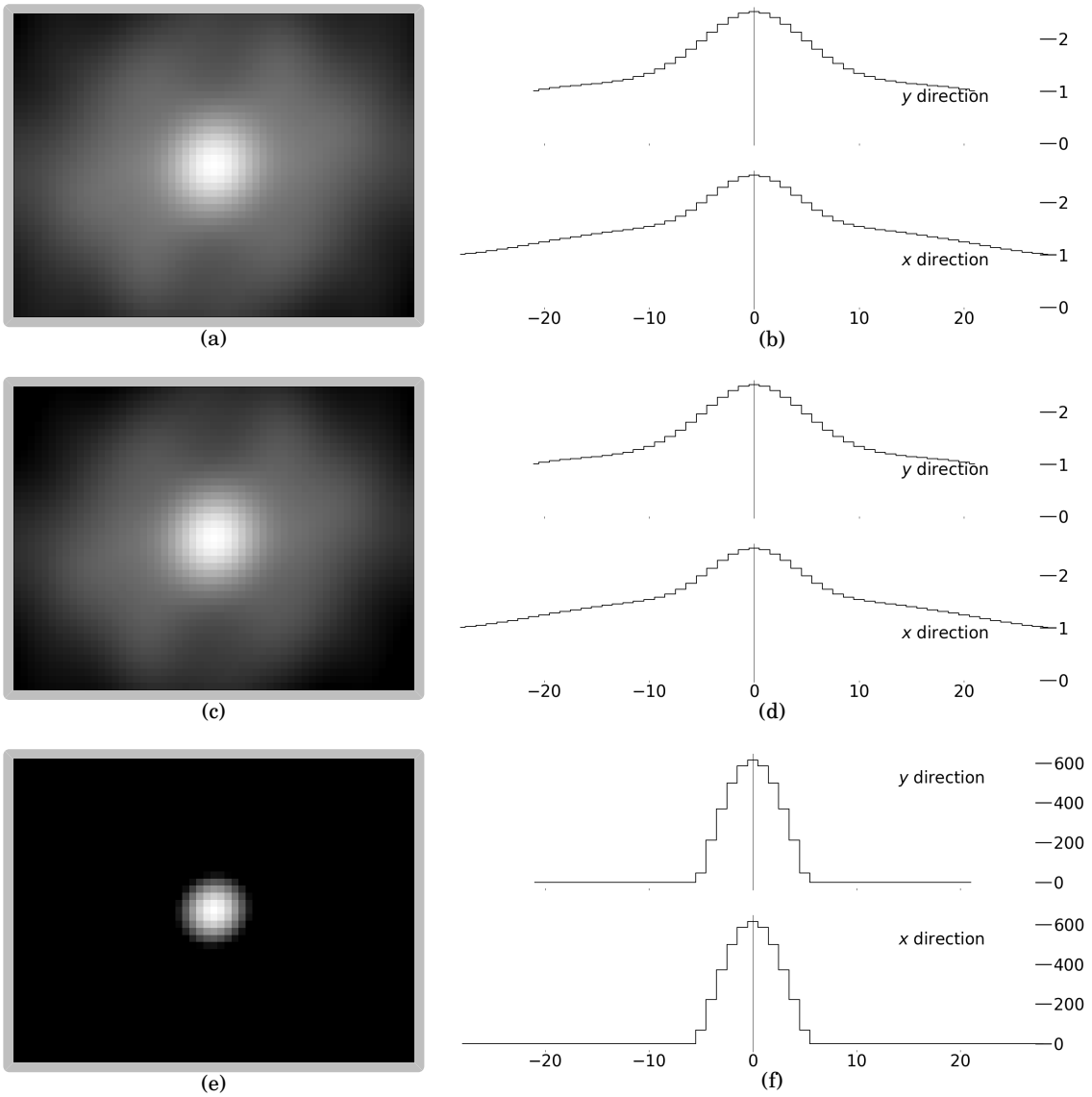

FIGURE 5.9. (left) Decoded images and (right) lineouts for a Gaussian source of peak intensity 1 and full width half maximum of 10 pixels. The (top) unaltered image has undergone (middle) post-substraction processing with a value of 0.685 calculated and (bottom) the compensation of equation 5.12 with $n = 23.0$.

have the correct full width half maximum (FWHM) of the input source in the x direction, they are sitting atop a high background that increases towards the centroid of the Gaussian. However, there y direction measures a FWHM of 6. For an unknown source, it would be difficult to ascertain what was true source information and what was decoding background.

The compensation reduces the background to 0, at the expense of everything beyond the FWHM and n inflated peak height from 1 to 600. This was a constant trend, with the Gaussian always being reduced to its FWHM, which if known can still possibly be used experimentally

Furthermore, there is a slight skew on the Gaussian leaning towards the $x = y$ direction.

In conclusion, none of the measures presented eradicative the decoding noise from using a NRA. The background term in equation 5.4 prevents large scale sources being accurately decoded without large noise components being present. Two possible solutions have been suggested, the compensation more suited for background removal at the expense of larger source intensity variation, and the post-subtraction has less source intensity variation at the expense of higher background levels. Either can be used to try and counteract inherent NRA imaging issues, depending on the purpose of the application.

5.3 Banded Spectral Coded Aperture

Construction of a BaSCA requires multiple NRA designs to be placed onto a single aperture. The detector is a combination of each hologram from every NRA design overlaid, where the spectral information is encoded within the holograms. Thus, the detector need not be spectrally resolving, reducing the price of the overall imaging system. Furthermore, when imaging sources above 10 keV, the quantum efficiency of spectrally resolving detectors often drops to below 1%, whereas non-resolving cameras and analogue detectors are able to image up to MeV energies using image plate or scintillators[170]. Thus, a wider range of detectors can be used for a Ross pair based banded system. BaSCAs using scintillators will also have low quantum efficiency at higher energies, but the higher throughput of an NRA over a single pinhole can compensate for reduced detector efficiency.

Each NRA is decoded separately, and then subtracted from one another in pairs to produce spectral bands. In order for each hologram to be decoded as cleanly as possible, the NRA designs would ideally be mutually non-redundant. However, this is not possible using multiple NRAs, and due to the mathematical complexity of NRA construction it would be impractical to derive new families of algebraic theory in order to test a BaSCAs possible effectiveness. Instead, reducing the redundancy between NRAs is the more prudent approach.

There is an expectation that the intrinsic background from decoding will increase as more redundancy is introduced. As such, the aggressive background compensation of equation 5.12 will be used on each decoding process individually to reduce backgrounds which may overlap and increase beyond the levels of the intended signal.

For the following study, the $p49$ NRA used previously will be used as the basis for a BaSCA. Three filters will be used, with colour analogous to the energies they are transmissive to - red, green, and blue in descending order of energy. Thus, the spectral bands to be created are red-green, green-blue, and sub-blue. Translation of an NRA will cause decoding error for every hologram due to the high levels of redundancy caused. Instead, rotation will limit extra redundancy created by having multiple designs. Orthogonal rotations will still hold some redundancy on a square based grid. For the tri-energy BaSCA, 120° rotations were found to hold the least redundancy.

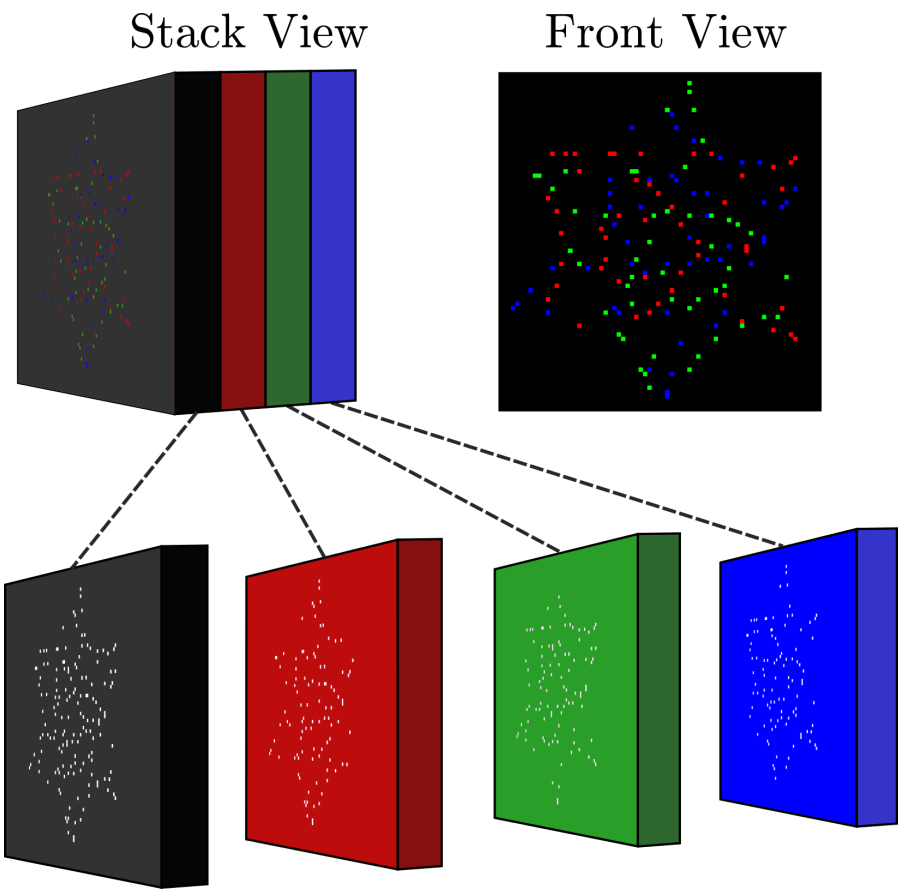

FIGURE 5.10. Explosion diagram of a $p49$ $r3$ BaSCA.

The explosion diagram of the BaSCA can be seen in figure 5.10, with 3 rotations ($r3$). The black substrate may not be necessary for all BaSCAs, but it will be useful for broadband sources with a significant flux above red energy. The red filter must have the designs for the green and blue machined into it, so it does not affect the transmission properties of those NRAs. The same logic applied for the other two filters.

It is noted that the machining tolerances necessary to machine and stack the multiple filters to the required precision for a high-resolution BaSCA may be a limiting step in their production and utility. However, for this proof on concept the machining difficulties will not be considered further.

The capability of the $r3$ BaSCA will be evaluated for three identical sources, each emitting inside one of the spectral bands - point sources, extended objects of uniform intensity, and large objects of varying intensity.

5.3.1 Point Source

The reconstruction of 3 point sources can be seen in figure 5.11. Despite the hologram of 5.11(b) holding no spectral information, the sources have been cleanly reconstructed without any decoding noise using the background approximation of equation 5.12 with n values around 6.5. The uncompensated image is also able to reconstruct the three sources in the correct locations, with a maximum background of 0.18. This is higher than the PSF of figure 5.3, and that of the 3 point source of figure 5.5(a).

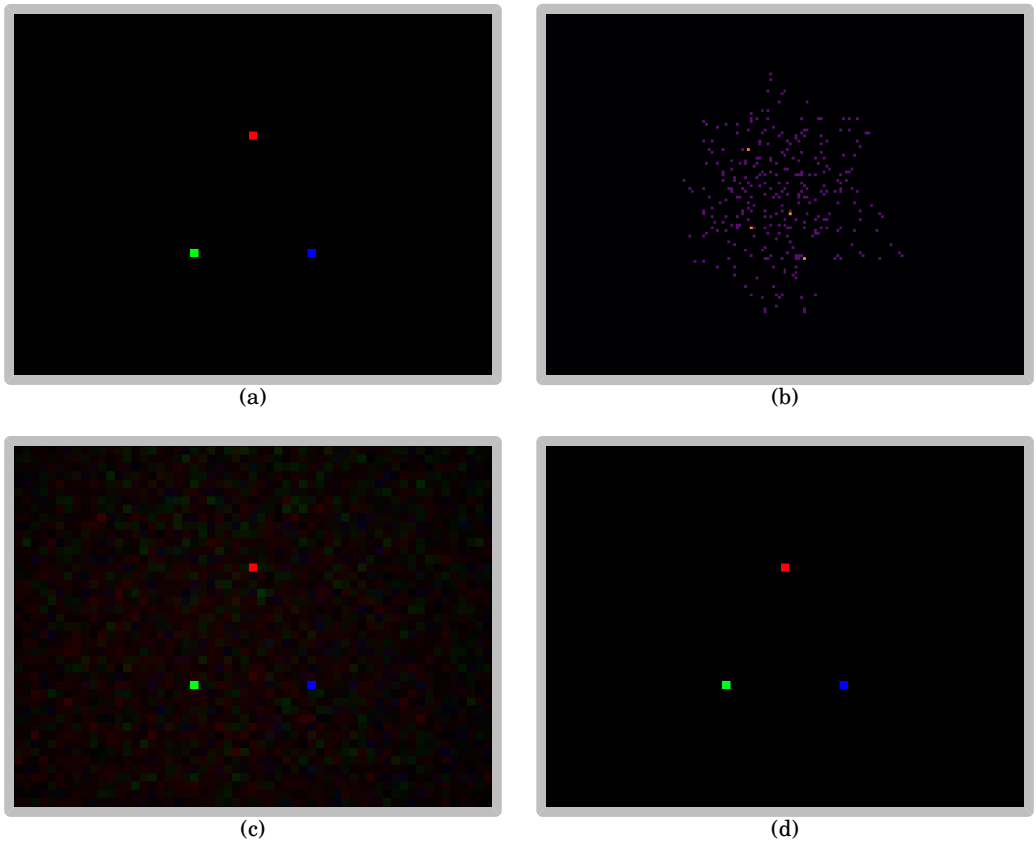

FIGURE 5.11. Imaging 3 points sources of different energies with the $p49$ $r3$ BaSCA of figure 5.10. The original sources (a) produce (b) the hologram, with the detector counts varying between $0-2$. The hologram is decoded three times and overlaid upon one another to show all three spectral bands in a single image. The decoding is performed using (c) no compensation and (d) the compensation of equation 5.12 with $n_{\text{red}} = 6.2$, $n_{\text{green}} = 6.6$, and $n_{\text{blue}} = 6.8$.

5.3.2 Extended Source

The effect of higher background in the uncompensated image is more apparent in figure 5.12 when imaging larger objects. The image is dominated by a strong red background, with pockets

of blue and green. Background counts in red are as high as 0.74, with the red source intensity varying between 0.84–1.00. The compensation has been able to remove a vast majority of this background, with clearer images of green and red energies visible. However, the lower blue energy reconstruction has been detrimentally affected, with intensities as low as 0.25 within the source, with a uniform intensity of 1 expected.

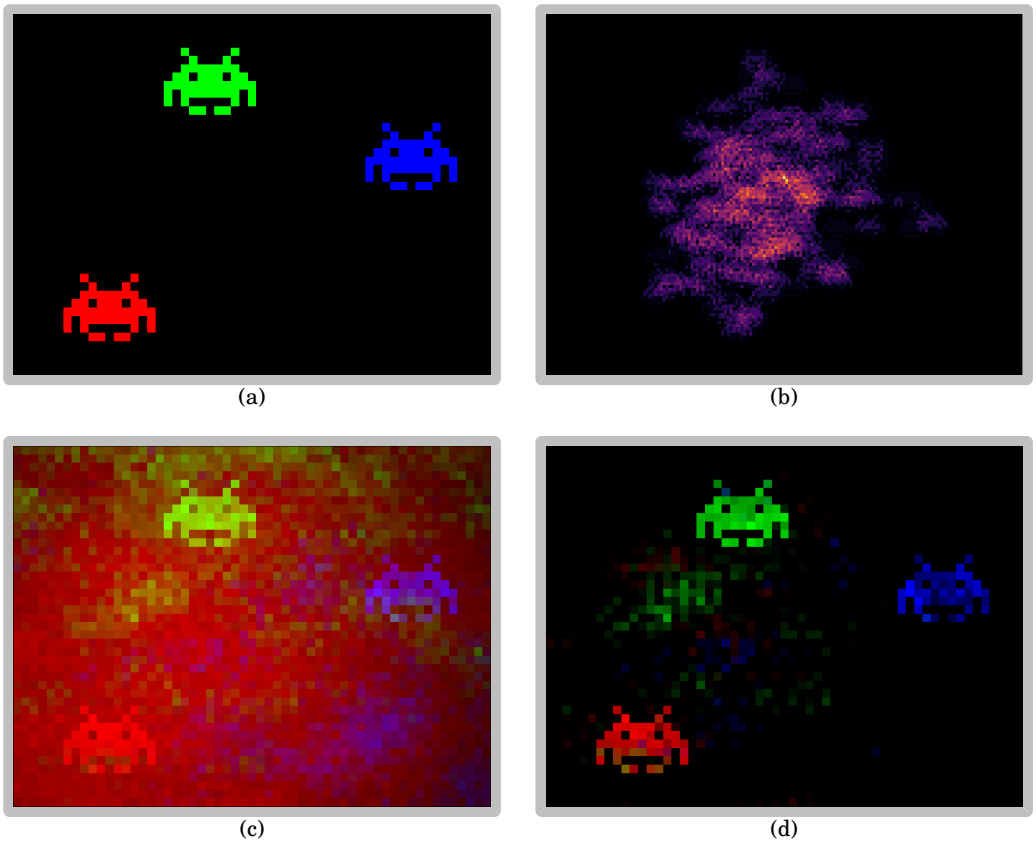

(a) (b) (c) (d)

FIGURE 5.12. Imaging 3 space invaders of different energies with the $p49\ r3$ BaSCA of figure 5.10. The original sources (a) produce (b) the hologram, with the detector counts varying between $0-12$. The hologram is decoded three times and overlaid upon one another to show all three spectral bands in a single image. The decoding is performed using (c) no compensation and (d) the compensation of equation 5.12 with $n_{\text{red}} = 29.2$, $n_{\text{green}} = 29.5$, and $n_{\text{blue}} = 28.8$.

With sources larger than k, it can be seen in figure 5.13 that the limit of BaSCA has been reached. Neither the compensated nor uncompensated images are able to accurately decode the source positions or size, with little to no correlation between these images and the original sources. The spectral information within the hologram has been lost to the decoding background, with the decoding unable to separate the reconstructed blue source from the original green.

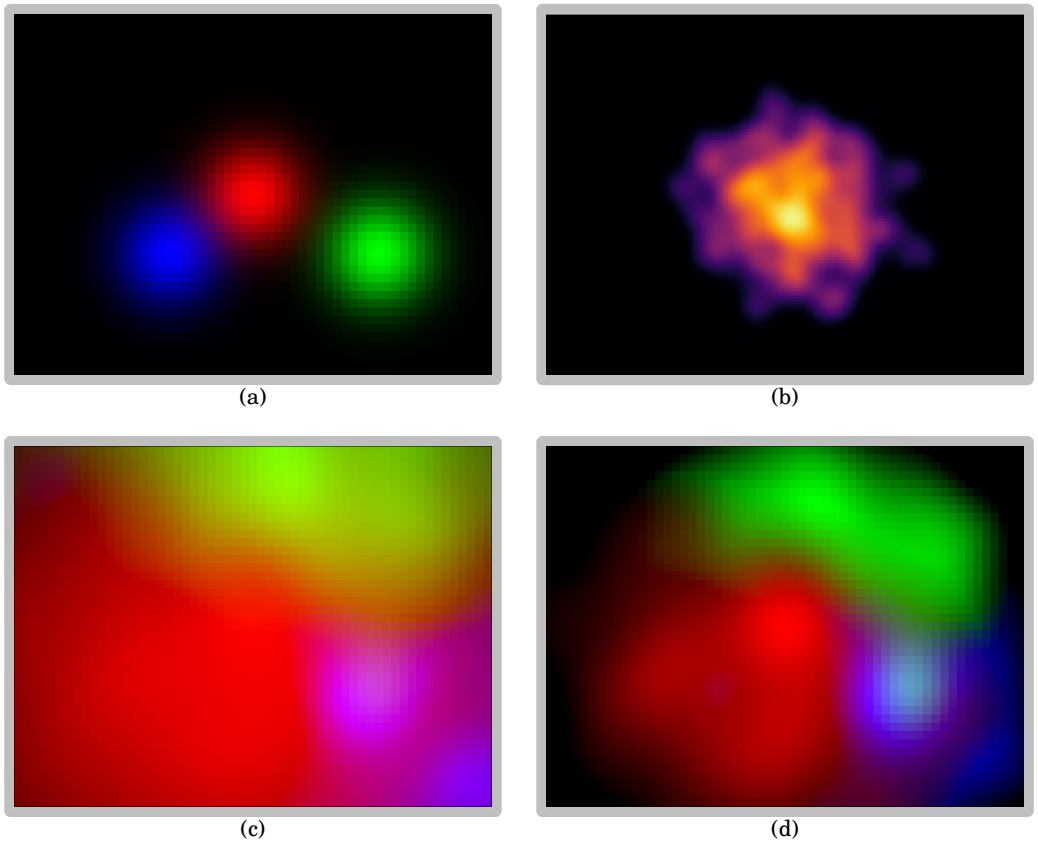

(a) (b) (c) (d)

FIGURE 5.13. Imaging 3 Gaussian sources of different energies with the $p49\ r3$ BaSCA of figure 5.10. (a) The original sources produce (b) the hologram, with the detector counts varying between 0–16. The hologram is decoded three times and overlaid upon one another to show all three spectral bands in a single image. The decoding is performed using (c) no compensation and (d) the compensation of equation 5.12 with $n_{\text{red}} = 33.3$, $n_{\text{green}} = 32.9$, and $n_{\text{blue}} = 33.4$.

5.3.3 Complex Source

A similar trend can be seen the complex source shown in figure 5.14. This is a Gaussian profile akin to those detected on laser - solid target experiments. Despite the original source profile being a mathematically perfect Gaussian spanning all three filter energies, the reconstruction is unable to produce an image similar to the object. The transitions between filter energies is present, but heavily masked by the decoding noise both with and without the compensation.

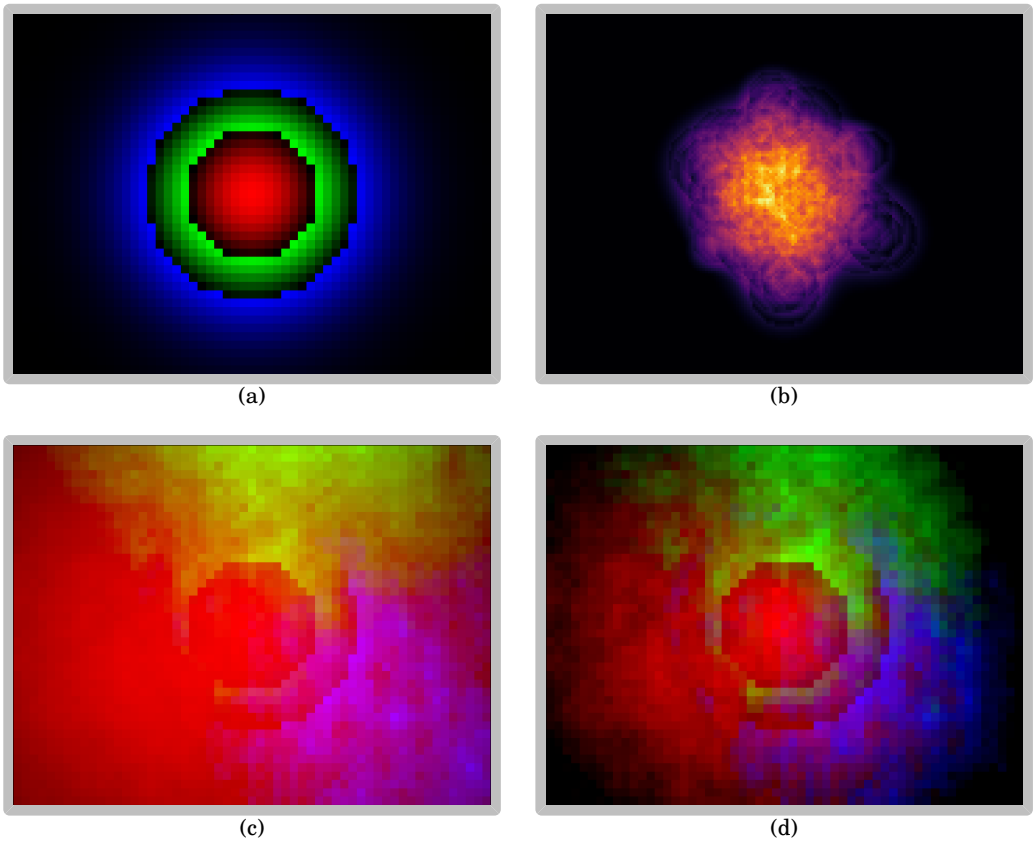

FIGURE 5.14. Imaging a single Gaussian source ranging across 3 energies with the $p49$ $r3$ BaSCA of figure 5.10. The original source (a) produce (b) the hologram, with the detector counts varying between $0-23$. The hologram is decoded three times and overlaid upon one another to show all three spectral bands in a single image. The decoding is performed using (c) no compensation and (d) the compensation of equation 5.12 with $n_{\text{red}} = 35.4$, $n_{\text{green}} = 35.5$, and $n_{\text{blue}} = 36.1$.

5.4 Conclusion

In conclusion, the possibility of combining Ross pair filters with coded aperture theory to create a banded spectrally resolving imaging system without the need for specialist resolving detector was discussed. Due to the background term in NRA decoding, and the lack of other available aperture designs, a compensation technique is required in an attempt to mitigate the background due to decoding. This compensation worked best with a limited source size less than k, the number of perforations in the NRA. A similar trend was seen within the BaSCA, where point sources could be accurately decoded separately, but the amount of background scaled with source size and its relation to k.

There is scope for application of the current BaSCA in astrophysics, where point sources are routinely imaged. Security imaging could also make use of this technique, trying to detect

the presence and location of dangerous substances within cargo. Characteristic emission from radioactive decay of nuclear material is well characterised, as is characteristic emission from photo-excited atoms of other compounds classified as dangerous. Therefore, a BaSCA can be designed to spectrally select the desired substance to scan for, and a LFWA x-ray source used to photo-excite the cargo. With a large-resolution aperture, the location of any classified dangerous substances can be identified within the cargo as a point source on the imaging plane.

However, for laboratory imaging the background of equation 5.4 prevents the BaSCA being ubiquitous in its current form. Therefore, a new aperture design would be required to utilise the BaSCA system. If a suitable A and G pairing could be constructed with a similar open fraction to the NRA, but with a PSF of a perfect delta function, the background would no longer scale with source size. This would allow large sources to be decoded accurately, without the need for the compensations presented here. In order to create the new aperture design required, either geometric mathematics or a machine learning model would be required. Machine learning could also be used to generate specialist BaSCA designs where the separate filter designs are non-redundant between themselves, to further decrease the amount of decoding noise.

CHAPTER 6

FUSION NEUTRON IMAGING

Fusion neutrons are notoriously difficult to image, with 2.45 MeV and 14.1 MeV neutrons from deuterium-deuterium (DD) and deuterium-tritium (DT) fuel mixes respectively being highly penetrative through any substrate. The difficulty is compounded when imaging inertial confinement fusion (ICF) neutron implosions, where µm scale resolution is required to show any notable asymmetry in implosion geometry. This necessitates small diameter perforations to be machined through thick substrates at considerable cost, with high manufacturing difficulty, alignment precision and image reconstruction to make a working aperture.

The National Ignition Facility (NIF) is the largest ICF experiment in the world, and will be used here as a case study. The CASPA (chapter 4) has already demonstrated that substrate thickness can be substantially reduced without degrading imaging quality. This chapter will be dedicated to applying CASPA principals to neutron imaging on NIF, to discuss whether it can be used to design a cheaper and easier to implement imaging system with the same imaging capability. This is achieved by ascertaining a CASPA thickness for DT neutrons, and attempting to apply collimator correction factors to prevent noisy reconstructed images. It was found that the collimator effect is not the predominant mechanism for the introduction of noise, and iterative reconstruction methods are explored. Starting with maximum-likelihood expectation-maximization already used on NIF results[102,181–183], which is found to produce suboptimal reconstructions for CASPA images, improvements using maximum a posteriori principals are explored.

6.1 Experimental Constraints

Currently, neutron imaging on NIF is performed by the neutron imaging system (NIS) using a grand array of 20 pinholes, imaging the source onto a gated, intensified charge coupled device (CCD). The neutron imaging aperture (NIA) and CCD are 20 cm and 28 m from the source, respectively. The NIA substrate is solid gold, with a thickness of 20 cm[184]. The triangular perforations are tapered from 5 μm closest to the source out to 226 μm facing the detector[183], to overcome the collimator effect and increase the individual field of view per perforation without compromising the resolution capability of 0.1 μm^{-1}[102]. The individual field of view for any one perforation is approximately 200×200 μm, with a total NIA field of view combining to be 500×700 μm[102]. Therefore, images cannot be formed through all 20 grand array pinholes simultaneously.

Competition is rife for space on NIF, between all 192 beam paths and the multitude of diagnostics focused on the ~1 cm long cylindrical capsule in the centre of the 10 m diameter chamber[94]. For neutron imaging, time of flight (ToF) is often used to acquire spectral information about neutrons incident on the detector, with ToF paths of 10–25 m typical for this technique and require imaging lines to be created through the radiation shielding. It takes considerable time, cost, and experimental down-time to create new imaging lines, and as such it is more efficient to design diagnostics for pre-existing imaging lines.

For aperture development, it is prudent to use pre-existing detector infrastructure, as well as imaging lines, for design and future experimentation. Through discussions will collaborators, it is known that an imaging line with a detector position 11.5 m from the source is often used for initial diagnostic tests, and 2 inch square image plate is common for initial aperture results as it has a comparable resolution of 500 μm to the CCD. As discussed in chapter 4, these parameters can be used to calculate a suitable MURA p value through equations 4.10, 4.11, and 4.12. In order to match the NIS resolution capability, a $p97$ aperture is required with 9.9 μm elements, situated 11.5 cm from the capsule. The difference in design between the CASPA and the NIA can be seen in figure 6.1.

It is necessary that a novel aperture can be demonstrated to be - at very least - capable of producing similar results to the NIA. It is for this reason the resolution capability of 0.1 μm^{-1} was chosen for the design shown. However, due to the decoupling of signal and resolution for coded apertures discussed in chapter 2, as long as the design can be fabricated, it is possible to better the current resolution capability on NIF without SNR detriment.

6.2 Analytical Method

Two main analytical methods will be used in this chapter - one for assessing the substrate effectiveness as a CASPA, and the other for analysis of reconstructed images. Herein, Gaussian profiles are used for first approximations of neutron geometries from NIF implosions.

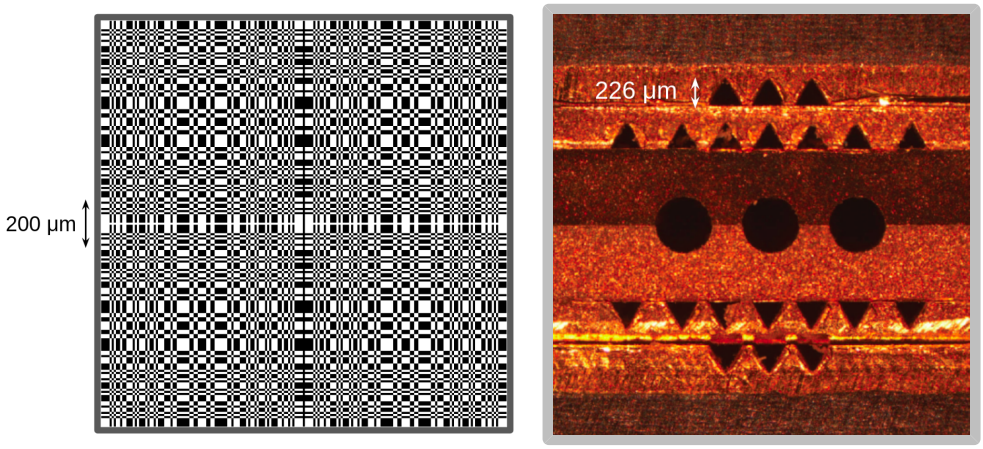

FIGURE 6.1. A comparison of the back surface (detector facing) of (a) the proposed $p97$ CASPA and (b) the NIA. The three large holes in the central row of (b) are for penumbral imaging.

6.2.1 Furtive Direct Ratio

The furtive to direct ratio (FDR) has been created here as the ratio between particles that are perturbed or attenuated away from the in-line pixel, and particles that hit the in-line pixel as if the substrate was not present at all. It is used as a quantitative measure of a substrates effectiveness of creating hologram contrast and is defined as:

$$\begin{aligned} \mathrm{FDR}_j &= \frac{\lambda_{\hat{j}} + \alpha}{\lambda_j} \\ &= \frac{\Gamma - \lambda_j}{\lambda_j} \end{aligned} \tag{6.1}$$

where j is the in-line pixel the particle would hit unperturbed, $\bar{j}$ is every other pixel on the detector besides j, α is the number of particles attenuated by the substrate, and Γ is the total number of particles in the simulation. A higher FDR will create a working CASPA with thinner substrates, and thus is desirable for high-energy imaging.

6.2.2 Legendre Mode Fitting

When comparing novel advancements with already implemented diagnostics, it is imperative to compare them equivalently such that the conclusions are meaningful. NIF neutron data analysis uses Legendre polynomial fit at the 17% contour to quantify the asymmetry of neutron sources[182], and thus it will also be used here. It is performed in polar coordinates using a least-squares fitting routine. For this, the origin of the hotspot needs to be known, O^{index}, and O

is used to define the 17% contour value, $C^{17\%}$. Then, the Legendre mode fit can be applied with the following equation:

$$r_{17\%}(\theta) = \sum_{n=0}^{N} P_n L_n(\theta) \tag{6.2}$$

where $r_{17\%}(\theta)$ is the radius of origin to contour at angle θ, and $L_n(\theta)$ can be defined succinctly through Rodrigues' formula[185] as:

$$L_n(\theta) = \frac{1}{2^n n!} \frac{d^n}{d\theta^n}(\theta^2 - 1)^n \tag{6.3}$$

Typically, $N \sim 8$ is adequate for NIFs purposes, and the constraint of $P_1 = 0$ is added to prevent movement of the contour centre. Furthermore, odd asymmetry modes (P_3, P_5, P_7) should not be required due to reflection symmetry[186], but can still be present from physical imperfections in fabrication processes[187]. Common asymmetries and their Legendre polynomial factors can be seen in figure 6.2.2.

NIF remove single-pixel hotspots before analysis, and then assume a background of 0 while conducting this analysis. This allows O to be the maximum of the image, and $C^{17\%} = 0.17 \times O$. However, for a CASPA the assumption of 0 background is inappropriate. Instead, the contour needs to be defined as:

$$C^{17\%} = \tilde{\lambda}_{\hat{j}} + 0.17(O_j - \tilde{\lambda}_{\hat{j}}) \tag{6.4}$$

where j is every pixel within the current estimate for the 17% contour, $\hat{j}$ is every pixel outside j (and used as the definition for the image background), $\tilde{\lambda}_{\hat{j}}$ is the median of said background, and O is calculated through j's centre of mass. It can be seen in equation 6.4 that j is required to calculate $C^{17\%}$, while $C^{17\%}$ is required to calculate j. Therefore, this cannot be solved linearly, and requires a recursive approach:

$$C^{17\%}_{i+1} \simeq \tilde{\lambda}_{\hat{j},i} + 0.17(O_{j,i} - \tilde{\lambda}_{\hat{j},i}) \tag{6.5}$$

where i is the iterator, with initial conditions O_0 = image maximum and $\tilde{\lambda}_0$ = image minimum. The stopping condition for this recursivity is that:

- $C^{17\%}_{i+1} = C^{17\%}_i$
- $O_{i+1} = O_i$
- $O^{\text{index}}_{i+1} = O^{\text{index}}_i$

and is capped at 100 total iterations. The fitting routine gives a χ^2 value in lieu of error analysis. This can be converted into a fit "goodness", where goodness < 1 is desirable to be classified as an appropriate fit. Goodness is defined as:

$$\text{Goodness} = \frac{\chi^2}{M - N} \tag{6.6}$$

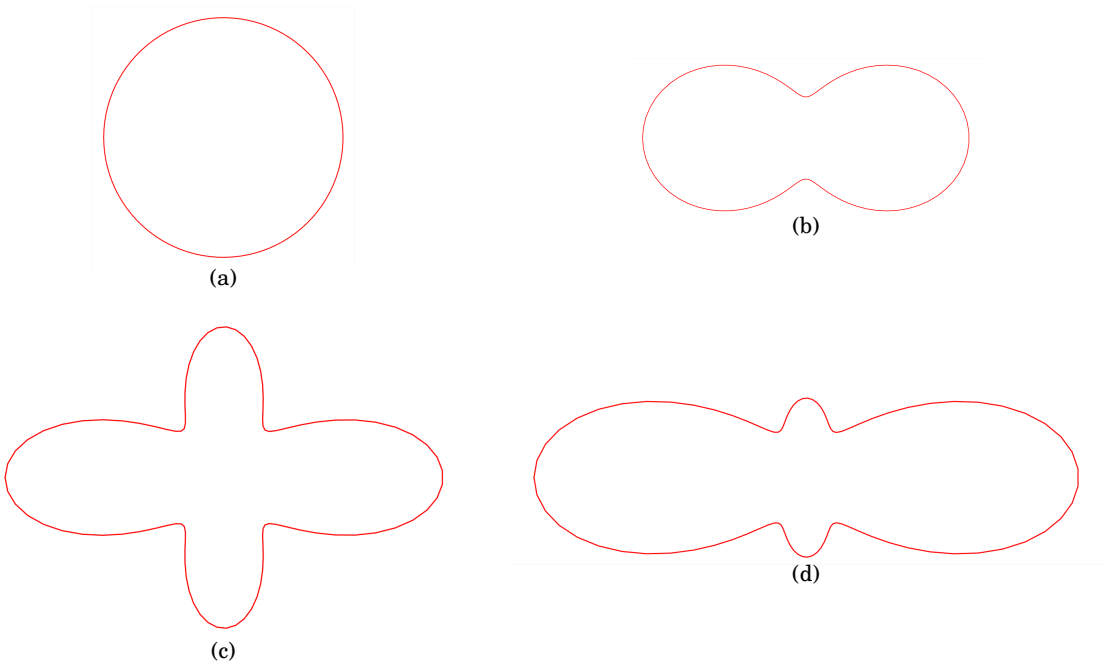

Asymmetry	P_0	P_1	P_2	P_3	P_4
(a)	1	0	0	0	0
(b)	1	0	1	0	0
(c)	1	0	0	0	1
(d)	1	0	1	0	1

(e)

Figure 6.2: Common implosion asymmetries found within ICF implosions (a–d) and (e) their corresponding Legendre modes (equation 6.2). Common asymmetries are even Legendre modes, as the contour should always be cyclic.

where N is the total number of Legendre modes fitted, and M is the number of data points used in the fit. The higher the goodness, the worse the fit is perceived to be.

6.3 Substrate Design

6.3.1 Substrate Material

The CAPSA discussion of figure 4.6 shows that a combination of attenuation and scatter in a substrate is more effective than either individually. As highlighted in Chapter 2, the mechanisms for scatter and attenuation of fast neutrons is different from photons, and as such an effective substrate for photons may not be as effective for neutrons. For this chapter three substrate materials will be compared, as shown in table 6.1:

- Gold, with the highest scatter probability
- Tungsten, with the highest attenuation probability
- Platinum, a moderate balance of scatter and attenuation probability

2.5 MeV			
Substrate	Scatter $_{\text{elastic}}$ (/cm)	Scatter $_{\text{inelastic}}$ (/cm)	Attenuation (/cm)
Tungsten-182	0.233±0.005	0.15±0.01	$(3.5\pm0.3)\times10^{-3}$
Platinum-194	0.25±0.02	0.14±0.01	$(1.9\pm0.5)\times10^{-3}$
Gold-197	0.303	0.165	$(2.26\pm0.05)\times10^{-3}$

14 MeV			
Substrate	Scatter $_{\text{elastic}}$ (/cm)	Scatter $_{\text{inelastic}}$ (/cm)	Attenuation (/cm)
Tungsten-182	0.166±0.006	0.032±0.006	$(6\pm6)\times10^{-5}$
Platinum-194	0.15±0.01	0.02±0.01	$(6\pm6)\times10^{-5}$
Gold-197	0.174	0.036	6.6×10^{-5}

Table 6.1: The probability of interaction per unit length of *ca.* DD and *ca.* DT fusion neutron energies with various substrates, in their most abundant isotopes. Cross sections from joint evaluated fission and fusion library (JEFF)[188], and converted with data from the CRC handbook of chemistry and physics[189].

Figure 6.3 shows the FDR results from a Geant4 pencil beam of DD and DT fusion neutrons striking the substrate of varying thickness and material. The detector plane is 40 mm from the back surface of the substrate, with a pixel size of 0.01 mm^2. It can be seen that neither the scatter or attenuation mechanisms dominate, with pure platinum having a consistently higher FDR than gold or tungsten across both incident neutron energies and all thicknesses tested.

It is worth noting that the NIA is manufactured is gold, yet other high-energy x-ray diagnostics use doping to achieve similar properties to high-Z materials (tungsten and lead, mostly) in easier to machine substrates. These doped materials are not being considered here, due to a lack of cross section data on JEFF[188]. However, the analysis performed here can be done with any substance of known chemical composition and density.

An approximation of doped substances was created using stacked materials - to explore whether layering gold and tungsten (due to their prowess in scattering and attenuating fusion neutrons) in a multi-metal substrate could out-perform a mono-metal one of equivalent thickness. However, for every stack ratio between gold and tungsten thickness the FDR was lower than that of mono-metal tungsten substrates. Furthermore, changing the order of materials in the stack was found to make no change in FDR over the simulations conducted.

The effect of scatter on the FDR can be seen in contrasting figures 6.3(a) and 6.3(b), and the relative proximity of the platinum and gold (the higher scatterers) to that of tungsten. The performance gap between platinum and tungsten for DT is marginal, with the largest percentage

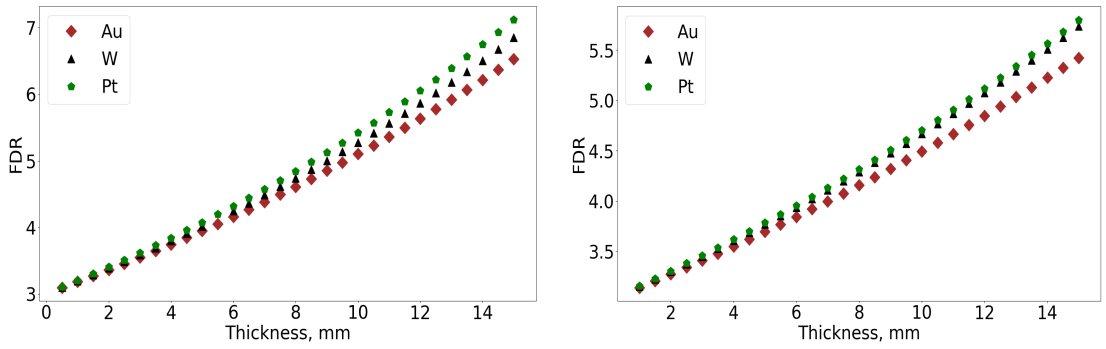

FIGURE 6.3. A comparison between the FDR of tungsten, platinum, and gold substrates with (a) DD and (b) DT fusion neutrons. Tungsten has the greatest attenuation cross-section, gold has the better scattering cross-section, with platinum between each extreme.

difference being 1% at the 14 mm thick substrate. However, the cost of raw materials varied drastically, with platinum orders of magnitude more expensive than tungsten ($32.39 and $0.03 per gram in 2018, respectively[190]), making platinum as a substrate inaccessible to all but the largest facilities with the matching budgets. As such, tungsten will be used as the substrate of choice for rest of this chapter.

6.3.2 Substrate Thickness

With the substrate material of tungsten being chosen, the corresponding thickness can be ascertained. The thickness required will have a neutron flux dependency, as CASPAs rely on adequate statistical information to discern between signal and contrast on the hologram. As it is a statistical process, there is only a minimum aperture thickness limit in order to decode the hologram into a reconstruction of the object. Thus, the CASPA should be designed for the highest incident energy neutron anticipated, and everything below that energy will still be imaged effectively. For fusion neutrons, the highest incident energy anticipated will be at 14.1 MeV from DT interactions, so the CASPA must be designed to work for those energies.

There is no quantifiable definition for when an object is being effectively or ineffectively imaged. It is subjective, depending on the outcomes required. In order to quantify effectiveness for imaging 14.1 MeV neutrons, Legendre mode fitting (as defined in section 6.2) of a known simulated source will be used. By generating the source from a Gaussian of known P_0, and comparing that to the P_0 from an analysed and decoded hologram.

The measurable neutron yield on NIF is between 10^{10} and 10^{19} across 4π radially from the capsule implosion[191], with yields of 10^{14}–10^{15} being typical for DT shots[192], and a current record of 4.8×10^{17} set on shot N210808[193]. A dataset of individual Geant4 simulations have been plotted in figure 6.4 for 4 different CASPA thicknesses, looking at the variation of post-

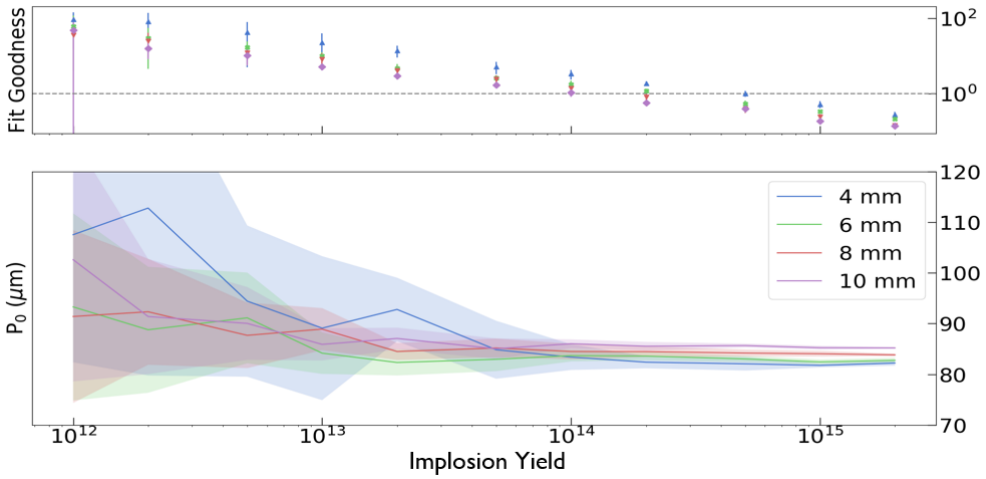

FIGURE 6.4. Benchmarking CASPA effectiveness at 4 different thicknesses for accurately imaging a $P_0 = 80$ μm Gaussian source as a function of neutron yield. Fit Goodness is from Legendre mode fitting, and error bars are either the standard deviation of 5 repeats or the diagnostic resolution, whichever is greater.

analysis P_0 for an input Gaussian of $P_0 = 80$ μm as a function of total experimental neutron yield. As the source is a known perfectly defined Gaussian, the analysis was constrained such that $P_n = 0$ for $n > 0$, and the fit goodness used as a quantitative measure of imaging effectiveness.

The first result with a goodness of less than or equal to 1 is the 10 mm CASPA for a total implosion neutron yield of 1×10^{14}. As this falls within the aforementioned typical range, it is suggested that a 10 mm thick tungsten CASPA would be suitable for imaging DT fusion neutrons on NIF, with non-tapered features of 9.9 μm and a basic MURA pattern of $p97$. This is a twenty-fold decrease in thickness with respect to the 20 cm thick NIA. It is also worth noting that this does not include any use of maximum likelihood (ML) reconstruction techniques which are already heavily deployed when analysing NIF neutron data, so the fit goodness of figure 6.4 is the upper bound of usable results. Using ML, it is possible that a thinner CASPA could be used, or that the 10 mm aperture could be applied to lower source yields.

Manufacture and metrology of fusion neutron apertures is a costly endeavour, requiring specialist skill and machinery to accomplish. The apertures are too large, with too high an aspect ratio to machine from a solid bock of metal. Instead, they must be made in smaller, more manageable sheets and assembled. These sheets can either be along the collimation axis, or perpendicular to it.

The NIA takes the approach along the collimator axis. The triangular pinholes are etched as grooves, and then stacked atop a non-etched sheet to form the perforation. This allows for fine control over taper features for the full length of the aperture, but limits the technique pinholes on rowed grids only. The separate sheets can be seen through discolouration in figure 6.1(b). Having

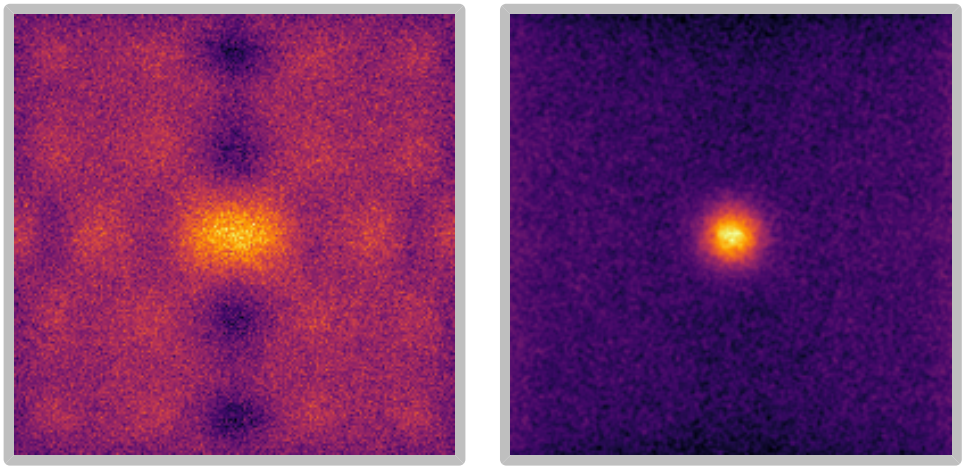

(a) (b)

FIGURE 6.5. The (a) hologram and (b) reconstructed image for the $p97$ 10 mm thick W CASPA, with a source yield of 10^{14} neutrons from a P_0 = 80 µm Gaussian distribution.

a defined metrology for the aperture is paramount for maximum likelihood reconstruction of the experimental images (discussed later in section 6.4), which is a difficult task for such high aspect ratio tapered features.

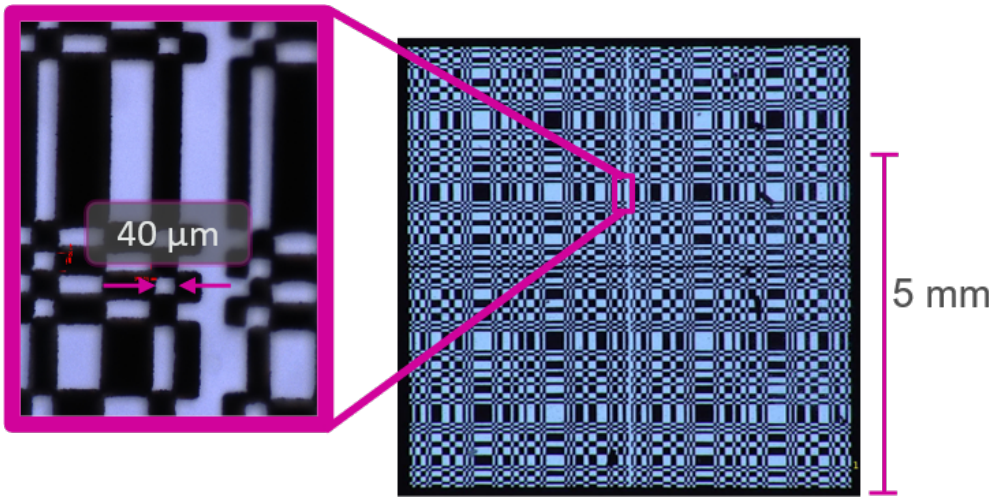

FIGURE 6.6. The first manufactured CASPA, by Scitech Precision. A $p53$ MURA, with a 100 µm tungsten substrate, designed with an A_{pix} = 52 µm and 7 µm corner rounding to make the aperture self-supporting. The measured feature size of 40 µm is displayed on the figure. Image courtesy of Scitech Precision with an optical microscope.

The substantial reduction in aperture thickness for the CASPA reduces the collimator effect,

and each individual perforation has a larger field of view without the need to taper. This allows for stacks perpendicular to the collimation axis to be used, and with each sheet in the stack being identical to one another, and thus can be manufactured in batch. This is not viable for tapered features, as notches or imperfections along the taper would be detrimental to imaging quality and effectiveness.

This stacking approach would allow different manufacturing techniques to be used on thinner sheets in batch, which are more common in micromachining. Thus, even though the challenges in manufacture will be different, they have been investigated by industry more readily. This should reduce the manufacturing cost of a CAPSA with respect to the NIA, both in terms of specialist labour hours and cost of raw materials. Furthermore, because laser micromachining and lithography techniques are more readily applied to thin sheets, there is potential to manufacture a CASPA with a smaller A_{pix} to enable higher-resolution imaging, as discussed previously. Laser machining has already been used by Scitech Precision to manufacture a 250 µm thick CASPA with *ca.* 48 µm A_{pix}, as shown in figure 6.6. It is noted that alignment of the separate sheets in the stack would be a complex micromachining task, and metroloy of every single perforation may be impractical.

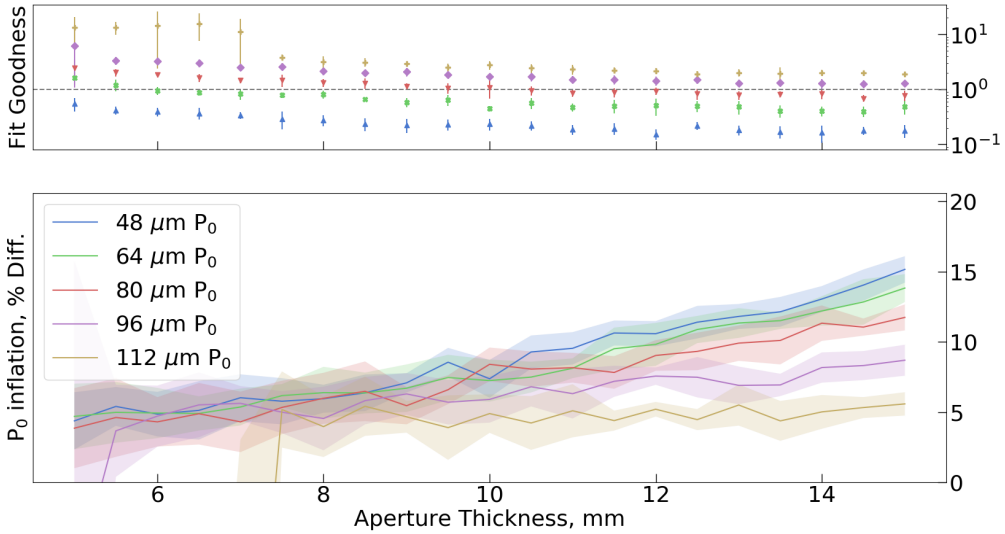

FIGURE 6.7. The error in P_0 measurement from a known source, as a function of aperture thickness. Results all use a consistent neutron yield of $\times 10^{14}$. For large P_0 and thin aperture, the Gaussian was too degraded to adequately analyse. Fit Goodness is from Legendre mode fitting, and error bars are the standard deviation of 5 repeats.

Despite the 10 mm tungsten aperture having the desired goodness in figure 6.4 and converging, the result of 85.7 ± 2.5 µm falls outside the range for the P_0 of 80 µm input source. Furthermore, a trend is apparent across the four aperture thicknesses tested, with the thinner apertures

converging closer to the input parameters than their thicker counterparts. This is highlighted further in figure 6.7, highlighting the percentage difference between recorded P_0 and input P_0 for different aperture thicknesses, as well as for different source sizes. It can be seen that there are correlations with both parameters, and as such either correction factors, iterative reconstruction methods, or both need to be used in order for input and outputs to align.

6.4 Hologram Compensation

The decoding process outlined in section 2.3.3 models the aperture plane and detector plane as a two dimensional, allowing them to be easily defined in a matrix. As the aspect ratio increases, and sources are close enough to the aperture to have a non-zero divergence, the point spread function (PSF) used to generate the decoding function is unlikely to be the binary aperture design. Instead, either the decoding function or hologram need to be corrected for the change in PSF. In literature, Mu & Liu[120] suggest an aspect ratio correction, as well as a maximum likelihood expectation-maximization algorithm to more accurately reconstruct the object. Henceforth, ϕ will be used to describe the angle of incidence of a single particle from the source onto the aperture, and using the naming convention of the front and back of the aperture being the source-facing and detector-facing surfaces respectively.

6.4.1 Aspect Ratio

The collimator effect can cause the effective imaging diameter of a pinhole to vary as a function of ϕ. Working under assumption that the substrate is an effective attenuator of incident particles, for any known point source position the amount of signal reduction on the detector due to the collimator effect of the aperture can be calculated with simple geometry; project the perforation from the front to the back surface of the aperture, and calculate the overlapping area of this projection with the exit of the perforation. The fraction of this overlapping area with respect to the total perforation area can then be used as a correction factor, C, for the collimator effect.

ϕ is a function of the vector between source position and detector pixel position on their respective planes ($\boldsymbol{s}$ and $\boldsymbol{d}$ respectively). In turn, C is a function of ϕ, substrate thickness, t, perforation radius, r, and the distance between the source and detector planes, z where $z = u + v$ (from figure 4.3).

However, requiring to know the source position before imaging, in order to compensate said imaging system, is a fatal flaw. Instead, a correction is required that is only a function of detector pixel and aperture design, and thus independent of source position. The literature achieves this with three key assumptions[120] which will be discussed in sequence:

1. A homogeneous source
2. An aperture of uniform perforation diameter
3. Large system magnification

By treating the source as homogeneous across its plane, the $\boldsymbol{s}$ dependence of $C(\phi)$ is removed, and the response looks akin to a PSF for the single perforation, showing its full field of view and the signal drop-off as a function of ϕ.

Then, using the no-two-holes-touching approach outlined by Fenimore and Cannon[194] for aperture construction, the perforation diameter stays constant across the entire aperture. This allows $C(\phi)$ to be calculated once for a homogeneous source place, and then extrapolated to the entire aperture correction, $\overline{C}$:

$$\overline{C}_{\boldsymbol{d}}(t,z,r) = \sum_{\boldsymbol{d}} A_{\boldsymbol{d}+\boldsymbol{a}-\boldsymbol{s}}\ C_{\boldsymbol{d}-\boldsymbol{s}}(t,z,r) \tag{6.7}$$

Assumptions 1 & 2 remove the necessity of knowing source distribution pre-imaging, however it does require knowing where the source plane is - or rather, picking a source plane before imaging. This is akin to calculating the focal plane for a lens based system, but removes a powerful capability of coded apertures to adjust focal plane in post processing. Instead, by assuming a large system magnification, $u << v$, and therefore $z \simeq v$, as well as $\boldsymbol{s} \simeq \boldsymbol{a}$. Thus, ϕ can be calculated as a function of $\boldsymbol{d}$ alone, and $\overline{C}$ can be calculated as:

$$\begin{aligned} \overline{C}_{\boldsymbol{d}}(t,v,r) &= \sum_{\boldsymbol{d}} A_{\boldsymbol{d}}\ C_{\boldsymbol{d}-\boldsymbol{a}}(t,v,r) \\ &= A \star C(t,v,r) \end{aligned} \tag{6.8}$$

The corrections were originally discussed in the context of single photon emission computerised tomography (SPECT) using circular pinholes on the no-two-holes-touching aperture. This can be extrapolated using the logic discussed above to work with the square, multi-sized pinholes used in the MURA apertures of this work.

Mu and Liu[120] use cylindrical coordinates to calculate C and ϕ, due to their the symmetry about a circular pinhole of constant diameter. For the square pinholes used here, a cartesian coordinate system is better suited. Furthermore, while not using the no-two-holes-touching approach to aperture design, there will be a variety of perforation sizes across the aperture. Thus, $\overline{C}$ becomes:

$$\overline{C}_{\boldsymbol{d}}(t,v,r) = \sum_{r_x,r_y} \frac{1}{n} A \star C(t,v,r) \tag{6.9}$$

where n is a normalisation term - the total perforation area divided by the fraction of perforations with size d out of the total number of perforations.

However, in applying the collimator correction in figure 6.8, it can be seen that the correction is detrimental to the imaging results, with the hologram and reconstruction being dominated by the correction. Thus it can be concluded that the collimator effect is not the predominant mechanism of error within the encoding of the aperture pattern onto the hologram, and thus the error within image reconstruction.

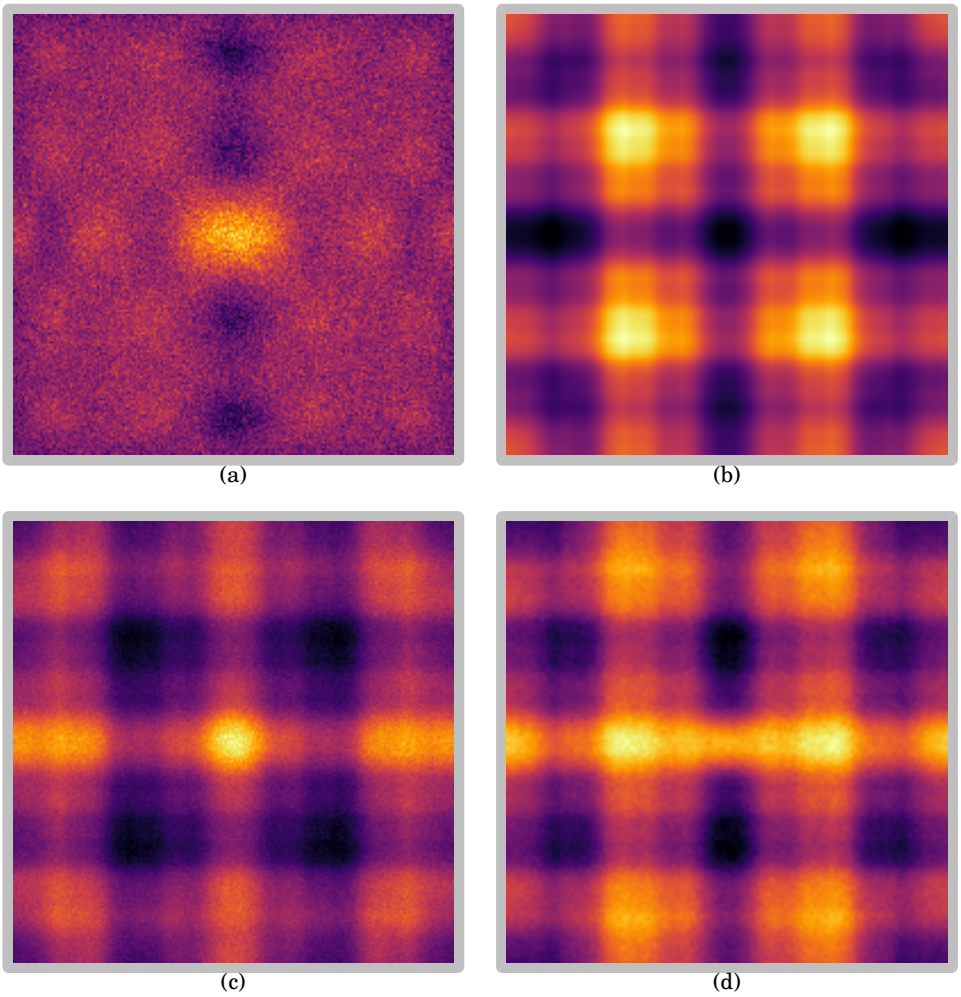

FIGURE 6.8. For the $p97$ aperture being discussed, (a) the original detector hologram is altered by (b) collimator correction from equation 6.9 to (c) the corrected hologram for collimator effects, and (d) the resulting reconstructed image.

The trend in error as a function of substrate thickness in figure 6.7 also has a correlation with source size. Smaller source sizes have a higher P_0 inflation than their larger counterparts, suggesting there is a scatter mechanism within the inflation - smaller sources having a larger ϕ.

Instead of taking Mu & Liu's homogeneous source model, the assumption of a point source is more applicable to NIF imaging due to the small implosion size with respect to the field of view. For a point source, ϕ will always be radial about the z axis, and will only increase ϕ for incidence on the detector for neutrons scattered through the substrate. This can be modelled as a correction to the detector hologram:

$$C(\phi) = \cos(n\phi) \tag{6.10}$$

where ϕ is calculated from the central axis of the source plane onto the detector, and the scatter

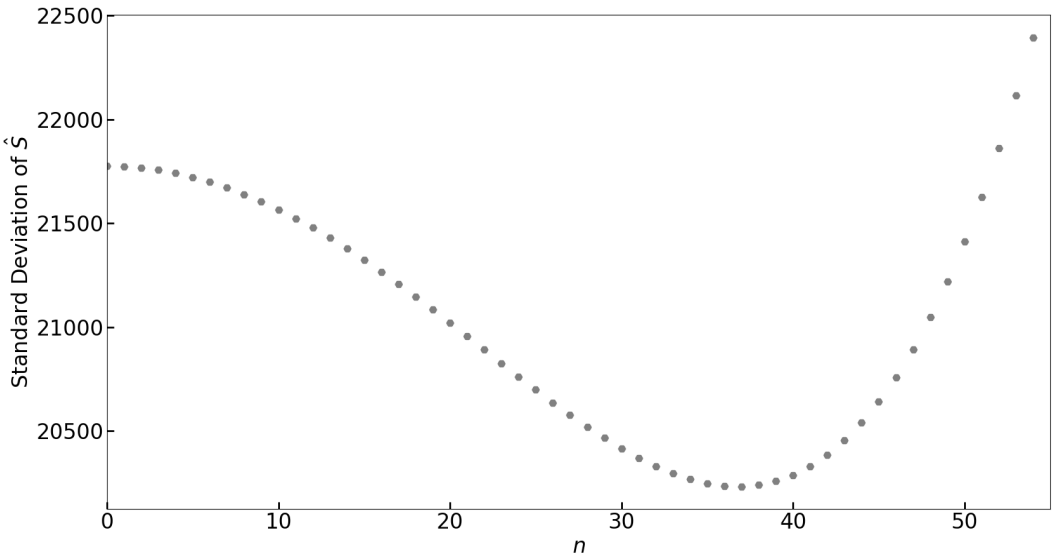

(a)

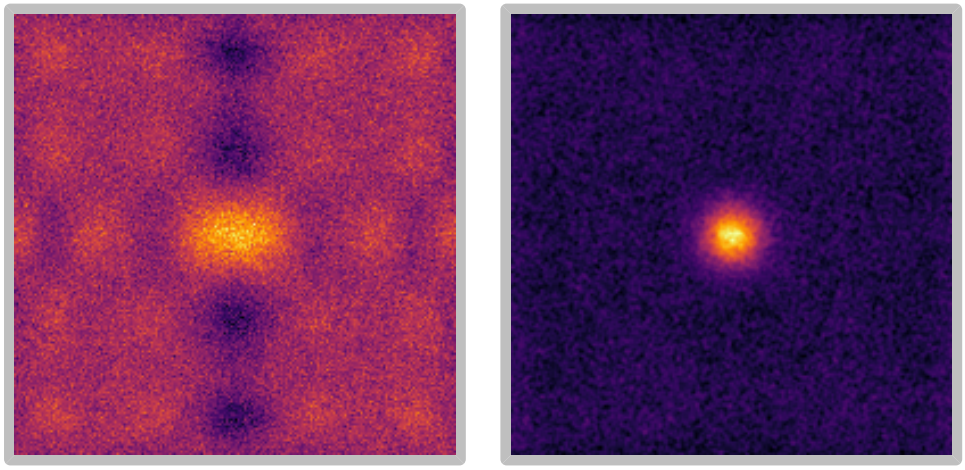

(b) (c)

FIGURE 6.9. (a) The variation in standard deviation across the reconstructed image as a function of n , where equation 6.10 is applied to the hologram pre-decoding. The minimum of the function, $n = 36.8$, had been applied to (b) the hologram, and decoded to produce (c) the source reconstruction.

modifier n will be a function of aperture thickness and source size. The role of this correction factor is to reduce the variation in background back to a quasi-uniform plane, which results in a constant background across the reconstructed image. Therefore, the standard deviation of $\hat{S}$ is a suitable figure of merit to analyse the effect of $C(n)$ on decoded image background levels, which can be seen in figure 6.9(a). By finding the minima of the function within the graph, a suitable n can be inferred for the specific substrate thickness and source yield - in this case the 10 mm W and 10^{14} neutrons, with an optimal n of 36.8.

Although visual comparison of the holograms of figure 6.5 and 6.9 shows little variation, the decoded images have noticeable changes in background. The higher than average background counts to the left and right of figure 6.5(b) are no longer present in the post-scatter corrected $\hat{S}$, and neither are the lower than average counts to the top and bottom. This suggests the scatter mechanism of equation 6.10 is a larger source of error on hologram encoding than the collimator effect of equation 6.9.

6.5 Reconstructed Image Correction

Although the scatter correction of equation 6.10 has reduced deviation in the image background, there is more background variation than the mathematically perfect Gaussian input source. This is a common issue with ICF experiments, with current NIF experiments requiring computationally heavy post-processing in order to iteratively reconstruct the most likely source from the imaged DT neutron data[102,181–183], an example of which has been shown in figure 6.10 to highlight the change in data quality before and after an iterative reconstruction method has been applied.

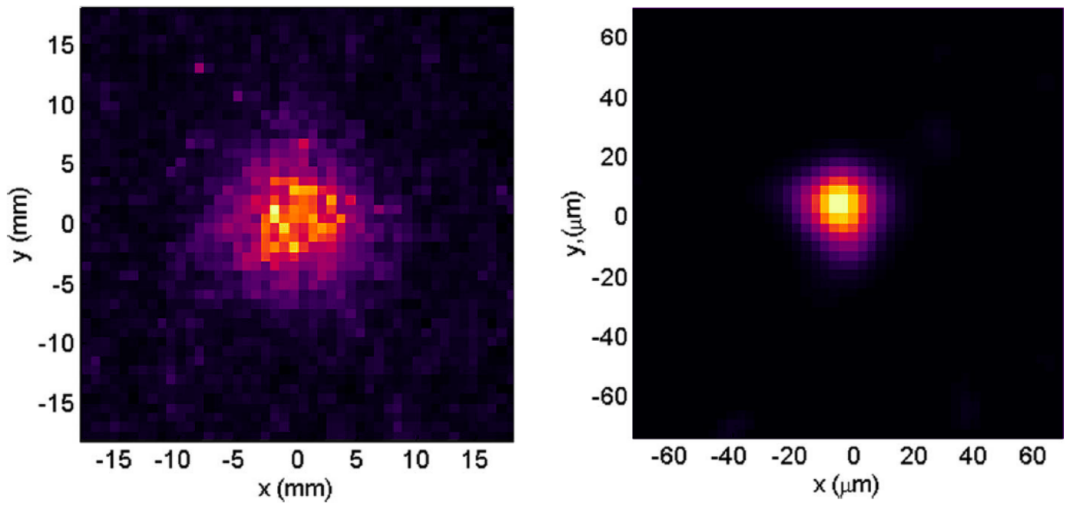

(a) (b)

FIGURE 6.10. The (a) captured detector image and (b) reconstructed image from the "best pointed" perforation of the NIS on NIF shot N120412-001. Figure reproduced from literature[102].

Pinhole imaging of mono-energetic sources can also be described as:

$$D = \int_{\boldsymbol{s}} K_{\boldsymbol{d}-\boldsymbol{s}} S_{\boldsymbol{s}} \tag{6.11}$$

where K is the kernel which describes the PSF for both the aperture and the detector. The former is dependent on the aperture perforation shape, axial profile, substrate thickness and source

shape, while the latter is often modelled as a Gaussian blur[183]. In an ideal case, K is a δ function for the image formed on D to perfectly image the source. In order to de-couple K from S, the source position must be known, which as discussed previously is not a useful requirement for an imaging system. Instead, an iterative reconstruction method is required to step-wise converge towards the most likely S that would produce the signal collected on D.

Iterative reconstruction is able to generate estimates for S to a greater resolution than attainable by the imaging system[181], as well as estimates with reduced noise. Due to the high noise on the CASPA images, the resolution increase application is not currently being considered here as the noise reduction is more pressing.

6.5.1 Maximum-Likelihood Expectation-Maximization: Poisson

Analysis of NIF shots using maximum-likelihood reconstruction, and modelling the noise as a Poisson distribution (expectation-maximization, MLEM). This is an iterative "forwards-backwards" technique, based on the comparison between the current iteration (forward projection) and the original (backward projection) in order to converge on the most likely source distribution. It is worth noting that other models can be used, with a Gaussian noise approximation being the principal amongst them. However, the Gaussian model allows for negative values in the reconstruction, which is unphysical for am imaging system and can cause erroneous reconstructions[183].

The following definition for the MLEM is often attributed to M. Z. Tarasko[195], and is discussed in English within the literature[181,183]. For the sake of the following equations, S, K and D are considered to be normalised such that their summation is unity:

$$S_{\boldsymbol{s}}^{t+1} = S_{\boldsymbol{s}}^{t} \left(\sum_{\boldsymbol{d}} K_{\boldsymbol{s},\boldsymbol{d}} \frac{D_{\boldsymbol{d}}}{\sum_{\boldsymbol{s}} K_{\boldsymbol{s},\boldsymbol{d}}\, S_{\boldsymbol{s}}^{t}} \right) \tag{6.12}$$

The MLEM algorithm constrains all of S, K and D to be positive integers, and will never produce S^{t+1} estimates with negative values. This is well suited to image reconstruction, where negative counts on a pixelated detector are not experimentally feasible.

For iterative solutions such as equation 6.12, the model will converge upon a reconstruction of the source, and if left unconstrained will run to infinitum. Instead, a stopping parameter is required when S^{t+1} is consistent with S^0 to within the experimental accuracy of the acquired data. Statistically, this is best expressed through a normalised χ^2 factor and its variance. Much akin to fit goodness, a χ^2 of 1 is desirable for a reconstruction with a high likelihood of being a good representation of the source. A $\chi^2 << 1$ would be resultant from a high noise in the reconstruction, while a $\chi^2 >> 1$ would suggest a poor reconstruction of the source[183].

However, this requires knowledge of the expected background on the image, which is often not known. Instead, an approximation for the stopping parameter can be the Kullback-Leibler divergence:

$$\begin{aligned}\Delta\rho &= \frac{\rho^t - \rho^{t+1}}{\rho^t} \\ \rho^t &= \sum_{\boldsymbol{d}} D_{\boldsymbol{d}} \ln\left(\frac{D_{\boldsymbol{d}}}{\sum_{\boldsymbol{s}} K_{\boldsymbol{s},\boldsymbol{d}}\, S^t_{\boldsymbol{s}}}\right)\end{aligned} \tag{6.13}$$

where stopping of 10^{-3} was found empirically to be a suitable critical value for the use on current NIF data. For any iterative method, initial conditions are required from which to begin. This is often a uniform array normalised to unity, but could reflect the expected source in order to reduce the number of iterations required - for instance defining S^0 as a centred circle with a radius of that expected from an implosion.

The MLEM approach outlined, with a uniform S^0 has been used for many NIF data shots[183], and works well for the triangular pinholes of figure 6.1(b). Although it is not an issue for the slow repetition rate of NIF shots and neutron experiments, one limitation for its more ubiquitous use for other ICF fusion devices is the speed of the algorithm. Volegov *et al.* state that for a 100×100 pixel detector image, the K array is of the order of $10^4 \times 10^4$.

Coded apertures differ from pinhole arrays by the virtue that they already consider a K-like array in the decoding process. For an infinitesimally thin completely attenuating coded apertures, the PSF is the aperture design and intrinsically linked to the decoding function. By taking the collimator effect and near-field imaging approximations into account, the K array for a coded aperture can be defined as:

$$\begin{aligned}K_{\boldsymbol{s},\boldsymbol{d}} &= A_{(\boldsymbol{d}-\boldsymbol{s})}\; C_{\boldsymbol{d}}(t,v,r)\; \cos^3\phi \\ &= A_{(\boldsymbol{d}-\boldsymbol{s})} \text{ when } D_{\boldsymbol{d}} \text{ is adjusted for } C(\phi)\end{aligned} \tag{6.14}$$

Through substitution into equation 6.12, this becomes:

$$S^{t+1}_{\boldsymbol{s}} = S^t_{\boldsymbol{s}} \left(\sum_{\boldsymbol{d}} A_{\boldsymbol{d}-\boldsymbol{s}} \frac{D_{\boldsymbol{d}}}{\sum_{\boldsymbol{s}} A_{\boldsymbol{d}-\boldsymbol{s}}\, S^t_{\boldsymbol{s}}}\right) \tag{6.15}$$

which, through substitution of definitions for cross correlation and convolution becomes the equation defined by Mu & Liu[120]:

$$S^{t+1} = S^t \left(A \star \frac{D}{A * S^t}\right) \tag{6.16}$$

Evaluating the efficiency of this MLEM expression has first been computed with a perfect Gaussian of $P_0 = 80$ µm with the addition of randomised noise with a maximum magnitude of 10% with respect to the Gaussian peak. The hologram is then calculated mathematically for a thin and attenuating coded aperture through deconvolution. This is due to the approximations

changing from the original SPECT imaging constraints for which the equation was published, and the point source approximation being more appropriate for the Gaussian profile imaging than the homogeneous one.

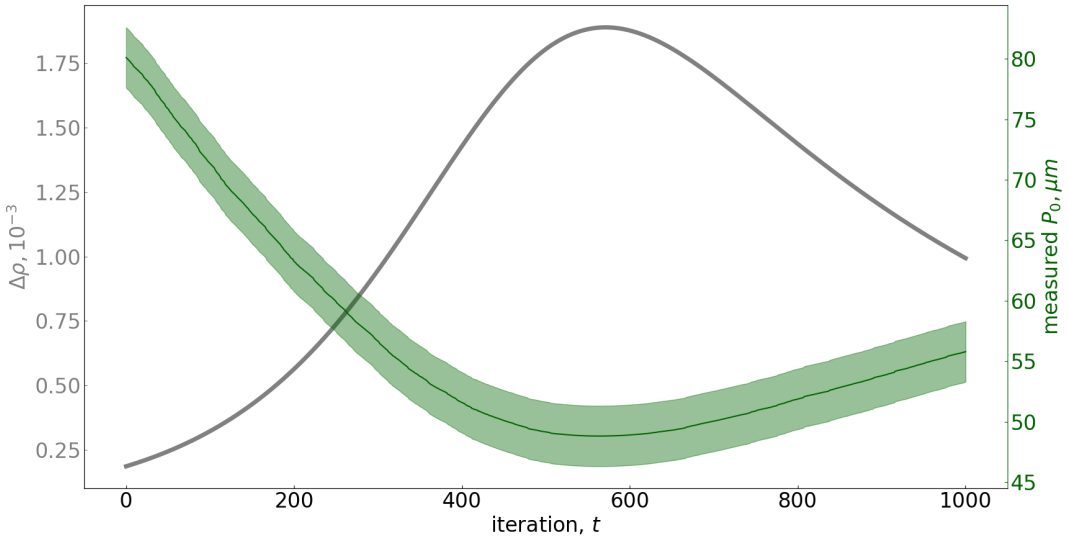

FIGURE 6.11. The variation of $\Delta\rho$ (equation 6.13) and analysed P_0 as a function of iteration number (equation 6.16). The source reconstruction of original noisy image is modified as a function of t, with a P_0 minimum at $t = 576$.

The variation in $\Delta\rho$ and P_0 can be seen as a function of t in figure 6.11. The magnitude of $\Delta\rho$ shows how slow-moving equation 6.16 is - the expected trend is a sharp increase followed by a decrease tending towards 0, while the figure shows it 576 iterations before this decrease begins. During this time, despite the noise signal being removed, the P_0 has shrunk considerably from its initial 80 ± 2.5 µm down to nearly half its expected value at 47.5 ± 2.5 µm, which is not representative of the known source. Although P_0 does increase again, over the 1000 iterations it only reaches 55.8 ± 2.5 µm.

Due to the low magnitude of $\Delta\rho$ while $P_0 \neq 80$ µm, it can be concluded that a different stopping parameter will be required than that suggested by Volegov. Stopping parameters are unique to the application, and will be considered secondary to the goal of having P_0 converge on the expected value.

6.5.2 Maximum-Likelihood Expectation-Maximization: Gaussian

Figure 6.11 does clearly show that a faster algorithm is required that does not take as many iterations to converge. The addition of a non-unity step size, h, can be introduced to speed up slower converging images[181]:

$$S_{\boldsymbol{s}}^{t+1} = S_{\boldsymbol{s}}^{t}\left(1 + h\left[\sum_{\boldsymbol{d}} A_{\boldsymbol{d}-\boldsymbol{s}} \frac{D_{\boldsymbol{d}} - \sum_{\boldsymbol{s}} A_{\boldsymbol{d}-\boldsymbol{s}}\, S_{\boldsymbol{s}}^{t}}{\sigma_{\boldsymbol{d}}^{2}}\right]\right) \tag{6.17}$$

where σ is the estimation for the variance of the noise. This algorithm assumes a Gaussian noise profile, and will hence be referred to as MLGAUSS. The MLGAUSS is more versatile in application than MLEM, as it is capable of handling negative values in its reconstruction. However, this is undesirable for image reconstruction, and the parameters h and σ must be constrained to prevent unphysical negative growth in S. It is worth noting that the Poisson noise model can be incorporated into the MLGAUSS algorithm, by taking σ^2 to be the mean of the signal in a single pixel, or:

$$\sigma^2 = \sum_{\boldsymbol{s}} A_{\boldsymbol{d}-\boldsymbol{s}}\, S_{\boldsymbol{s}}^{t} \tag{6.18}$$

which can then be substituted into equation 6.17 to yield:

$$\begin{aligned} S_{\boldsymbol{s}}^{t+1} &= S_{\boldsymbol{s}}^{t}\left(1 + h\left[\sum_{\boldsymbol{d}} A_{\boldsymbol{d}-\boldsymbol{s}} \frac{D_{\boldsymbol{d}}}{\sum_{\boldsymbol{s}} A_{\boldsymbol{d}-\boldsymbol{s}}\, S_{\boldsymbol{s}}^{t}} - 1\right]\right) \\ &= S^{t}\left(1 + h\left[A \star \frac{D}{A * S^{t}} - 1\right]\right) \end{aligned} \tag{6.19}$$

Literature suggests than an optimum h can be calculated[181,183], given a suitable model for the background variance is known. However, these calculations do not bind h such that $S \geq 0$. Instead, an empirical approach is used here, finding $h = 200$ suitable to speed up the algorithm without adding negative values to S.

The results from algorithm 6.19 can be seen in figure 6.12, with the P_0 measurement converging within 50 iterations. However, the converged value of 76.1 ± 2.5 µm is not within error of the 80 µm input. A similar trend in P_0 occurs, with the Gaussian size reducing nearly two-fold as the background noise is removed, before the source size is converged upon. This correlates with $\Delta\rho$, where the respective minima and maxima both occur at $t = 4$.

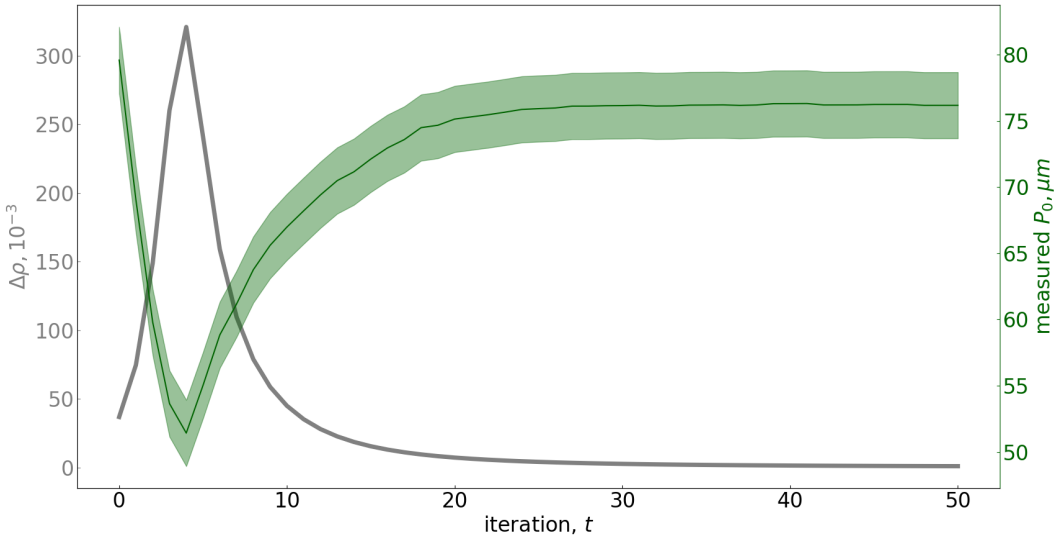

(a)

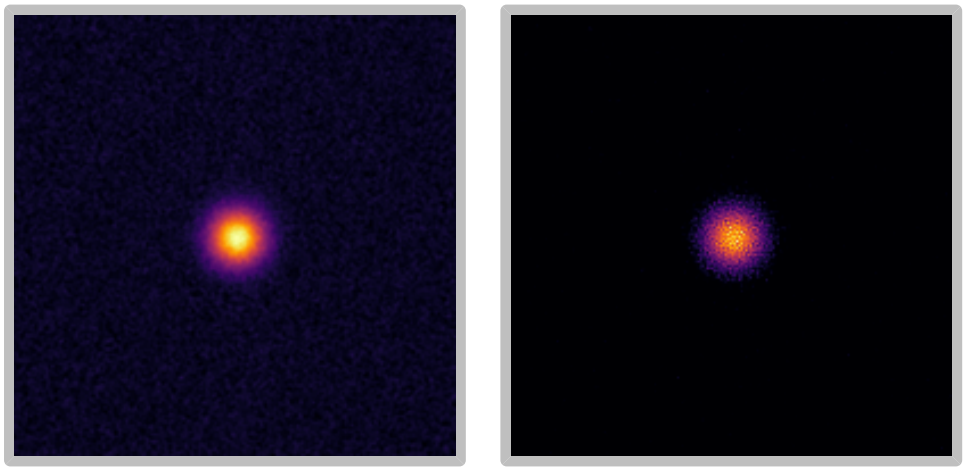

(b) (c)

FIGURE 6.12. The implementation of equation 6.19 to speed up the MLEM algorithm with coded apertures. $h = 200$ was chosen empirically, with (a) the variation of $\Delta\rho$ and P_0 as a function ot t, (b) the original image and (c) the $t = 50$ reconstruction.

6.5.3 Maximum A Posteriori Expectation-Maximization

Upon visual inspection of the reconstructed image (figure 6.12(c)) shows a high level of noise within the reconstruction, with a noticeable variance pixel-to-pixel across what should be a smooth Gaussian profile. A similar trend is seen in SPECT image analysis, where MLEM reconstruction algorithms are known to inflate noise within objects when reconstructions are close to the measured noise profiles[196]. Instead, an alternative algorithm is required to prevent such noise in reconstructed imaged, that can be steered towards an expected outcome. This reconstruction approach is known as a maximum a posteriori expectation-maximization (MAPEM) or one-step

late algorithm[197]:

$$
\begin{aligned}
S_{\boldsymbol{s}}^{t+1} &= \frac{S_{\boldsymbol{s}}^{t}}{1+\beta\frac{d}{d\boldsymbol{s}}U_{\boldsymbol{s}}}\left(1+h\left[\sum_{\boldsymbol{d}}A_{\boldsymbol{d}-\boldsymbol{s}}\frac{D_{\boldsymbol{d}}}{\sum_{\boldsymbol{s}}A_{\boldsymbol{d}-\boldsymbol{s}}\,S_{\boldsymbol{s}}^{t}}-1\right]\right) \\
&= \frac{S_{\boldsymbol{s}}^{t}}{1+\beta\frac{d}{d\boldsymbol{s}}U_{\boldsymbol{s}}}\left(1+h\left[A\star\frac{D}{A*S^{t}}-1\right]\right)
\end{aligned}
\tag{6.20}
$$

where the prior term, $\beta\frac{d}{d\boldsymbol{s}}U_{\boldsymbol{s}}$ is the differential of the energy function, U. This requires known properties of the source prior to image reconstruction, which is why the MAPEM approach is often deemed less favourable than MLEM. However, the prior knowledge does not have to be vast - for the continuous source of an ICF implosion, the prior term can be used to constrain the equation to favour smoother reconstructions. That is, reduction in single pixel hotspots, and the build up of noise within the reconstruction as seen in figure 6.12(c). This prior is always true for fusion implosions and makes no assumptions on symmetry or size of the hotspot, so its versatility within the field of ICF is still vast and valid. Thus, we can define the differential of the energy function to be a smoothing operator:

$$
\frac{d}{d\boldsymbol{s}}U_{\boldsymbol{s}} = \begin{bmatrix} \frac{1}{\sqrt{2}} & 1 & \frac{1}{\sqrt{2}} \\ 1 & 0 & 1 \\ \frac{1}{\sqrt{2}} & 1 & \frac{1}{\sqrt{2}} \end{bmatrix}
\tag{6.21}
$$

based on the radial distance between a pixel and its neighbours. This can be extrapolated out to larger $n \times n$ arrays for any odd number. β is then used to regulate the importance of the prior, with $\beta = h$ being the chosen factor here.

The results of the MAPEM function can be seen in figure 6.13. Although there is a similar trend in $\Delta\rho$ to the MLEM of figure 6.12, the key difference is the P_0 now converges to the initial 80 µm within error, with $P_0 = 78.5 \pm 2.5$ µm for $t = 50$. Furthermore, the variance of reconstructed image 6.13(c) is lower than that of 6.12(c), being 0.306 ± 0.001 and 0.313 ± 0.001 respectively across 3 repeats. Visually, the effect of noise across the smoothness of the Gaussian has also been reduced using MAPEM over MLEM.

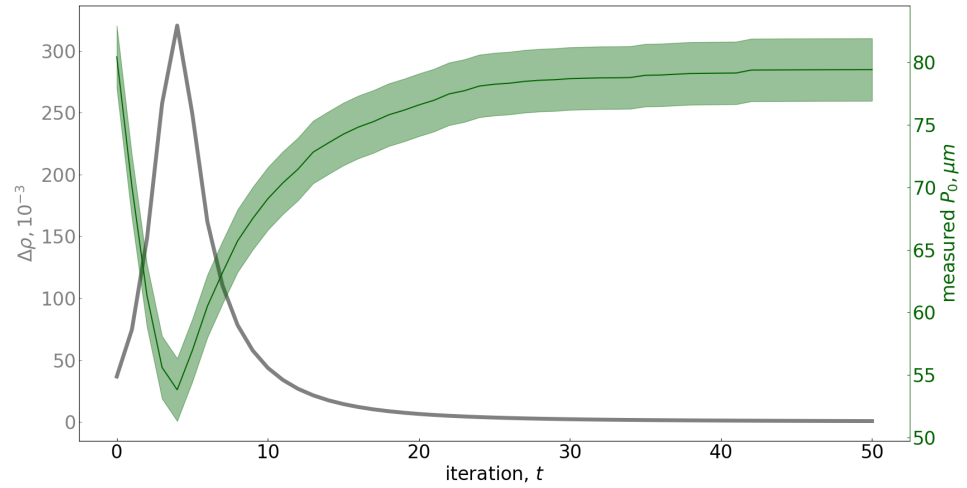

(a)

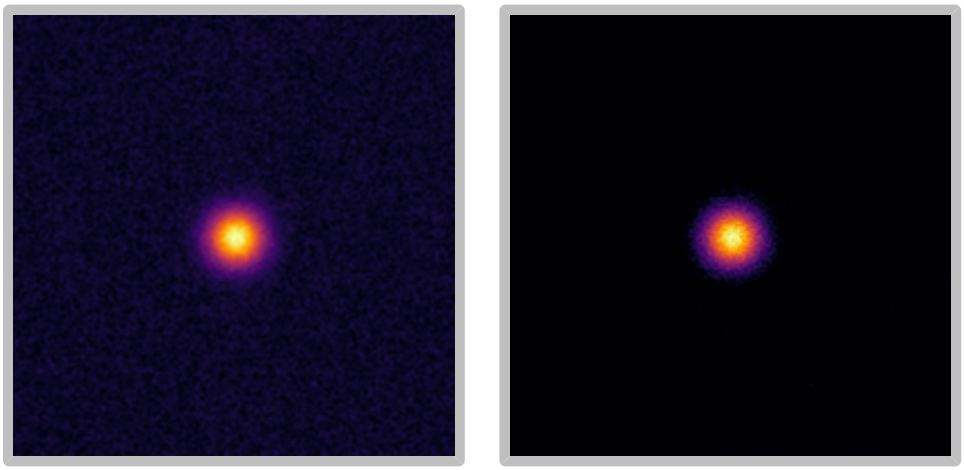

(b) (c)

FIGURE 6.13. Implementation of the MAPEM algorithm from equation 6.20 using $h = 200$ and a 5×5 kernel for $\frac{d}{d\boldsymbol{s}}U_{\boldsymbol{s}}$. (a) the variation of $\Delta\rho$ and P_0 as a function ot t, (b) the original image and (c) the $t = 50$ reconstruction.

6.5.4 Maximum A Posteriori Expectation-Maximization: using G

Despite the MAPEM algorithm producing the expected results of a smooth $P_0 = 80$ µm Gaussian, it may not be the most efficient for coded aperture use. $h = 1$ is standard for this technique, and thus a large h requirement is symptomatic of inefficiency within the process. This is largely down to the "forward" step of the cross correlation of A with the fractional difference between the original hologram and the reconstructed hologram. This step can be contextualised as converting a difference hologram from an encoded to decoded image, and the discussion between

autocorrelation and a unimodular decoding function G from chapter 2 can be applied:

$$\begin{aligned} S_{\boldsymbol{s}}^{t+1} &= \frac{S_{\boldsymbol{s}}^{t}}{1+\beta\frac{d}{d\boldsymbol{s}}U_{\boldsymbol{s}}}\left(1+h\left[\sum_{\boldsymbol{d}} G_{\boldsymbol{d}-\boldsymbol{s}}\frac{D_{\boldsymbol{d}}}{\sum_{\boldsymbol{s}} A_{\boldsymbol{d}-\boldsymbol{s}}\, S_{\boldsymbol{s}}^{t}}-1\right]\right) \\ &= \frac{S_{\boldsymbol{s}}^{t}}{1+\beta\frac{d}{d\boldsymbol{s}}U_{\boldsymbol{s}}}\left(1+h\left[G\star\frac{D}{A*S^{t}}-1\right]\right) \end{aligned} \tag{6.22}$$

By performing the cross correlation with G instead of A, the image contrast will be higher and therefore h need not be so high as the previous results shown here. Henceforth, this change to the algorithm will be called MAPGEM. However, the introduction of G does re-introduce the possibility for negative spirals in S, as anti-correlated holograms will result in negative values. As MLGAUSS and MAPEM are capable of handling negative values in reconstruction, but $S > 0$, h must therefore be bound once more to prevent unphysical negative growth in S.

Large changes to S^{t+1} from S have been observed to occasionally over-estimate the signal response, and result a system of over-under-estimation the alternates towards convergence in a saw-tooth-like function. Such a system still converges around the correct solution, but makes the stopping parameter more complex as $P_0^{t+1} - P_0^t \geq 7.5$ µm at $t \approx 50$ could be observed in some reconstruction. To prevent this, ΔS is bound such that:

$$\begin{aligned} \xi &= G\star\frac{D}{A*S^{t}}-1 \\ 0.9 &\leq (1+h\xi) \leq 2 \end{aligned} \tag{6.23}$$

Instead of using a constant h, this can be performed dynamically as a function of t. Ideally, h will be as large as possible without breaking the criterion of 6.23. However, large jumps in h was observed to cause erratic behaviour in reconstructions, so the change from h^t to h^{t+1} is limited to 5%. The dynamic h^t is calculated thus:

$$h^{t+1} = \min\begin{cases} -0.1/\xi_{\min} \\ 1/\xi_{\max} \\ 1.05\ h^{t} \end{cases} \tag{6.24}$$

with the expression designed such that h will steadily increase at a rate of 5% as long as $\xi_{\min}$ and $\xi_{\max}$ are still within the bounds of criterion 6.23.

Equation 6.24 is applied to $t \geq 1$. For $t = 0$, the criterion is expanded such that:

$$\begin{aligned} 0.1 &\leq \left(1+h^{0}\xi\right) \\ h^{0} &= -0.9/\xi_{\min} \end{aligned} \tag{6.25}$$

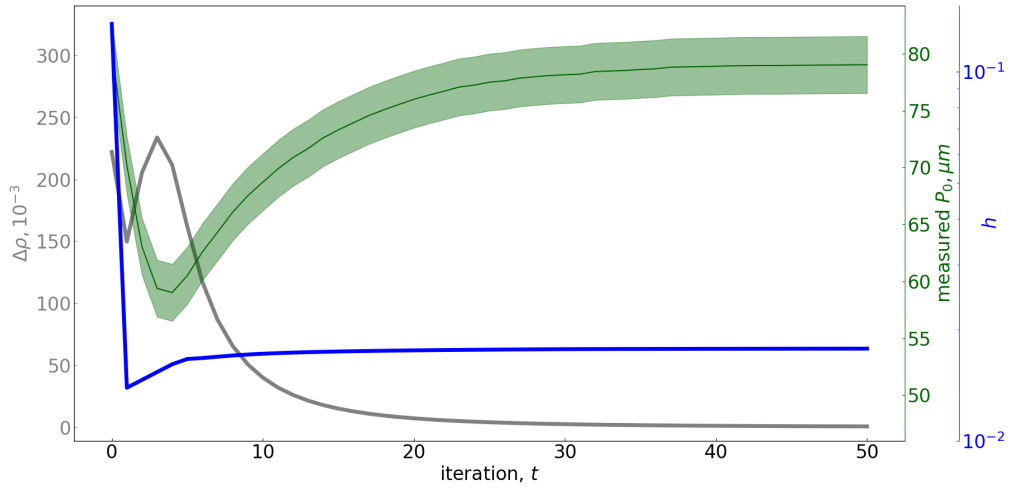

(a)

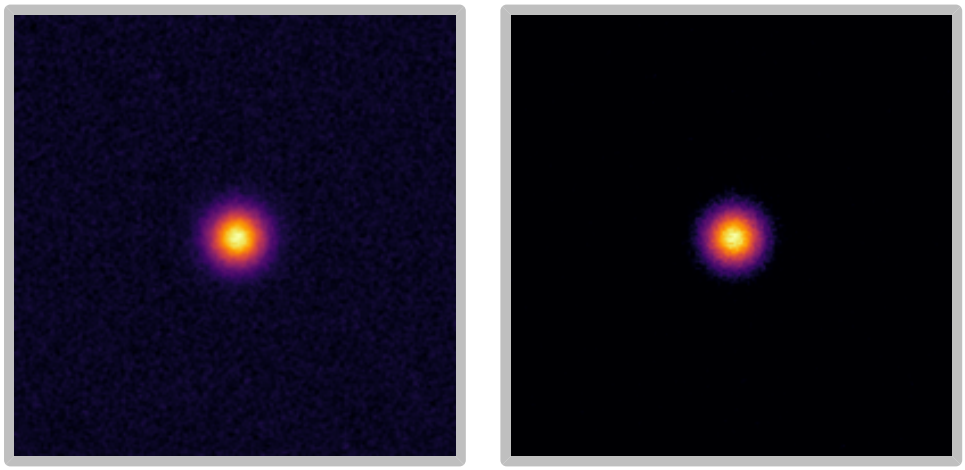

(b) (c)

FIGURE 6.14. Implementation of the MAPGEM algorithm from equation 6.22 using a dynamic h, a 5×5 kernel for $\frac{d}{d\boldsymbol{s}}U_{\boldsymbol{s}}$, $\beta = 200$, with h varying between 0.01 and 0.1. (a) the variation of $\Delta\rho$ and P_0 as a function ot t, (b) the original image and (c) the $t = 50$ reconstruction.

to speed up the early stage of the reconstruction. It is noted that this is a similar approach to adopting S^0 to be the initial source reconstruction, weighted to remove negative values.

The results from the MAPGEM algorithm can be seen in figure 6.14, using $\beta = 200$ to be comparable with figure 6.13. The MAPGEM algorithm yields a comparable result to MAPEM, with $P_0 = 79.2 \pm 2.5$ µm at $t = 50$. It is also worth noting that $\Delta\rho$ does not increase as high as the previous algorithms, and as such the P_0 minima is not as low - meaning that the algorithm does not walk as far away from the expected outcome before converging back towards it.

Thus, it has been shown that the MAPGEM algorithm is able to reconstruct Gaussian profiles accurately within 50 iterations, when the noise profile is independent of the aperture design.

6.6 NIF Simulation

The NIA has a maximum field of view of 700×500 µm, with each individual perforation only covering roughly 250×250 µm[102]. Due to this geometry, for a small source size expected from an ICF implosion on a NIF experiment not all of the perforations will be able to image the source completely, typically with only 4 or 5 or the total 20 perforations imaging an in-clipped source on any one shot. This makes target positioning and aperture pointing paramount in using this aperture to image the source. Due to the magnification and chamber size, this becomes an experimental challenge.

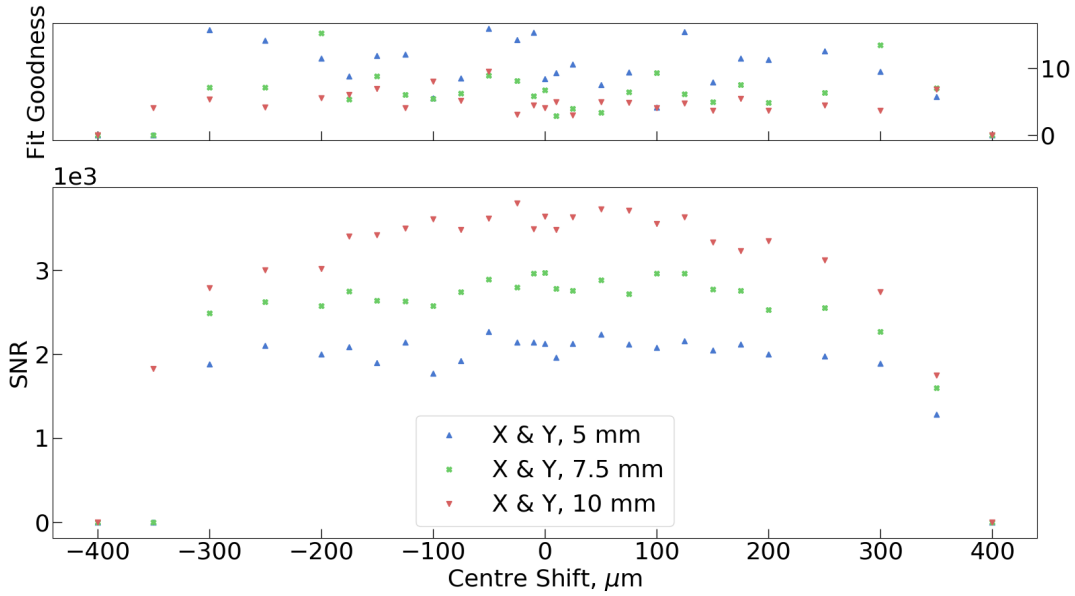

FIGURE 6.15. The field of view for the NIF experimental setup. A $P_0 = 80$ µm source with a yield of 10^{13} neutrons was moved across $x = y$, The CASPA and its SNR calculated to show the variation as a function of distance from the centre of the field of view.

The CASPA field of view is therefore of interest, both to ascertain the maximum object size attainable with the imaging system, as well as characterising the care required to axially align the source with the aperture centre. Figure 6.15 shows the variation in SNR as the source is translated across its plane in the $x = y$ direction, where the signal for the SNR calculation is defined as everything within the 17% contour of a Legendre mode fit. For the lower neutron yield, a field of view of 700×700 µm can be seen for the 10 mm aperture. However, the fit goodness shows the difficulty the Legendre fitting routine had characterising the 17% contour, so it is

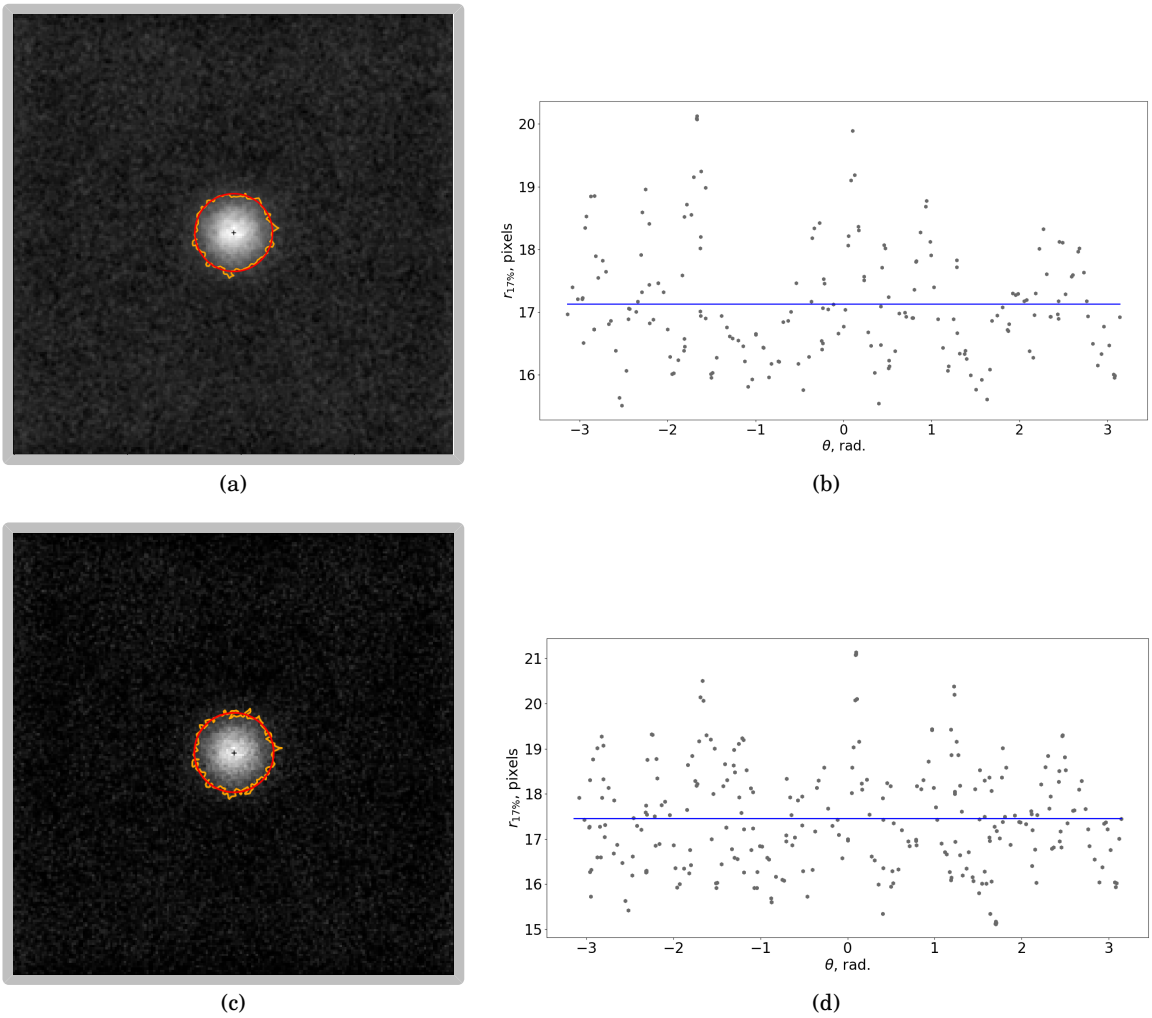

FIGURE 6.16. Applying th MAPGEM reconstruction algorithm to a 10 mm W CASPA Geant4 simulation with an implosion yield of 10^{14} neutrons. After the cos $n\phi$ has been applied, (a) is the $t = 0$ iteration with the 17% contour in yellow and the Legendre mode fit in red. (b) its Legendre fit in polar coordinates. (c) is the $t = 50$ iteration, and (d) its corresponding Legendre fit with a 9×9 density function and $\beta = 750$.

possible the total field of view will be larger when an iterative reconstruction routine is applied.

It is noted that a CASPA will not have the same field of view issue that the NIA does, where individual perforations can not all be used at the same time due to their limited individual field of view. As the substrate attenuation is low, the neutrons will penetrate through readily and pass through a fraction of the perforation volume, which will create contrast on the hologram with respect to neutrons that only pass through substrate This creates a low contrast image of the perforation on the hologram, which can then be decoded.

The MAPGEM algorithm can be applied to the a Geant4 simulation from figure 6.9, to

evaluate whether the noise profiles from the Geant4 simulations are independent of the aperture profile, with the results shown in figure 6.16. The pre-reconstruction ((a) & (b)) of $P_0 = 85.7$ µm and a fit goodness of 0.87 is lower than the $t = 50$ result of $P_0 = 87.3$ µm and a fit goodness of 1.40. This is despite the mean background being lower in (c) than (a).

The known source shape highlights the presence of background in the reintroduction, which the algorithm is unable to distinguish from signal and is actively attempting to reconstruct it. This proves a dependency of the background signal on the aperture design, and thus the Mu & Liu approximation of equation 6.14 cannot be applied in this context. Instead, the multi-dimensional K of Volegov is required, as well as a clearer defined PSF instead of assuming the two dimensional aperture design to be adequate. Due to the computational costs and resources required, these advancements will not be followed at this current time.

6.7 Conclusion

In summary, we propose that a CASPA can be used for fusion neutron imaging on ICF facilities in order to have a cheaper aperture that is easier to align and has a larger field of view. We demonstrate a MAPGEM algorithm for coded aperture image construction using maximum likelihood principles with a varying step size in order to converge faster than current methods. For the case study of NIF, a 10 mm thick tungsten CASPA has been designed for the 11.5 m line of sight, and shown to be an adequate thickness. This corresponds to a 20 times reduction in substrate thickness with respect to the NIA.

Further research in this area should focus on the calculation of the PSF for CASPAs, and the required modification to the MAPGEM algorithm to reconstruct a noiseless Gaussian profile from the Geant4 simulation. Once completed, reconstruction to sub-detector resolution can be explored and experimental data from a NIF implosion used to evaluate the imaging capabilities of a CASPA against the current architecture for ICF implosion geometries.

CHAPTER 7

FURTHER WORK

The potential for this research is not limited to the results presented here. There are many applications for coded aperture imaging systems, and development can be made for specific applications. However, there are three overarching areas for immediate development; experimental results, manufacture feasibility study, and machine learning.

7.1 Experiments

The major impact of the COVID19 pandemic on this work has been the lack of experimental access. Facilities where coded apertures would have been tested - such as the Central Laser Facility at the Rutherford Appleton Laboratories - closed and were not running experiments. Despite having an aperture constructed and ready to use (see figure 6.6), it was not possible to take experimental data with the coded apertures to compliment the simulation results shown. Therefore, experimental results are a high priority for further work.

The aperture of figure 6.6 was designed for a silver K-edge source, and could be run on any experiment with a source *ca.* 10 keV to measure source size. The neutron work is unlikely to be used on NIF before being tested elsewhere, and as such experiments on Omega or the Z machine are more likely for initial neutron measurements.

7.2 Manufacture

Knowing the limitations on manufacture will be useful for designing future apertures, as the resolution is dependent on perforation size. A feasibility study into manufacturing techniques to create high aspect ratio coded apertures is suggested, looking at manufacture mechanisms such as laser machining or lithography and the tolerances they are able to produce.

Then, a study into the PSF for apertures can be conducted to evaluate how costly manufacturing imperfections could be to the decoding efficiency. Furthermore, a study into the structural integrity of a coded aperture with minimally rounded corners, and the PSF effect of rounded corners would aid in future designs for coded aperture based imaging systems.

A preliminary study was performed to look at decoding efficiency for a non-perfectly constructed coded aperture, with the results seen in figure 7.1. By altering the binary of the aperture construction from a 1 to a 0, or vice versa, the SNR of the PSF can be calculated when the decoding is done with and without knowledge of the imperfection locations.

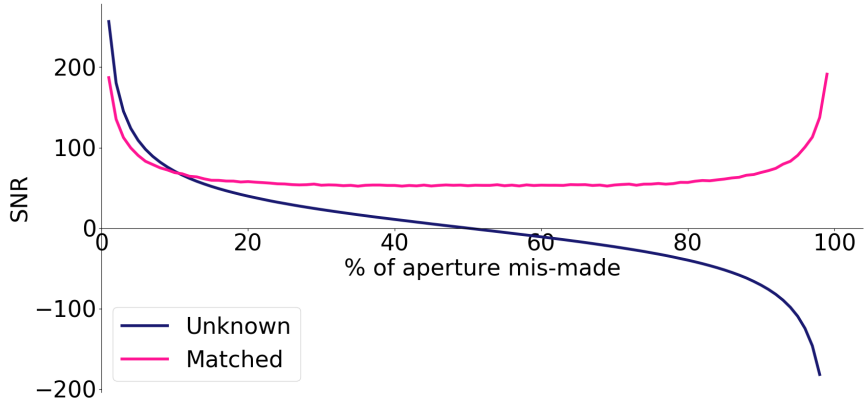

FIGURE 7.1. SNR as a function of aperture design defects, where (blue) the defects are not known and (pink) the defects are known and used to generate G.

7.3 Machine Learning

Machine learning is a powerful tool for solving problems previously deemed too complex or arduous to mathematically model, instead using an iterative model to tend to the solution.

For the work presented here, machine learning could improve the results for neutron imaging and the the BaSCA. The maximum likelihood reconstruction techniques will could be improved through calculation of a CASPA PSF, which could be constructed through machine learning instead of mathematical approximations or Monte-Carlo simulations. Furthermore, the impact of the BaSCA decoding noise could be negated by constructing an aperture and decoding function pair that create a delta function for each individual energy band, without using the same design in rotation. Such an aperture would need machine learning techniques to construct.

CHAPTER 8

CONCLUSION

In conclusion, novel approaches to high-energy high-resolution laboratory imaging have been explored using coded apertures. The published and known advantages of coded apertures are still relevant, with increased throughput with respect to a single pinhole aperture. This allows for high-resolution imaging through small perforation sizes without sacrificing signal strength to do so.

A new advantage of coded apertures has been presented here, demonstrating that coded apertures need not be fully attenuating to be able to reconstruct an image of the source. The CASPA showed that, through considerations of scatter and partial attenuation of a substrate material, source reconstruction is possible with highly transmissive substrates, as demonstrated through simulations of a space invader source emitting at 511 keV. With this example, a CASPA made from only 250 µm thick tungsten could be used where 18 mm of tungsten would previously be used to design single pinhole apertures. The processes used for scatter and partial attenuation are not key to the success of a CASPA, merely that the combination of the two creates adequate hologram contrast for clean decoding to occur. Therefore, the technique can be applied to image a range of particles over a broad range of high-energies, as demonstrated with 511 keV photons and 14.1 MeV neutrons.

Combining techniques used within Ross pair filtering with coded apertures, banded spectrally resolved imaging was discussed using a single non-spectrally resolving detector and an aperture of multiple combined NRAs. This is in contrast to filtered pinhole arrays commonly used, necessitating multiple or large detectors at significant expense. The BaSCA was shown to be able to resolve spectral bands, but decoding noise masked signal when using objects on the order or larger than the number of perforations within the NRA. In order for a BaSCA to be used for non-point sources, a new aperture and decoding function pair will be required - the construction

of which is most likely to be calculated through machine learning algorithms.

The CASPA was then discussed as a possible alternative to thick, expensive pinhole arrays used on ICF experiments such as NIF to image primary neutrons released from DT fusion reactions. NIF currently use a 20 cm thick gold aperture of 20 tapered triangular perforations, and simulations suggest that a CASPA of only 10 mm thick tungsten with un-tapered square perforations could be used instead. The iterative reconstruction methods from literature[120,183] are discussed and the theory updated for CASPA specific applications, showing that assumptions made by Mu and Liu [2006] break down for the CASPA. Although raw data looks comparable to that from NIF, further work is required on the CASPA reconstruction techniques before comparing the ability to resolve implosion asymmetries between the two systems. The use of such reconstruction techniques may allow for a thinner CASPA to be used, or for lower yield experiments to be imaged.

APPENDIX A

SYMBOLS & ABBREVIATIONS

A.1 Symbols

A	The array that defines the aperture pattern
$\boldsymbol{a}$	The $[n,m]$ coordinate system used on the aperture plane
$A_{\mathbf{pix}}$	The height and length of an aperture pixel, assumes square geometry
B	The array that defines the background on a hologram
D	The array that defines the detector hologram
D_v	The array that defines a virtual detector hologram
$D_{\mathbf{det}}$	The height and length of the entire detector, assumes square geometry
$D_{\mathbf{pix}}$	The height and length of a detector pixel, assumes square geometry
$\boldsymbol{d}$	The $[i,j]$ coordinate system used on the detector plane
G	The array that defines the decoding function
K	the array that defines the point spread function
M	Magnification of the system
p	The prime number, or square of a prime, used as a basis for aperture creation
R	Resolution capability, the number of resolvable sources per unit length
S	The array that defines the source
$\hat{S}$	The array that defines the reconstruction of the source
$\boldsymbol{s}$	The $[x,y]$ coordinate system of the source plane

A.2 Abbreviations

API	Application Program Interface
BaSCA	Banded spectral coded aperture
CAD	Computer aided design
CASPA	Coded aperture with scatter and partial attenuation
CCD	Charge coupled device
DD	A fusion fuel mix of deuterium with deuterium
DT	A fusion fuel mix of deuterium with tritium
FDR	Furtive to direct ratio
FFT	Fast Fourier transform
FWHM	Full width half maximum
ICF	Internally confined fusion
JEFF	Joint evaluated fission and fusion library
LWFA	Laser wakefield acceleration
MAPEM	Maximum a posteriori maximisation
MAPGEM	Maximum a posteriori maximisation using the decoding function
ML	Maximum likelihood
MLEM	Maximum likelihood expectation maximisation, using Poisson statistics for noise
MLGAUSS	Maximum likelihood expectation maximisation, using Gaussian statistics for noise
MURA	Modified uniformly redundant array
NIA	Neutron imaging aperture, currently used on NIF
NIF	National ignition facility, in Lawrence Livermore National Laboratory, USA
NIS	Neutron imaging system, a combination of the NIA and detector used at NIF
NRA	Non-redundant array
PET	Positron emission tomography
PRNG	Pseudo-random number generator
PSF	Point spread function
RAM	Random access memory
RNG	Random number generator
RTM	Ray trace model
SNR	Signal to noise ratio
SPECT	Single-photon emission computerised tomography
ToF	Time of Flight
URA	Uniformly redundant array

APPENDIX B

APPENDIX

B.1 Fusion 360 CAD API

```
#Author-M P Selwood
# Description-A script to make the coded apertures, with standard pinhole features
# p value, pixel size and thickness can all be altered
# *** FUCTION setVariables IS THE ONLY ONE THAT NEEDS TO BE CHANGED
# A boarder, 1 pixel large, is put around the edge

# v.1 - first attempt, with square pinholes
# v.2 - rounded corners, but only where they need to be rounded to prevent floating points
# v.3 - make nxn boxes a single sketch, instead of grouping single pixels
# distances are all in cm, E-4 converts to microns

import adsk.core, adsk.fusion, adsk.cam, traceback

def setVariables(ui, design):
  p = 5
  # distances are all in cm, E-4 converts to microns
  roundOff = 7
  gridSpace = "54 micron"
  thickness = "250 micron"
  #assign variables from text box UI
  p         = ui.inputBox('Enter {}'.format("p value"), '{}'.format("p value"), '5')[0]
  gridSpace = userInput(ui, design, gridSpace, "pixel size")
  roundOff = ui.inputBox('Enter {}'.format("Corner Rounding (microns)"), '{}'.format("
      Corner Rounding (microns)"), '7')[0]
  thickness = userInput(ui, design, thickness, "thickness" )
  roundOff = float(roundOff) * 1E-4
```

```
26    # convert cm to microms
27    # return variables
28    return int(p), gridSpace, roundOff, thickness
29
30  def userInput(ui, design, var, name):
31    input = var
32    createInput = ui.inputBox('Enter {}'.format(name), '{}'.format(name), input)
33    if createInput[0]:
34    (input, isCancelled) = createInput
35    unitsMgr = design.unitsManager
36    realSteps = unitsMgr.evaluateExpression(input, unitsMgr.defaultLengthUnits)
37    return realSteps
38
39  def C(phi, p):
40  # Quadratic Residue Modulo
41  # same code as c++ counterpart
42    x = q = 0
43    QRM = False
44    for x in range(p):
45      q  = x**2 % p
46      if ( q == phi and q != 0):
47        QRM = True
48      if(QRM == True or x >= p):
49        break
50    if QRM == True:
51      return 1
52    else:
53      return -1
54
55  def makeAperture(p):
56  # create the array of the aperture
57  # basic pattern only
58  # same code as c++ counterpart
59    halfdim = (p - 1) / 2
60    iPost = jPost = 0
61    holes = [[-1 for i in range(p)] for j in range(p)]
62
63    for jPre in range(p):
64      if (jPre < halfdim):
65        jPost = halfdim + jPre + 1
66      else:
67        jPost = jPre - halfdim
68      jPre  = int(jPre)
69      jPost = int(jPost)
70
71      for iPre in range(p):
72        if (iPre < halfdim):
```

```
73          iPost = halfdim + iPre + 1
74        else:
75          iPost = iPre - halfdim
76        iPre  = int(iPre)
77        iPost = int(iPost)
78        # equation 13 from paper
79        if(iPost == 0):
80          holes[jPre][iPre] = 0
81        elif (jPost == 0 and iPost != 0 ):
82          holes[jPre][iPre] = 1
83        elif (C(iPost, p) * C(jPost, p) == 1 ):
84          holes[jPre][iPre] = 1
85        else:
86          holes[jPre][iPre] = 0
87    return holes
88
89  def mosaic(holes, p):
90  # create the mosaic pattern of the pinholes in the substrate
91  # code is exactly the same as c++ version
92    mosaic = [[-1 for i in range(2*p - 1)] for j in range(2*p - 1)]
93    halfdim = (p - 1) / 2
94    for jCoord in range( 2 * p - 1 ):
95      jRef = jCoord + halfdim + 1
96      while jRef >= p:
97        jRef -= p
98      for iCoord in range( 2* p - 1):
99        iRef = iCoord + halfdim + 1
100       while iRef >= p:
101         iRef -= p
102       iCoord = int(iCoord)
103       jCoord = int(jCoord)
104       iRef = int(iRef)
105       jRef = int(jRef)
106       mosaic[jCoord][iCoord] = holes[jRef][iRef]
107   return mosaic
108
109 def redefine_Points(refPattern, p, value = 1):
110 """
111 Converts the 2D array from simple 1 & 0, into a value from 0 - 16
112 Each value denotes a number of corners which need to be rounded in order
113 for the structure to be continuous, and thus exportable as a singular DXF
114 """
115   withRounds = [x[:] for x in refPattern]
116   for jCoord in range( len( refPattern[:][0] ) ):
117     jCoord = int(jCoord)
118     for iCoord in range( len( refPattern[0][:] ) ):
119       iCoord = int(iCoord)
```

```
120       if refPattern[jCoord][iCoord] == value:
121         withRounds[jCoord][iCoord] = calcCellVal(refPattern, iCoord, jCoord, value)
122   return withRounds
123
124 def printRound(point):
125 """
126 A function to convert the cell value into a corner index
127 """
128   export = ""
129
130   if point >= 2**3 + 1:
131     export += "d, "
132     point -= 2**3
133
134   if point >= 2**2 + 1:
135     export += "c, "
136     point -= 2**2
137
138   if point >= 2**1 + 1:
139     export += "b, "
140     point -= 2**1
141
142   if point >= 2**0 + 1:
143     export += "a "
144     point -= 2**0
145
146   if export == "":
147     export = "none"
148
149   return export
150
151 def calcCellVal(refPattern, iCoord, jCoord, value = 1):
152 """
153 Test to see if the cell requires rounded corners
154
155 4 corners have been denoted: a,b,c,d
156 a - top left
157 b - top right
158 c - bottom right
159 d - bottom left
160
161 The code evaluates the adjacent cell diagonally touching each corner.
162 If this cell is also a 1 (therefore a hole), it checks the other 2 adjacent cells
163 If these are 0 (substrate), the corner must be rounded in order to make 1 structure
164
165 The cell index is made such that value = a 2**0 + b 2**1 + c 2**2 + d 2**3 + 1
166 The +1 denotes that it is a hole, and differentiates it from the substrate value of 0
```

```
"""
  a = b = c = d = 0

  # corner a
  try:
    adjCorner = refPattern[jCoord - 1][iCoord + 1]
    adjCell_1 = refPattern[jCoord - 1][iCoord + 0]
    adjCell_2 = refPattern[jCoord - 0][iCoord + 1]

    if adjCorner == value and adjCell_1 != value and adjCell_2 != value:
      if (jCoord - 1) >= 0 and (iCoord + 1) < len(refPattern[:][0]):
        a = 1
  except:
    a = 0

  # corner b
  try:
    adjCorner = refPattern[jCoord - 1][iCoord - 1]
    adjCell_1 = refPattern[jCoord - 1][iCoord - 0]
    adjCell_2 = refPattern[jCoord - 0][iCoord - 1]

    if adjCorner == value and adjCell_1 != value and adjCell_2 != value:
      if (jCoord - 1) >= 0 and (iCoord - 1) >= 0:
        b = 1
  except:
    b = 0

  # corner c
  try:
    adjCorner = refPattern[jCoord + 1][iCoord - 1]
    adjCell_1 = refPattern[jCoord + 1][iCoord - 0]
    adjCell_2 = refPattern[jCoord + 0][iCoord - 1]

    if adjCorner == value and adjCell_1 != value and adjCell_2 != value:
      if (jCoord + 1) < len(refPattern[0][:]) and (iCoord - 1) >= 0:
        c = 1
  except:
    c = 0

  # corner d
  try:
    adjCorner = refPattern[jCoord + 1][iCoord + 1]
    adjCell_1 = refPattern[jCoord + 1][iCoord + 0]
    adjCell_2 = refPattern[jCoord + 0][iCoord + 1]

    if adjCorner == value and adjCell_1 != value and adjCell_2 != value:
      if (jCoord + 1) < len(refPattern[0][:]) and (iCoord + 1) < len(refPattern[:][0]):
```

```
214         d = 1
215     except:
216       d = 0
217
218     a *= 2**0
219     b *= 2**1
220     c *= 2**2
221     d *= 2**3
222
223     return a + b + c + d + 1
224
225 def makeBox(xPoint, yPoint, pixSize, boxX = 1, boxY = 1):
226 # make a pixel into the sketch parameters required to draw a box
227 # default box size is 1 pixel
228     xMid = xPoint * pixSize
229     yMid = yPoint * pixSize
230     xLen = (xPoint * pixSize) - (pixSize * boxX )/2
231     yLen = (yPoint * pixSize) - (pixSize * boxY )/2
232     return xMid, yMid, xLen, yLen
233
234 def makeList(array, value = 1):
235 # turn the 2D array into a list of holes, and zero centre
236 # LIST FORMAT: all in pixels
237 # 1. centre of box in I
238 # 2. length of box in I
239 # 3. centre of box in J
240 # 4. length of box in J
241 # 5. Value (rounded-ness)
242     list = []
243     halfLength = (len( array[:][1] ) - 1 ) / 2
244     # modify centre row & column first
245     # as this is *always* the same
246     # left side of centre
247     xCentre, xLength, yCentre, yLength = centreFinds(0 - halfLength, -1, 0, 0)
248     list.append( [ xCentre, xLength, yCentre, yLength, 1 ])
249     # right side of centre
250     xCentre, xLength, yCentre, yLength = centreFinds(1, len( array[:][1]) - halfLength - 1,
          0, 0)
251     list.append( [ xCentre, xLength, yCentre, yLength, 1 ])
252
253     # when cycling, skip the centre row / column from sweep
254     # but not from calculations
255     for jCoord in range( len( array[:][1] ) ):
256       jCoord = int(jCoord)
257       # skip the centre row
258       if jCoord == halfLength:
259         continue
```

```
260     for iCoord in range( len( array[1][:] ) ):
261       iCoord = int(iCoord)
262       # if it is a hole
263       if array[jCoord][iCoord] > 0:
264         array, iMax, jMax, value = testSurround(array, iCoord, jCoord)
265         iNorm, iLength, jNorm, jLength = centreFinds(iCoord, iMax, jCoord, jMax)
266         iTrans = iNorm - halfLength
267         jTrans = jNorm - halfLength
268         list.append([iTrans, iLength, jTrans, jLength, value ])
269   return list
270
271 def testSurround(array, i, j):
272 # test adjacent pixels, to see if it an be redefined as a larger box
273   iMin = iMax = i
274   jMin = jMax = j
275   it = 0 # iterator
276   value = 1 # for rounded corners. 1 denotes a hole
277   goX = True
278   goY = True
279   iFull = len( array[0][:] )
280   jFull = len( array[:][0] )
281   # continue looping until a non-hole is encountered, XY, X, and Y
282   while goX == True or goY == True:
283     it += 1
284     # test to see if x and y are still viable options
285     if (goX == True and goY == True and
286     j + it < jFull and i + it < iFull and
287     array[j + it][i + it] > 0 and
288     array[j + it][i + 0] > 0 and
289     array[j + 0][i + it] > 0):
290       # sqaure features
291       iMax += 1
292       jMax += 1
293       goX = True
294       goY = True
295       elif goY == True and j + it < jFull and array[j + it][i] > 0:
296         # rectangles in Y
297         jMax += 1
298         goX = False
299       elif goX == True and i + it < iFull and array[j][i + it] > 0:
300         # rectangles in X
301         iMax += 1
302         goY = False
303       else:
304         goX = goY = False
305
306   # remove points from future loops
```

```
307   for subJ in range(jMin, jMax + 1):
308     for subI in range(iMin, iMax + 1):
309       # for holes with rounded corners, add up to find
310       # new corner value
311       if array[subJ][subI] > 1:
312         value += array[subJ][subI] - 1
313       # remove used points
314       array[subJ][subI] = -1
315   return array, iMax, jMax, value
316 
317 def centreFinds(xMin, xMax, yMin, yMax):
318 # define the center and length of a box
319 # from pixel points
320   xLength = xMax - xMin
321   xCentre = xMin + 0.5 * xLength
322   yLength = yMax - yMin
323   yCentre = yMin + 0.5 * yLength
324   # make single element holes size 1
325   xLength += 1
326   yLength += 1
327   return xCentre, xLength, yCentre, yLength
328 
329 
330 def sketchHole(hole, pixSize, roundOff, profileCollection, sketchCollection):
331 """
332 #Remove a hole from the substrate
333 # 1 hole per sketch
334 """
335   rootComp = adsk.core.Application.get().activeProduct.rootComponent
336   # get reference to the sketches and plane
337   sketches = rootComp.sketches
338   xyPlane = rootComp.xYConstructionPlane
339   sketch   = sketches.add(xyPlane)
340   # draw 1 hole
341   xCentre, xLength, yCentre, yLength, pixValue = hole
342   xMid, yMid, xLen, yLen = makeBox(xCentre, yCentre, pixSize, xLength, yLength)
343   # define sketch parameters
344   midPoint  = adsk.core.Point3D.create( xMid, yMid, 0)
345   edgePoint = adsk.core.Point3D.create( xLen, yLen, 0)
346   # create a new sketch and get lines reference
347   lines = sketch.sketchCurves.sketchLines
348   lines.addCenterPointRectangle(midPoint, edgePoint)
349   totalLines = len(lines)
350   l0 = totalLines - 4
351   l1 = totalLines - 3
352   l2 = totalLines - 2
353   l3 = totalLines - 1
```

```
354     # add curvature on defined corner
355     if pixValue >= 2**3 + 1:
356       # corner d = bottom left
357       arc = sketch.sketchCurves.sketchArcs.addFillet(lines[l1], lines[l1].endSketchPoint.
              geometry, lines[l2], lines[l2].startSketchPoint.geometry, roundOff)
358       pixValue -= 2**3
359
360     if pixValue >= 2**2 + 1:
361       # corner c = bottom right
362       arc = sketch.sketchCurves.sketchArcs.addFillet(lines[l2], lines[l2].endSketchPoint.
              geometry, lines[l3], lines[l3].startSketchPoint.geometry, roundOff)
363       pixValue -= 2**2
364
365     if pixValue >= 2**1 + 1:
366       # corner b = top right
367       arc = sketch.sketchCurves.sketchArcs.addFillet(lines[l3], lines[l3].endSketchPoint.
              geometry, lines[l0], lines[l0].startSketchPoint.geometry, roundOff)
368       pixValue -= 2**1
369
370     if pixValue >= 2**0 + 1:
371       # corner a = top left
372       arc = sketch.sketchCurves.sketchArcs.addFillet(lines[l0], lines[l0].endSketchPoint.
              geometry, lines[l1], lines[l1].startSketchPoint.geometry, roundOff)
373       pixValue -= 2**0
374
375     for profile in sketch.profiles:
376       profileCollection.add(profile)
377
378     sketchCollection.add(sketch)
379     return profileCollection, sketchCollection
380
381 def run(context):
382     ui = None
383     try:
384       app = adsk.core.Application.get()
385       ui  = app.userInterface
386
387       # NEEDED FEATURES
388       design      = app.activeProduct
389       rootComp = design.rootComponent
390       extFeats   = adsk.fusion.ExtrudeFeatures.cast(rootComp.features.extrudeFeatures)
391       # turn off history / tracking
392       adsk.fusion.Design.cast(app.activeProduct).designType = adsk.fusion.DesignTypes.
              DirectDesignType
393       # PROGRESS DIALOG for CREATION
394       progressSketches = ui.createProgressDialog()
395       progressSketches.isBackgroundTranslucent = False
```

```
396     progressSketches.isCancelButtonShown = False
397     progressSketches.hide()
398     # PROGRESS DIALOG for DELETION
399     progressDelete = ui.createProgressDialog()
400     progressDelete.isBackgroundTranslucent = False
401     progressDelete.isCancelButtonShown = False
402     progressDelete.hide()
403     # grab user inputs
404     p, gridSpace, roundOff, thick = setVariables(ui, design)
405     # create a new sketch on the xy plane
406     sketches = rootComp.sketches
407     xyPlane = rootComp.xYConstructionPlane
408     sketch   = sketches.add(xyPlane)
409     # Create list of holes
410     pattern    = mosaic(makeAperture(p), p) # make moasiaced pattern in pixels
411     rounded   = redefine_Points(pattern, p) # claculate rounded corners
412     holes        = makeList(rounded) # convert to a list, and glob multi-pixel holes
            together
413     numHoles = len(holes)
414     """
415     *** SUBSTRATE BACKING ***
416     """
417     substrateSketch = adsk.core.ObjectCollection.create()
418     # draw the outline square
419     lines = sketch.sketchCurves.sketchLines
420     # centre point, in pixels
421     xPoint = 0
422     yPoint = 0
423     # convert pixels to a distance centre, and dimensions
424     xMid, yMid, xLen, yLen = makeBox(xPoint, yPoint, gridSpace, 3 * p, 3 * p)
425     recLines = lines.addCenterPointRectangle(adsk.core.Point3D.create(xMid, yMid, 0), #
            Centre
426     adsk.core.Point3D.create( xLen, yLen, 0)) # half of dimensions
427     # save as sketch
428     substrateSketch.add(sketch.profiles.item(0))
429     # extrude
430     distance = adsk.core.ValueInput.createByReal(thick)
431     extrude = extFeats.addSimple(substrateSketch,
432       distance,
433       adsk.fusion.FeatureOperations.NewBodyFeatureOperation)
434     sketch.deleteMe()
435     # collections
436     profileCollection = adsk.core.ObjectCollection.create()
437     sketchCollection = adsk.core.ObjectCollection.create()
438     progressSketches.show('Aperture Creation', 'Holes Sketched: %p%', 0, numHoles)
439     for hole in range( len(holes) ):
440       profileCollection, sketchCollection = sketchHole(holes[hole], gridSpace, roundOff,
```

```
            profileCollection, sketchCollection)
441         progressSketches.progressValue = hole
442         # Create an extrusion input
443         extInput = extFeats.createInput(profileCollection, adsk.fusion.FeatureOperations.
                CutFeatureOperation)
444         # set the distance extend to be a single direction
445         extInput.setOneSideExtent(adsk.fusion.ThroughAllExtentDefinition.create(), adsk.
                fusion.ExtentDirections.PositiveExtentDirection)
446         # extrude
447         extFeats.add(extInput)
448         adsk.doEvents()
449         progressSketches.hide()
450
451         # delete sketches
452         progressDelete.show('Aperture Creation', 'Sketches Deleted: %p%', 0, len(
                sketchCollection) )
453         for i, sketched in enumerate(sketchCollection):
454           sketched.deleteMe()
455           progressDelete.progressValue = i
456           progressDelete.hide()
457       ui.messageBox('p{} Aperture Creation Complete'.format(p), 'Coded Aperture Notification',
              0, 2)
458     except:
459       if ui:
460         ui.messageBox('Failed:\n{}'.format(traceback.format_exc()))
461 # https://forums.autodesk.com/t5/fusion-360-api-and-scripts/api-create-a-sketch-on-a-
      surface-of-a-body/td-p/8064061
```

Code B.1: Fusion 360 CAD API, to construct a MURA of defined p value, thickness, and corner roundedness.

BIBLIOGRAPHY

[1] G. Grim *et al.*, "Neutron imaging at the NIF," *Journal de Physique IV (Proceedings)*, vol. 133, p. 913, 06 2006.

[2] J.N. Gruse *et al.*, "Application of compact laser-driven accelerator x-ray sources for industrial imaging," *Nuclear Instruments and Methods in Physics Research Section A: Accelerators, Spectrometers, Detectors and Associated Equipment*, vol. 983, p. 164369, 2020.

[3] A. Alavi and S.S. Huang, "Positron emission tomography in medicine: An overview," *Cancer Imaging*, vol. 31, no. 1, pp. 39–44, 2008.

[4] M.J. Cieślak, K.A.A. Gamage, and R. Glover, "Coded-aperture imaging systems: Past, present and future development - A review," *Radiation Measurements*, vol. 92, pp. 59–71, 2016.

[5] J. Cowley *et al.*, "Excitation and control of plasma wakefields by multiple laser pulses," *Physical Review Letters*, vol. 119, 07 2017.

[6] C. Emma *et al.*, "Terawatt attosecond x-ray source driven by a plasma accelerator," *APL Photonics*, vol. 6, no. 7, p. 076107, 2021.

[7] A.E. Hussein *et al.*, "Laser-wakefield accelerators for high-resolution x-ray imaging of complex microstructures," *Sci. Rep.*, vol. 9, no. 1, pp. 1–13, 2019.

[8] J.M. Krämer *et al.*, "Making spectral shape measurements in inverse Compton scattering a tool for advanced diagnostic applications," *Sci. Rep.*, vol. 8, no. 1, pp. 1–11, 2018.

[9] P. Goldreich and W.H. Julian, "Pulsar electrodynamics," *Astrophysical Journal*, vol. 157, p. 869, 1969.

[10] R.D. Blandford and R.L. Znajek, "Electromagnetic extraction of energy from Kerr black holes," *Monthly Notices of the Royal Astronomical Society*, vol. 179, no. 3, pp. 433–456, 1977.

[11] M.C. Begelman, R.D. Blandford, and M.J. Rees, "Theory of extragalactic radio sources," *Rev. Mod. Phys.*, vol. 56, pp. 255–351, 1984.

[12] J.F. Wardle *et al.*, "Electron-positron jets associated with the quasar 3C279," *Nature*, vol. 395, no. 6701, pp. 457–461, 1998.

[13] G. Sarri *et al.*, "Table-top laser-based source of femtosecond, collimated, ultrarelativistic positron beams," *Phys. Rev. Lett.*, vol. 110, no. 25, pp. 1–5, 2013.

[14] ——, "Generation of neutral and high-density electron-positron pair plasmas in the laboratory," *Nature Communications*, vol. 6, p. 6747, 2015.

[15] J.P. Gordon, "Radiation forces and momenta in dielectric media," *Phys. Rev. A*, vol. 8, pp. 14–21, Jul 1973.

[16] L. Torrisi, M. Cutroneo, and A. Torrisi, "Cold electrons acceleration in tnsa laser-generated plasma using a low-contrast fs laser," *Contributions to Plasma Physics*, vol. 61, no. 4, p. e202000097, 2021, e202000097 ctpp.202000097.

[17] U. Zastrau *et al.*, "Temperature and Kα -yield radial distributions in laser-produced solid-density plasmas imaged with ultrahigh-resolution x-ray spectroscopy," *Phys. Rev. E - Stat. Nonlinear, Soft Matter Phys.*, vol. 81, no. 2, pp. 1–4, 2010.

[18] J.D. Lindl *et al.*, "The physics basis for ignition using indirect-drive targets on the national ignition facility," *Physics of Plasmas*, vol. 11, no. 2, pp. 339–491, 2004.

[19] J.F. Seely *et al.*, "X-ray spectra in the 12- to 60-keV energy range from plasmas produced by the OMEGA laser," in *Applications of X Rays Generated from Lasers and Other Bright Sources II*, G.A. Kyrala and J.C.J. Gauthier, Eds., vol. 4504, International Society for Optics and Photonics. SPIE, 2001, pp. 198 – 204.

[20] ——, "X-ray emission from laser-generated plasmas recorded by a transmission crystal spectrometer," in *Laser-Generated and Other Laboratory X-Ray and EUV Sources, Optics, and Applications*, G.A. Kyrala *et al.*, Eds., vol. 5196, International Society for Optics and Photonics. SPIE, 2004, pp. 177 – 184.

[21] J.A. Koch *et al.*, "Multispectral x-ray imaging with a pinhole array and a flat bragg mirror," *Review of Scientific Instruments*, vol. 76, no. 7, p. 073708, 2005.

[22] K. Gi *et al.*, "Potential contribution of fusion power generation to low-carbon development under the paris agreement and associated uncertainties," *Energy Strategy Reviews*, vol. 27, p. 100432, 2020.

[23] E. Esarey, C.B. Schroeder, and W.P. Leemans, "Physics of laser-driven plasma-based electron accelerators," *Reviews of Modern Physics*, vol. 81, pp. 1229–1285, 2009.

[24] D.J. O'Brien, P. Kinsella, and P. McCavana, "Primary electron spot-size determination from slit-based measurements for linac photon beams," *Physica Medica*, vol. 32, no. 7, p. 958, 2016.

[25] B.A. Tozer, "Theory of the ionization of gases by laser beams," *Phys. Rev.*, vol. 137, pp. A1665–A1667, Mar 1965.

[26] D.A. Burton *et al.*, "Observations on the ponderomotive force," *Proceedings of SPIE*, 2017.

[27] R. Fitzpatrick, *Plasma Physics: an introduction*. CRC Press, 2014.

[28] S.V. Bulanov *et al.*, "Transverse-wake wave breaking," *Physical Review Letters*, vol. 78, no. 28, pp. 4205–4208, 1997.

[29] T. Tajima and J.M. Dawson, "Laser electron accelerator," *Physics Review Letters*, vol. 43, no. 4, pp. 267–270, 1979.

[30] A. Maksimchuk *et al.*, "Forward ion acceleration in thin films driven by a high-intensity laser," *Phys. Rev. Lett.*, vol. 84, pp. 4108–4111, May 2000.

[31] I. Blumenfeld *et al.*, "Energy doubling of 42 GeV electrons in a metre-scale plasma wakefield accelerator," *Nature*, vol. 445, no. 7129, pp. 741–744, 2007.

[32] X. Wang *et al.*, "Quasi-monoenergetic laser-plasma acceleration of electrons to 2 GeV," *Nat. Commun.*, vol. 4, no. May, 2013.

[33] E. Adli *et al.*, "Acceleration of electrons in the plasma wakefield of a proton bunch," *Nature*, vol. 561, no. 7723, pp. 363–367, 2018.

[34] O. Lundh *et al.*, "Few femtosecond, few kiloampere electron bunch produced by a laser-plasma accelerator," *Nat. Phys.*, vol. 7, no. 3, pp. 219–222, 2011.

[35] A.J. Gonsalves *et al.*, "Petawatt laser guiding and electron beam acceleration to 8 gev in a laser-heated capillary discharge waveguide," *Phys. Rev. Lett.*, vol. 122, p. 084801, 2019.

[36] A. Alejo *et al.*, "Laser-wakefield electron beams as drivers of high-quality positron beams and inverse-compton-scattered photon beams," *Frontiers in Physics*, vol. 7, 2019.

[37] M.H. Cho *et al.*, "Controlled electron injection facilitated by nanoparticles for laser wakefield acceleration," *Scientific Reports*, vol. 8, 2018.

[38] C.I.D. Underwood *et al.*, "Development of control mechanisms for a laser wakefield accelerator-driven bremsstrahlung x-ray source for advanced radiographic imaging," *Plasma Physics and Controlled Fusion*, vol. 62, no. 12, p. 124002, oct 2020.

[39] S.P. Mangles *et al.*, "Monoenergetic beams of relativistic electrons from intense laser-plasma interactions," *Nature*, vol. 431, no. 7008, pp. 535–538, 2004.

[40] C.G. Geddes *et al.*, "High-quality electron beams from a laser wakefield accelarator using plasma-channel guiding," *Nature*, vol. 431, no. 7008, pp. 538–541, 2004.

[41] J. Faure *et al.*, "A laser-plasma accelerator producing monoenergetic electron beams," *Nature*, vol. 431, no. 7008, pp. 541–544, 2004.

[42] A. Rousse *et al.*, "Production of a kev x-ray beam from synchrotron radiation in relativistic laser-plasma interaction," *Phys. Rev. Lett.*, vol. 93, p. 135005, 2004.

[43] S. Fourmaux *et al.*, "Single shot phase contrast imaging using laser-produced betatron x-ray beams," *Opt. Lett.*, vol. 36, no. 13, pp. 2426–2428, 2011.

[44] S. Kneip *et al.*, "X-ray phase contrast imaging of biological specimens with femtosecond pulses of betatron radiation from a compact laser plasma wakefield accelerator," *Applied Physics Letters*, vol. 99, no. 9, p. 093701, 2011.

[45] J. Wenz *et al.*, "Quantitative x-ray phase-contrast microtomography from a compact laser-driven betatron source," *Nature Communications*, vol. 6, no. 1, 2015.

[46] B.R. Wheaton, *Bremsstrahlung*. Berlin, Heidelberg: Springer Berlin Heidelberg, 2009, pp. 78–81.

[47] N. Lemos *et al.*, "Bremsstrahlung hard x-ray source driven by an electron beam from a self-modulated laser wakefield accelerator," *Plasma Phys. Control. Fusion*, vol. 60, no. 5, 2018.

[48] C.D. Armstrong *et al.*, "Bremsstrahlung emission from high power laser interactions with constrained targets for industrial radiography," *High Power Laser Sci. Eng.*, vol. 7, pp. 21–23, 2019.

[49] S. Chen *et al.*, "Mev-energy x rays from inverse compton scattering with laser-wakefield accelerated electrons," *Phys. Rev. Lett.*, vol. 110, p. 155003, 2013.

[50] N.D. Powers *et al.*, "Quasi-monoenergetic and tunable X-rays from a laser-driven Compton light source," *Nat. Photonics*, vol. 8, no. 1, pp. 28–31, 2014.

[51] A. Chaleil *et al.*, "Inverse compton scattering x-ray source yield optimization with a laser path folding system inserted in a pre-existent rf linac," *Nuclear Instruments and Methods in Physics Research A*, vol. 840, pp. 113–120, 2016.

[52] F. Albert *et al.*, "Laser wakefield accelerator based light sources: potential applications and requirements," *Plasma Physics and Controlled Fusion*, vol. 56, no. 8, p. 084015, 2014.

[53] F. Albert and A.G.R. Thomas, "Applications of laser wakefield accelerator-based light sources," *Plasma Physics and Controlled Fusion*, vol. 58, no. 10, p. 103001, 2016.

[54] H. Bethe, W. Heitler, and P.A.M. Dirac, "On the stopping of fast particles and on the creation of positive electrons," *Proceedings of the Royal Society of London. Series A, Containing Papers of a Mathematical and Physical Character*, vol. 146, no. 856, pp. 83–112, 1934.

[55] W. Heitler, *The Quantum Theory of Radiation*, 3rd ed. Oxford: Clarendon Press, 1954, ch. 26, pp. 256–268.

[56] G. Breit and J.A. Wheeler, "Collision of two light quanta," *Phys. Rev.*, vol. 46, pp. 1087–1091, 1934.

[57] V. Baier and V. Katkov, "Electroproduction of electron-positron pair in oriented crystal at high energy," *Physics Letters A*, vol. 373, no. 21, pp. 1874–1879, 2009.

[58] S.S. Bulanov *et al.*, "Electromagnetic cascade in high-energy electron, positron, and photon interactions with intense laser pulses," *Phys. Rev. A - At. Mol. Opt. Phys.*, vol. 87, no. 6, pp. 1–10, 2013.

[59] Y.C. Wang *et al.*, "Copious positron production by femto-second laser via absorption enhancement in a microstructured surface target," *Sci. Rep.*, vol. 10, no. 1, pp. 1–9, 2020.

[60] K.A. Tanaka *et al.*, "Current status and highlights of the eli-np research program," *Matter and Radiation at Extremes*, vol. 5, no. 2, p. 024402, 2020.

[61] N. Jourdain *et al.*, "The l4n laser beamline of the p3-installation: Towards high-repetition rate high-energy density physics at eli-beamlines," *Matter and Radiation at Extremes*, vol. 6, no. 1, p. 015401, 2021.

[62] J.W. Yoon *et al.*, "Realization of laser intensity over 10^{23} W/cm^2," *Optica*, vol. 8, no. 5, pp. 630–635, 2021.

[63] P. Chabert and N. Braithwaite, *Plasma synamics and equilibrium*. Cambridge University Press, 2011, ch. 2.

[64] P. Gibbon and E. Förster, "Short-pulse laser - plasma interactions," *Plasma Physics and Controlled Fusion*, vol. 38, no. 6, pp. 769–793, 1996.

[65] V.L. Ginsburg, *Propagation of electromagnetic waves in plasma*. Gordon & Breach, 1961.

[66] L. Landau, "On the vibrations of the electronic plasma," in *Collected Papers of L.D. Landau*, D. Ter Harr, Ed. Pergamon, 1965, pp. 445–460.

[67] F.F. Chen, *Introduction to plasma physics and controlled fusion*, 3rd ed. Springer, 2016.

[68] W. Kruer, *The Physics Of Laser Plasma Interactions*. Avalon Publishing, 1988.

[69] M. Raynaud *et al.*, "Strongly enhanced laser absorption and electron acceleration via resonant excitation of surface plasma waves," *Physics of Plasmas*, vol. 14, no. 9, p. 092702, 2007.

[70] S.C. Wilks *et al.*, "Absorption of ultra-intense laser pulses," *Phys. Rev. Lett.*, vol. 69, pp. 1383–1386, 1992.

[71] T.D. Arber *et al.*, "Contemporary particle-in-cell approach to laser-plasma modelling," *Plasma Phys. Control. Fusion*, vol. 57, no. 11, 2015.

[72] B. Hidding *et al.*, "Novel method for characterizing relativistic electron beams in a harsh laser-plasma environment," *Review of Scientific Instruments*, vol. 78, no. 8, p. 083301, 2007.

[73] D. Heunoske *et al.*, "Time-resolved emission spectroscopy of impact plasma," *Procedia Engineering*, vol. 58, pp. 624–633, 2013.

[74] A. Saemann *et al.*, "Isochoric heating of solid aluminum by ultrashort laser pulses focused on a tamped target," *Phys. Rev. Lett.*, vol. 82, pp. 4843–4846, 1999.

[75] G. Malka *et al.*, "Fast electron transport and induced heating in solid targets from rear-side interferometry imaging," *Phys. Rev. E*, vol. 77, p. 026408, 2008.

[76] R. Lee *et al.*, "Plasma-based studies with intense x-ray and particle beam sources," *Laser and Particle Beams*, vol. 20, no. 3, pp. 527–536, 2002.

[77] S.M. Wong, *Introductory Nuclear Physics*. John Wiley & Sons, Ltd, 1998.

[78] N.R. Sree Harsha, "The tightly bound nuclei in the liquid drop model," *European Journal of Physics*, vol. 39, no. 3, p. 035802, 2018.

[79] A. Harms, K. Schoepf, and D. Kingdon, *Principles of Fusion Energy: An Introduction to Fusion Energy for Students of Science and Engineering*, ser. Principles of Fusion Energy: An Introduction to Fusion Energy for Students of Science and Engineering. World Scientific, 2000.

[80] J.D. Lawson, "Some criteria for a power producing thermonuclear reactor," *Proceedings of the Physical Society. Section B*, vol. 70, no. 1, pp. 6–10, 1957.

[81] R.G. Mills, "Lawson criteria," *IEEE Transactions on Nuclear Science*, vol. 18, no. 4, pp. 205–207, 1971.

[82] J. Wesson and D.J. Campbell, *Tokamaks*, 3rd ed. Oxford: Clarendon Press; New York: Oxford University Press, 2004.

[83] M.D. Rosen, "The physics issues that determine inertial confinement fusion target gain and driver requirements: A tutorial," *Phys. Plasmas*, vol. 6, no. 5, pp. 1690–1699, 1999.

[84] M. Gatu Johnson *et al.*, "Neutron spectrometry - an essential tool for diagnosing implosions at the national ignition facility (invited)," *Review of Scientific Instruments*, vol. 83, no. 10, p. 10D308, 2012.

[85] M. Gordinier *et al.*, "Nuclear fusion power," in *Encyclopedia of Physical Science and Technology (Third Edition)*, 3rd ed., R.A. Meyers, Ed. New York: Academic Press, 2003, pp. 671–699.

[86] A.L. Kritcher *et al.*, "Achieving record hot spot energies with large hdc implosions on nif in hybrid-e," *Physics of Plasmas*, vol. 28, no. 7, 7 2021.

[87] P.K. Patel *et al.*, "Hotspot conditions achieved in inertial confinement fusion experiments on the national ignition facility," *Physics of Plasmas*, vol. 27, no. 5, p. 050901, 2020.

[88] W. Hogan *et al.*, "The national ignition facility," *Nuclear Fusion*, vol. 41, no. 5, pp. 567–573, 2001.

[89] D.G. Hicks *et al.*, "Streaked radiography measurements of convergent ablator performance," *Rev. Sci. Instrum.*, vol. 81, no. 10, 2010.

[90] R.E. Olson *et al.*, "Design calculations for NIF convergent ablator experiments," *EPJ Web Conf.*, vol. 59, pp. 3–6, 2013.

[91] B.A. Remington *et al.*, "Hydrodynamic instabilities and mix studies on NIF: Predictions, observations, and a path forward," *J. Phys. Conf. Ser.*, vol. 688, no. 1, 2016.

[92] H.D. Whitley *et al.*, "Comparison of ablators for the polar direct drive exploding pusher platform," *High Energy Density Physics*, vol. 38, p. 100928, 2021.

[93] G. Brunton *et al.*, "Shot Rate Improvement Strive for the National Ignition Facility (NIF)," *Proc. ICALEPCS2015, Melbourne, Aust.*, pp. 2–5, 2015.

[94] E.I. Moses, "Advances in inertial confinement fusion at the National Ignition Facility (NIF)," *Fusion Eng. Des.*, vol. 85, no. 7-9, pp. 983–986, 2010.

[95] E. Moses, "The national ignition facility: the world's largest laser," *20th IEEE/NPSS Symposium onFusion Engineering, 2003.*, pp. 413–418, 2003.

[96] ——, "The national ignition facility: status and plans for laser fusion and high-energy-density experimental studies," in *Proceedings of the 19th IEEE/IPSS Symposium on Fusion Engineering. 19th SOFE (Cat. No.02CH37231)*, 2002, pp. 487–492.

[97] J. Badziak, S. Jablonski, and J. Wołowski, "Progress and prospect of fast ignition of icf targets," *Plasma Physics and Controlled Fusion*, vol. 49, p. B651, 11 2007.

[98] Y.M. Wang, "A novel approach to icf ignition," in *2012 IEEE International Conference on Plasma Science*, 07 2012, pp. 4C–2.

[99] S. Atzeni *et al.*, "Studies on shock ignition targets for inertial fusion energy," in *CLEO: 2013*, 2013, pp. 1–2.

[100] V.N. Goncharov *et al.*, "Novel hot-spot ignition designs for inertial confinement fusion with liquid-deuterium-tritium spheres," *Phys. Rev. Lett.*, vol. 125, p. 065001, 2020.

[101] J. Nuckolls *et al.*, "Laser compression of matter to super-high densities: Thermonuclear (CTR) applications," *Nature*, vol. 239, no. 5368, pp. 139–142, 1972.

[102] F.E. Merrill *et al.*, "The neutron imaging diagnostic at NIF (invited)," *Rev. Sci. Instrum.*, vol. 83, no. 10, 2012.

[103] V.E. Fatherley *et al.*, "Aperture design for the third neutron and first gamma-ray imaging systems for the National Ignition Facility," *Rev. Sci. Instrum.*, vol. 89, no. 10, 2019.

[104] D. Fittinghoff, private communications with Lawrence Livermore National Laboratory, 2021.

[105] E. Hecht, *Optics*, 4th ed. Addison-Wesley, 1998.

[106] D. Attwood, *Soft x-rays and extreme ultraviolet radiation: principles and applications*. Cambridge university Press, 1999.

[107] Z. Wang and W. Guo, "Coded pinhole lens imaging," *OSA Continuum*, vol. 1, no. 1, pp. 64–77, Sep 2018.

[108] S. Cipiccia *et al.*, "A tuneable ultra-compact high-power, ultra-short pulsed, bright gamma-ray source based on bremsstrahlung radiation from laser-plasma accelerated electrons," *Journal of Applied Physics*, vol. 111, no. 6, p. 063302, 2012.

[109] V. Cantoni, S. Levialdi, and G. Musso, *Image Analysis and Processing*, 1st ed. Springer New York, NY, 1986.

[110] R.H. Dicke, "Scatter-hole cameras for x-rays and gamma rays," *Astrophysics Journal*, vol. 153, pp. L101–L106, 1968.

[111] T.M. Cannon and E.E. Fenimore, "Coded aperture imaging: many holes make light work," *Opt. Eng.*, vol. 19, no. 3, pp. 283–289, 1980.

[112] S.R. Gottesman and E.E. Fenimore, "New family of binary arrays for coded aperture imaging," *Applied Optics*, vol. 28, no. 20, pp. 4344–4352, 1989.

[113] R. Accorsi, F. Gasparini, and R.C. Lanza, "Optimal coded aperture patterns for improved SNR in nuclear medicine imaging," *Nucl. Instruments Methods Phys. Res. Sect. A Accel. Spectrometers, Detect. Assoc. Equip.*, vol. 474, no. 3, pp. 273–284, 2001.

[114] H. Arguello and G.R. Arce, "Rank minimization code aperture design for spectrally selective compressive imaging," *IEEE Trans. Image Process.*, vol. 22, no. 3, pp. 941–954, 2013.

[115] D. Hellfeld *et al.*, "A Spherical Active Coded Aperture for $4pi$ Gamma-Ray Imaging," *IEEE Trans. Nucl. Sci.*, vol. 64, no. 11, 2017.

[116] L. Mertz and N. Young, "Fenzel transform images," in *the International Conference on Optical Instruments and Techniques*. Chapman and Hall, London, 1961, pp. 305–310.

[117] E.E. Fenimore and T.M. Cannon, "Coded aperture imaging with uniformly redundant arrays," *Applied Optics*, vol. 17, no. 3, pp. 337–347, 1978.

[118] R.S. Strichartz, *A Guide To Distribution Theory And Fourier Transforms*, W. Scientific, Ed. World Scientific, 2003.

[119] E.E. Fenimore, "Coded aperture imaging: Predicted preformance of uniformly redundant arrays," *Applied Optics*, vol. 17, no. 22, pp. 3562–3570, 1978.

[120] Z. Mu and Y.H. Liu, "Aperture collimation correction and maximum-likelihood image reconstruction for near-field coded aperture imaging of single photon emission computerized tomography," *IEEE Trans. Med. Imaging*, vol. 25, no. 6, pp. 701–711, 2006.

[121] M. Grosse and O. Bimber, "Coded aperture projection," in *ACM SIGGRAPH 2008 Posters*, ser. SIGGRAPH '08. New York, NY, USA: Association for Computing Machinery, 2008.

[122] A. Busboom, H. Elders-Boll, and H.D. Schotten, "Uniformly redundant arrays," *Experimental Astronomy*, vol. 8, pp. 97–123, 1998.

[123] L.J. Meng and D.K. Wehe, "A gamma ray imager using clustered non-redundant array coded aperture," *Nuclear Science Symposium Conference Record*, vol. 2, pp. 763–766, 2003.

[124] P.T. Durrant *et al.*, "The application of pinhole and coded aperture imaging in the nuclear environment," *Nuclear Instruments and Methods in Physics Research A*, vol. 422, no. 1-3, pp. 667–671, 1999.

[125] D. Schellingerhout *et al.*, "Coded aperture nuclear scintigraphy: A novel small animal imaging technique," *Molecular Imaging*, vol. 4, no. 1, pp. 344–353, 2002.

[126] R. Pickholtz, D. Schilling, and L. Milstein, "Theory of spread-spectrum communications - a tutorial," *IEEE Transactions on Communications*, vol. 30, no. 5, pp. 855–884, 1982.

[127] T.J. Rouphael, *Chapter 3 - Common Digital Modulation Methods*, T.J. Rouphael, Ed. Burlington: Newnes, 2009.

[128] T. Nomura *et al.*, "A theory of two- dimensional linear recurring arrays," *Information Theory, IEEE Transactions on*, vol. 18, pp. 775 – 785, 12 1972.

[129] R.F. Wagner, D.G. Brown, and C.E. Metz, "On The Multiplex Advantage Of Coded Source/Aperture Photon Imaging," in *Digital Radiography*, W.R. Brody, Ed., vol. 0314. International Society for Optics and Photonics, 1981, pp. 72–76.

[130] M.A. Hussein, *Radiation Mechanics*, 1st ed. Elsevier Science, 2007.

[131] W. Huda and R. Slone, *Review of Radiologic Physics*, ser. High-Yield Systems Series. Lippincott Williams & Wilkins, 2003.

[132] W.S.C. Williams, *Nuclear and particle physics*. Oxford: Clarendon, 1991.

[133] A. Kagan and J.C. Oxley, *Counterterrorist Detection Techniques of Explosives*. Elsevier Science, 2022.

[134] E. Jones *et al.*, "SciPy: Open source scientific tools for Python," 2001.

[135] C.D. McGillem and G.R. Cooper, *Continuous and Discrete Signal and System Analysis*. Oxford University Press, 1991.

[136] S.W. Smith, *The Scientist and Engineer's Guide to Digital Signal Processing*. California Technical Publishing, 1997.

[137] G. Bradski, "The OpenCV library," *Dr. Dobb's Journal of Software Tools*, 2000.

[138] S. Agostinelli *et al.*, "GEANT4 - A simulation toolkit," *Nuclear Instruments Methods Physics Research Section A Accelerators Spectrometers, Detectors and Associated Equipment*, vol. 506, no. 3, pp. 250–303, 2003.

[139] F.G. Pikus, *Hands-On Design Patters with C++*. Packt Publishing, 2019.

[140] C.M. Brenner *et al.*, "Laser-driven x-ray and neutron source development for industrial applications of plasma accelerators," *Plasma Physics and Controlled Fusion*, vol. 58, no. 1, p. 014039, 2015.

[141] D.K. Bradley *et al.*, "Development and characterization of a pair of 30-40 ps x-ray framing cameras," *Review of Scientific Instruments*, vol. 66, no. 1, pp. 716–718, 1995.

[142] J.A. Oertel *et al.*, "Gated x-ray detector for the national ignition facility," *Review of Scientific Instruments*, vol. 77, no. 10, p. 10E308, 2006.

[143] A. Talebitaher *et al.*, "Imaging of plasma focus fusion by proton coded aperture technique," *Journal of Fusion Energy*, vol. 31, no. 3, pp. 234–241, 2012.

[144] S.V. Lebedev *et al.*, "Magnetic tower outflows from a radial wire array Z-pinch," *Monthly Notices of the Royal Astronomical Society*, vol. 361, no. 1, pp. 97–108, 2005.

[145] H. Chen *et al.*, "Relativistic quasimonoenergetic positron jets from intense laser-solid interactions," *Physics Review Letters*, vol. 105, p. 015003, 2010.

[146] L.A. Hof and J.A. Ziki, "Micro-hole drilling on glass substrates-A review," *Micromachines*, vol. 8, no. 2, p. 53, 2017.

[147] B. Yaakobi, F.J. Marshall, and D.K. Bradley, "Pinhole-array x-ray spectrometer for laser-fusion experiments," *Applied Optics*, vol. 37, no. 34, pp. 8074–8080, 1998.

[148] L. Labate *et al.*, "Novel x-ray multispectral imaging of ultraintense laser plasmas by a single-photon charge coupled device based pinhole camera," *Review of Scientific Instruments*, vol. 78, no. 10, p. 103506, 2007.

[149] J.A. Greenberg *et al.*, "Optimization of a coded aperture coherent scatter spectral imaging system for medical imaging," in *Medical Imaging 2015: Physics of Medical Imaging*, C. Hoeschen, D. Kontos, and T.G. Flohr, Eds., vol. 9412. International Society for Optics and Photonics, 2015, p. 94125E.

[150] D. Wang *et al.*, "Gamma-ray imaging with a time-modulated random coded aperture," *Review of Scientific Instruments*, vol. 90, no. 1, p. 015107, 2019.

[151] A.J. Kapadia *et al.*, "Monte-carlo simulations of a coded-aperture x-ray scatter imaging system for molecular imaging," in *Medical Imaging 2013: Physics of Medical Imaging*, vol. 8668. SPIE Medical Imaging, 2013.

[152] O. Ivanov *et al.*, "Portable x-ray and gamma-ray imager with coded mask: performance characteristics and methods of image reconstruction," *Nuclear Instruments Methods Physics Research Section A Accelerators Spectrometers, Detectors and Associated Equipment*, vol. 422, no. 1-3, pp. 729–734, 1999.

[153] A. Papoulis, *The Fourier integral and its applications*. New York: McGraw-Hill Electronic Science Series, 1962.

[154] M.P. Selwood, R. Heathcote, and C.D. Murphy, "Imaging Objects with Coded Apertures, Utilising a Laser Wakefield X-Ray source," in *16th Int. Conf. X-Ray Lasers*. Springer Proceedings in Physics Series., 2018.

[155] I.R. Cole, "Modelling cpv," Ph.D. dissertation, Loughborough University, 2015.

[156] D.E. Knuth, *Art of Computer Programming, Volume 2: Seminumerical Algorithms*. Boston, MA: Pearson Education, 2014.

[157] G. Marsaglia, "Xorshift RNGs," *J. Stat. Softw.*, vol. 8, no. 14, pp. 1–6, 2003.

[158] G. Marsaglia and W.W. Tsang, "Some Difficult-to-Pass Tests of Randomness," *J. Stat. Softw.*, vol. 7, no. 3, pp. 1–9, 2002.

[159] R. Simpson, *Introductory Electronics for Scientists and Engineers*. Allyn and Bacon, 1987.

[160] R. Heathcote *et al.*, "Coded aperture x-ray imaging of high power laser-plasma interactions on the Vulcan Laser System," in *Radiat. Detect. Med. Ind. Natl. Secur. XIX*, G.P. Grim *et al.*, Eds., vol. 10763. SPIE, 2018, p. 29.

[161] V. Mikerov *et al.*, "Prospects for efficient detectors for fast neutron imaging," *Applied Radiation and Isotopes*, vol. 61, no. 4, pp. 529 – 535, 2004, proceedings of the Fourth International Topical Meeting on Neutron Radiography. Advances in Neutron Imaging for the 21st Century.

[162] J.W. Scuffham *et al.*, "A CdTe detector for hyperspectral SPECT imaging," *Journal of Instrumentation*, vol. 7, no. 8, pp. P08 027–P08 027, 2012.

[163] S. Procz *et al.*, "X-ray and gamma imaging with medipix and timepix detectors in medical research," *Radiation Measurements*, vol. 127, p. 106104, 2019.

[164] D.R. Rusby *et al.*, "Pulsed x-ray imaging of high-density objects using a ten picosecond high-intensity laser driver," in *Emerging Imaging and Sensing Technologies*, vol. 9992, 2016.

[165] W.W. Moses, "Fundamental Limits of Spatial Resolution in PET." *Nuclear Instruments and Methods Physics Resesearch A.*, vol. 648 Supplement 1, pp. S236–S240, 2011.

[166] J.H. Hubbell and S.M. Seltzer, "NIST: X-Ray Mass Attenuation Coefficients," 1996, accessed: 2018.

[167] M.H. Weik, *Computer Science and Communications Dictionary*. Boston, MA: Springer US, 2001.

[168] C. Stoeckl *et al.*, "Operation of a single-photon‚Äìcounting x-ray charge-coupled device camera spectrometer in a petawatt environment," *Review of Scientific Instruments*, vol. 75, no. 10, pp. 3705–3707, 2004.

[169] A.T. Clark *et al.*, "Multimass velocity-map imaging with the pixel imaging mass spectrometry (pimms) sensor: An ultra-fast event-triggered camera for particle imaging," *The Journal of Physical Chemistry A*, vol. 116, no. 45, pp. 10 897–10 903, 2012.

[170] L. Labate *et al.*, "A novel technique for single-shot energy-resolved 2d x-ray imaging of plasmas relevant for the inertial confinement fusion," *Review of Scientific Instruments*, vol. 83, no. 10, p. 103504, 2012.

[171] L. Jowitt *et al.*, "HEXITEC 2 × 2 tiled hard x-ray spectroscopic imaging detector system," *Journal of Instrumentation*, vol. 17, no. 01, p. P01012, jan 2022.

[172] P.A. Ross, "A new method of spectroscopy for faint x-radiations," *J. Opt. Soc. Am.*, vol. 16, no. 6, pp. 433–437, Jun 1928.

[173] P. Kirkpatrick, "On the theory and use of ross filters," *Review of Scientific Instruments*, vol. 10, no. 6, pp. 186–191, 1939.

[174] S.K. Pandey *et al.*, "Doping and bond length contributions to Mn K-edge shift in La1 - xSrxMnO3 (x=0–0.7) and their correlation with electrical transport properties," *Pramana - J. Phys.*, vol. 70, 2008.

[175] J.A. Bearden and A.F. Burr, "Reevaluation of x-ray atomic energy levels," *Rev. Mod. Phys.*, vol. 39, pp. 125–142, Jan 1967.

[176] I.V. Khutoretsky, "Design of an optimal ross filter system for x-ray spectra measurements in the range of 8.98–88 kev," *Review of Scientific Instruments*, vol. 66, no. 1, pp. 773–775, 1995.

[177] M.H. Finger and T.A. Prince, "Useful classes of redundant arrays for imaging applications," *Imaging in High Energy Astronomy*, pp. 221–226, 1995.

[178] J. Ding, M. Noshad, and V. Tarokh, "Complementary lattice arrays for coded aperture imaging," *J. Opt. Soc. Am. A*, vol. 33, no. 5, pp. 863–881, 2016.

[179] J. Singer, "A theorem in finite projective geometry and some applications to number theory," *Trans. Amer. Math. Soc.*, vol. 43, pp. 377–385, 1938.

[180] D.M. Gordon, "On difference sets with small λ," *Journal of Algebraic Combinations*, vol. 55, pp. 109–115, 2020.

[181] V.I. Gelfcat, E.L. Kosarev, and E.R. Podolyak, "Programs for signal recovery from noisy data using the maximum likelihook principle," *Comput. Phys. Commun.*, pp. 335–348, 1993.

[182] G.P. Grim *et al.*, "Nuclear imaging of the fuel assembly in ignition experiments," *Phys. Plasmas*, vol. 20, no. 5, 2013.

[183] P. Volegov *et al.*, "Neutron source reconstruction from pinhole imaging at national ignition facility," *Rev. Sci. Instrum.*, vol. 85, no. 2, 2014.

[184] M.D. Wilke *et al.*, "The national ignition facility neutron imaging system," *Review of Scientific Instruments*, vol. 79, no. 10, p. 10E529, 2008.

[185] A. Nishino, H. Ujino, and M. Wadati, "Rodrigues formula for the nonsymmetric multivariable laguerre polynomial," *Journal of the Physical Society of Japan*, vol. 68, no. 3, pp. 797–802, 1999.

[186] S.M. Pollaine and D. Eimerl, "Modal analysis of power imbalance and pointing errors for direct drive and tetrahedral hohlraums," *Nucl. Fusion*, vol. 38, no. 10, pp. 1523–1530, 1998.

[187] S. Pollaine *et al.*, "NIF-scale hohlraum asymmetry studies using point-projection radiograph of thin shells studies by thin shell radiography," *42nd Annu. Meet. APS Div. Plamsa Phys.*, no. June 2014, 2000.

[188] N. Soppera, M. Bossant, and E. Dupont, "Janis 4: An improved version of the nea java-based nuclear data information system," *Nuclear Data Sheets*, vol. 120, pp. 294–296, 2014.

[189] CRC Handbook, *CRC Handbook of Chemistry and Physics*, 102nd ed. CRC Press, 2021.

[190] M. Staff. (2021) Metalary: Prices.

[191] G.W. Cooper and C.L. Ruiz, "NIF total neutron yield diagnostic," *Rev. Sci. Instrum.*, vol. 72, no. 1 II, pp. 814–817, 2001.

[192] A.L. Kritcher *et al.*, "Design of inertial fusion implosions reaching the burning plasma regime," *Nat. Phys.*, vol. 18, no. 3, pp. 251–258, 2022.

[193] C. Osolin, "'Hybrid' experiments drive nif toward ignition," Nov 2021.

[194] E.E. Fenimore and T.M. Cannon, "Uniformly redundant arrays: digital reconstruction methods," *Appl. Opt.*, vol. 20, no. 10, p. 1858, 1981.

[195] M.Z. Tarasko, "On the method for solution on the linear system with stochastic matrixes (in Russian)," *Preprint of the Physics and Energy Institute PEI-156, Obninsk*, 1969.

[196] P.P. Bruyant, "Analytic and iterative reconstruction algorithms in spect," *Journal of Nuclear Medicine*, vol. 43, no. 10, pp. 1343–1358, 2002.

[197] P.J. Green, "On use of the EM algorithm for penalized likelihood estimation," *Journal of the Royal Statistical Society: Series B (Methodological)*, vol. 52, no. 3, pp. 443–452, 1990.